Reliability of photovoltaic modules: from indoor testing to long-term performance prediction

THÈSE N^{O} 8672 (2018)

PRÉSENTÉE LE 31 MAI 2018

À LA FACULTÉ DES SCIENCES ET TECHNIQUES DE L'INGÉNIEUR
LABORATOIRE DE PHOTOVOLTAÏQUE ET COUCHES MINCES ÉLECTRONIQUES
PROGRAMME DOCTORAL EN ENERGIE

ÉCOLE POLYTECHNIQUE FÉDÉRALE DE LAUSANNE

POUR L'OBTENTION DU GRADE DE DOCTEUR ÈS SCIENCES

PAR

Eleonora ANNIGONI

acceptée sur proposition du jury:

Prof. J. A. Schiffmann, président du jury
Prof. C. Ballif, Dr A. F. A. Virtuani, directeurs de thèse
Dr T. Sample, rapporteur
Dr V. Naumann, rapporteur
Prof. H. Shea, rapporteur

ÉCOLE POLYTECHNIQUE
FÉDÉRALE DE LAUSANNE

Suisse
2018

Abstract

A fundamental challenge with solar energy is improving the reliability, and increasing the lifetime, of photovoltaic modules. Typically, photovoltaic module manufacturers guarantee 80% of the nominal power of their modules for 25 years, but this type of guarantee is not based on a deep comprehension of the degradation mechanisms of the modules. Moreover, the current target is to extend lifetimes to 30–40 years. For these reasons, accurate predictions of the lifetime of modules are needed. This doctoral work fits directly into this problematic, by developing test sequences and models that allow for the prediction of the electricity production of modules in the long term, taking into account the climates in which they operate. We consider the technology of crystalline silicon (c-Si), which largely dominates the market of photovoltaic modules.

In Chapter 1 we identify two main degradation mechanisms, potential-induced degradation (PID) and interconnection failures, which are of particular interest as they can occur not only in harsh environments such as desert or tropical regions, but also in temperate climates.

The main topic of this dissertation is the PID failure mechanism. Chapter 3 offers an introduction to PID for conventional p-type c-Si cells and modules. Chapter 3 also includes a description of the power regeneration mechanism.

In Chapter 4, we develop a predictive model for PID. This model is based on empirical equations between the variation of the module's power and the stress factors for PID (*e.g.* temperature or humidity), obtained from a matrix of accelerated tests in the laboratory. The result is a set of equations that describe the main phases of the evolution of PID as a function of the stress parameters.

In Chapter 5, we apply the model developed in Chapter 4 to predict the evolution of PID for mini-modules operating in real conditions (outdoors) in different climates. One difficulty is that, in this case, the stress levels vary continuously according to the meteorological conditions. We overcome this issue by using a mathematical method based on the concept of *equivalent time*. Moreover, suitable thresholds on the weather conditions are set to properly simulate the different phases of PID. In Chapter 6, we evaluate the effectiveness of some strategies that are currently available on the market to obtain "PID-free" modules.

Chapter 7 is devoted to interconnection failures, the second degradation mode under study in this dissertation. In particular, we validate experimentally a model developed in LT-SPICE that simulates the performance of a module with disconnections in the electrical circuit.

In summary, this thesis proposes a combination of a dedicated sequence of accelerated tests and a mathematical model that allow us to predict, for a given location, the effect of PID on the power output of a module. We are confident that, in general, this methodology can be applied to other degradation mechanisms, therefore leading to an improved prediction of reliability of photovoltaic modules in different climates.

Key words: Photovoltaics, Solar cell, Silicon, Module, Reliability, Accelerated lifetime test (ALT), Degradation, Failure mode, Modeling, Simulation, Prediction, Lifetime, Climate, Potential-induced degradation (PID), Encapsulant, Interconnections, Water ingress, Water vapor transmission rate (WVTR), Finite elements method (FEM), LCOE, Durability

Résumé

Alors que l'efficacité de conversion de certains modules commerciaux dépasse désormais les 22%, un des défis majeurs de l'industrie photovoltaïque consiste à améliorer la fiabilité des modules afin d'augmenter leur durée de vie. Généralement, les fabricants de modules garantissent 80% de la puissance nominale pendant 20 à 25 ans. Cependant, ce type de garantie n'a pas de réel fondement scientifique et n'est pas basé sur une compréhension détaillée des mécanismes de dégradation affectant les modules. L'objectif actuel étant de prolonger la durée de vie des modules au-delà de 30 - 40 ans, il est absolument nécessaire de pouvoir réaliser des prévisions détaillées du rendement énergétique d'un module sur le long terme. Ce travail de doctorat s'insère directement dans cette thématique en développant des séquences de tests et des modèles prédictifs permettant de quantifier la durée de vie des modules en fonction de leur environnement climatique. Les travaux présentés ici portent sur la technologie du silicium cristallin (c-Si) qui domine largement le marché des modules photovoltaïque.

En premier lieu, il s'est agi d'identifier les principaux mécanismes de dégradation. Deux ont été retenus comme critiques pour la technologie c-Si : le « PID » (potential-induced degradation) et les défaillances liées aux interconnections électriques. En effet, ces deux mécanismes de dégradation ne concernent pas seulement les modules implantés dans des régions avec climat extrême (par ex. désertique ou tropical) mais aussi dans les zones tempérées.

La majeure partie de cette thèse étant consacrée au PID, le Chapitre 3 offre tout d'abord une introduction au mécanisme de PID pour les cellules solaires en c-Si de type p. Ce chapitre contient également une description du processus de régénération de la puissance propre au PID.

Le Chapitre 4 est ensuite dédié au développement d'un modèle prédictif pour le PID. Ce modèle est basé sur des relations empiriques entre la variation en puissance du module et les paramètres influençant le PID (par ex. température ou humidité), obtenues à partir d'une matrice de tests accélérés réalisés en laboratoire. Le résultat est un ensemble d'équations qui décrivent les phases principales de l'évolution du PID en fonction des paramètres de stress.

Dans le Chapitre 5, le modèle ainsi développé est appliqué pour prédire l'évolution du PID dans des mini-modules fonctionnant en conditions réelles (extérieures) sous différents climats.

Mais, dans ce cas, les conditions de stress changent continuellement en fonction du temps, ce qui a nécessité des adaptations mathématiques. De plus, nous avons fixé des seuils spécifiques sur les conditions météorologiques afin de simuler de façon précise les différentes phases du PID. Dans le Chapitre 6, nous évaluons enfin l'efficacité de certaines stratégies qui sont actuellement disponibles sur le marché pour obtenir des modules «sans PID».

Finalement, le Chapitre 7 porte sur le deuxième mode de dégradation étudié dans le cadre de cette thèse, les défauts aux interconnections. En particulier, nous validons expérimentalement un modèle développé en LT-SPICE qui simule la performance d'un module présentant des interruptions dans le circuit électrique.

En résumé, cette thèse propose, en combinant une séquence de tests accélérés dédiée au PID et un modèle mathématique adapté, de prédire, pour un lieu donné, l'effet du PID sur la production électrique d'un module. Nous sommes convaincus que, de manière générale, cette méthodologie pourrait être appliquée à d'autres mécanismes de dégradation, permettant ainsi d'améliorer les prédictions de fiabilité des modules photovoltaïques dans différentes conditions climatiques.

Mots clefs : Photovoltaïque, Cellule solaire, Silicium, Module, Fiabilité, Test de durée de vie accélérée (ALT), Dégradation, Mode de défaillance, Modélisation, Simulation, Prédiction, Durée de vie, Climat, Potential induced degradation (PID), Encapsulant, Interconnexions, Entrées d'eau, Taux de transmission de la vapeur d'eau (WVTR), Méthode des éléments finis (FEM), LCOE, Durabilité

Contents

List of Figures

List of Tables

1 Reliability of photovoltaic modules

1.1 Introduction

1.1.1 Solar photovoltaic electricity

Within the challenge of covering worldwide increasing energy needs while maintaining limited CO_2 emissions, renewable energies are now becoming major actors on the scene. Not only do they offer energy, and more particularly electricity, with reduced environmental and health impacts, but they can also increase energy security, and improve energy access for developing countries. Energy sources such as solar and wind energy, biomass, and hydropower offer sustainable solutions to meet our energy needs as an alternative to fossil fuels. Photovoltaics (PV) – *i.e.* the direct conversion of sunlight into electricity – has, in particular, experienced rapid growth over the last few decades.

According to the International Energy Agency [53], the total capacity of PV installed worldwide by the end of 2016 was 303 GW, and the average annual growth rate in the period 2010–2016 was 40% (see Figure 1.1). PV adoption has also shown a rapid increase in Switzerland, with a total installed capacity of more than 1500 MW at the end of 2016, and is one of the pillars of the 2050 energy strategy of the Swiss Confederation. Reasons for this market expansion are the increasing competitiveness of photovoltaics, driven by the increase of solar cell efficiencies and by the steady reduction of PV module costs that have dropped by approximately 80% since 2010.

Photovoltaics is employed in power systems that range from residential installations (rooftop-mounted PV systems), with capacities of a few kilowatts, to large utility-scale systems (ground-mounted PV plants) with capacities of tens/hundreds of megawatts. The Tengger Desert Solar Park built in China in 2017, currently the largest solar power plant in the world, has a capacity of 1500 MW. The involvement of electric utilities *i.e.* electricity producers and retailers) is playing a role in the development of the PV market.

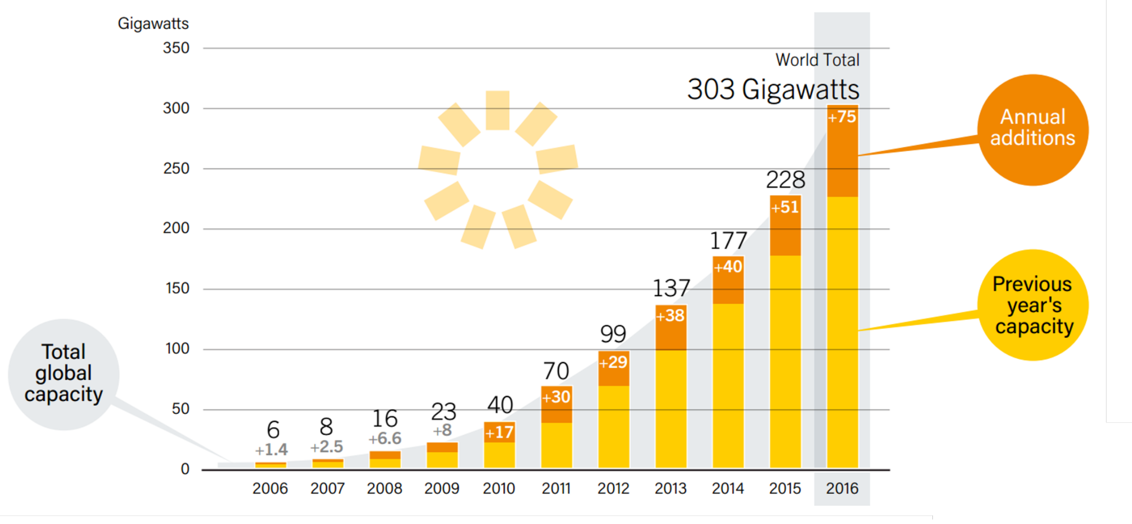

Figure 1.1: Photovoltaic global capacity and annual additions (reproduced from [138]).

1.1.2 Solar photovoltaic electricity: cost reduction

A factor to consider when evaluating whether to invest in a photovoltaic installation is its energy yield, *i.e.* the amount of electricity (in kWh) that the system will produce over its lifetime. The electricity generation cost is strictly related to the energy yield. Therefore, its estimation is particularly relevant for PV plant owners. The levelized cost of electricity (LCOE) is a quantity generally used to compare electricity generation costs among different technologies [150]. The LCOE is a present value assessment of the total system costs over its lifetime and the system returns. There are different formulas to calculate the LCOE, however they are all based on the same principle: the total lifecycle system cost (from building the plant to operation, maintenance, and decommissioning) is divided by the total energy yield of the system over its lifetime (Equation (1.1)):

$$\mathrm{LCOE} = \frac{\text{Lifecycle cost}}{\text{Lifetime energy yield}} \tag{1.1}$$

The LCOE is therefore expressed in €/Wh. Financial factors such as inflation or the cost of capital are also taken into account and discounted depending on the LCOE formula in use. To give an example, we refer to the formulas used in [150] and express the lifecycle cost and the lifetime energy yield in the following way:

$$\text{Lifecycle cost} = \mathrm{CAPEX} + \sum_{n=1}^{N} \frac{\text{OPEX-RV}}{(1+r)^n}, \tag{1.2}$$

$$\text{Lifetime energy yield} = \sum_{n=1}^{N} \frac{Y_0 \cdot (1-D)^n}{(1+r)^n}\,. \tag{1.3}$$

The formula for the LCOE becomes:

$$\text{LCOE} = \frac{\text{CAPEX} + \sum_{n=1}^{N} \frac{\text{OPEX-RV}}{(1+r)^n}}{\sum_{n=1}^{N} \frac{Y_0 \cdot (1-D)^n}{(1+r)^n}}\,, \tag{1.4}$$

where:

N is the number of years in operation [years]

CAPEX is the total initial investment [€/kWp]

OPEX is the sum of the annual operation and maintenance expenses [€/kWp]

RV is the residual value [€/kWp]

r is the discount rate [%]

Y_0 is the initial yield [kWh]

D is the system annual degradation rate [%]

The LCOE can be reduced by acting on different levels ([66] provides a detailed analysis of the impact of all the input parameters on the LCOE). At the module level, two key elements drive the cost. One is the efficiency with which the module converts sunlight into electricity: the higher the efficiency, the higher the initial (or nominal) energy yield, Y_0. The second element is the module's ability to maintain a high energy yield over many years. A low system annual degradation rate D and a low risk of module failure (implying low operation and maintenance expenses), as well as a long lifetime N, reduce the LCOE, making the PV system financially competitive. PV module degradation rate (affecting the system degradation rate D) is defined as the power decline over time. As we will see in Section 1.3.1, the degradation rate is strictly linked to the climate conditions in the PV plant site.

Considering the huge investments that companies and utilities are making on large solar plants all over the world, including locations with harsh climate conditions such as the MENA (Middle East and North Africa) region, the tropical zones of India or desert regions in South America, an accurate estimation of the LCOE of a PV plant should take into account the specific climate conditions of the installation site. This second aspect for the reduction of the LCOE is the motivation behind this work, which focuses on the lifetime and reliability of PV modules.

In the following sections we describe the composition of a PV module with special attention to the packaging scheme. We then introduce the concepts of lifetime and reliability for PV modules, give an overview of the degradation rates of PV installations worldwide, and give a brief overview of the main failure modes for PV modules. Finally, we describe accelerated aging tests, a tool employed to study module reliability in a reasonable time frame, and briefly discuss different uses of such tests as well as their limitations.

1.2 Photovoltaic module technology

The focus of this thesis is on PV modules with crystalline silicon (c-Si) cells, which represent the dominant technology with over 90% of the market share and of cumulative installations. The core device inside a c-Si PV module is the solar cell, a semiconductor material able to convert the energy of light into electricity by the photovoltaic effect. Solar cells are very thin, with typical thicknesses of around 200 µm, and brittle. Therefore, they are very fragile. In order to be deployed outdoors without breakage, damage or safety issues, they must be protected from environmental elements such as as rain, snow or wind. A PV module (or solar panel) is the assembly of several solar cells that are (i) electrically interconnected (typically in series, in order to increase the voltage output), and (ii) encapsulated between some materials that protect them from the environmental stress factors, and provide electrical isolation of the electrical circuit.

1.2.1 PV module electrical interconnections

Different levels of electrical connections are present in a PV module. For the terminology used in this thesis we refer to [51], Chapter 4.6, where clear definitions of the module parts are given which should be used with consistency in PV module reliability research.

Starting from the cell, “gridlines” (also called “fingers”) are metallic lines <0.4 mm thick that are directly in contact with the front silicon surface of the cell. Current collected in the gridlines makes its path towards the “busbars”, also directly in contact with the cell. The back surface of the cell is completely metalized and also features busbars, arranged in correspondence to the front ones. A typical cell has two or three busbars (even if the industry trend is to increase this number to four or five). This metalization on the cell is shown in Figure 1.2a.

Cells are then connected one to another by metallic ribbons, referred to as “cell interconnect ribbons”. Each ribbon is soldered on the cell busbar (which therefore becomes not visible), and connects the top of one cell with the rear of the next one. A line of serially interconnected cells is called a “string”. Multiple strings are then connected together with a “’string interconnect’ (see Figure 1.2b). In general, commercial PV modules are made of three substrings of 20 cells each.

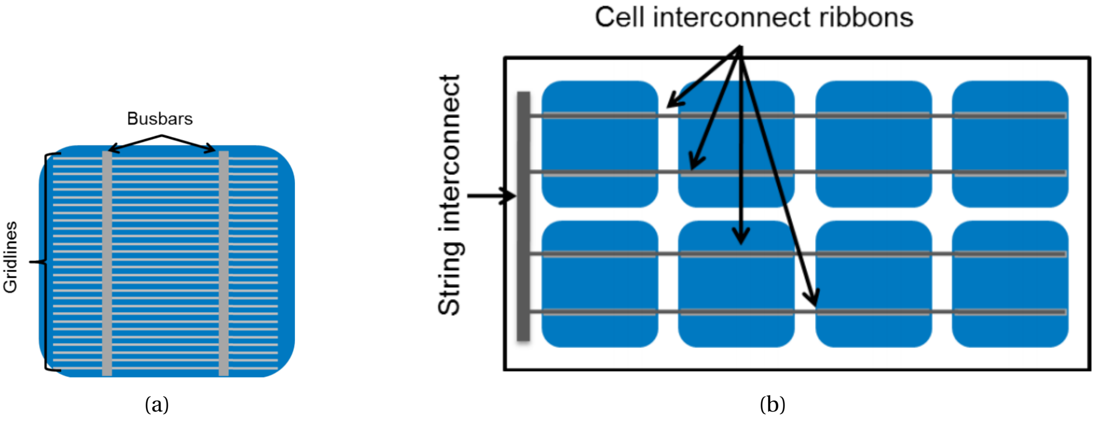

Figure 1.2: Schematic of the metalization in a c-Si PV module. (a) Metalization on the silicon cell: gridlines and busbars are in direct contact with the silicon. (b) Illustrative example of cells connected to one another with cell interconnect ribbons, forming a string; multiple strings are then connected together by means of a string interconnect. Images from [51].

1.2.2 PV module packaging

Figure 1.3 shows the typical packaging for c-Si cells. The stringed cells are generally protected on the front side by a glass. The rear cover can be either a polymer-based material (in this case it is called the backsheet) or glass. These configurations, typically referred to as "glass/backsheet" and "glass/glass", take 90% and 10%, respectively, of the c-Si module market [61]. Finally, the different layers are encapsulated together by means of a polymer foil on each side of the cells, called the encapsulant.

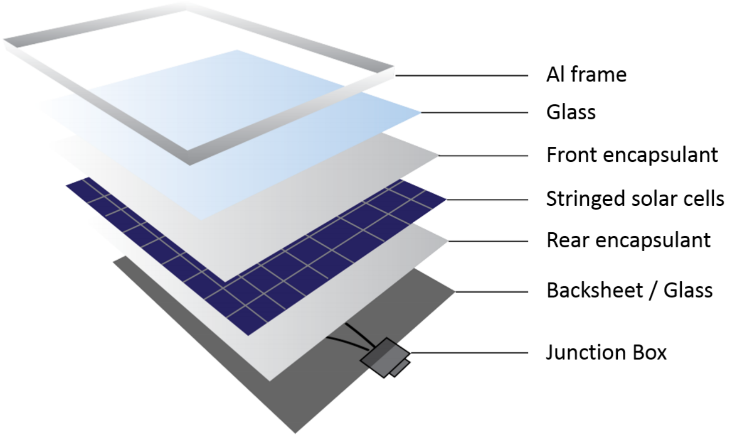

Figure 1.3: Packaging scheme of a c-Si PV module. The stringed cells are protected by glass in the front and a backsheet or glass in the rear. The different layers are encapsulated together by means of a polymer foil on each side of the cells. Image adapted from [95].

The purposes of PV module packaging are multiple [134], [21]. The front glass gives mechanical support against wind and snow loads, hail impact, and transport and installation damages. It must ensure at the same time good light transmittance to the cell surface. The encapsulant provides adhesion between the cells and the top and rear covers of the module. Properties required for a good encapsulant material are a high optical transmission, stability to high UV exposure and to elevated temperatures, good adhesion, and a coefficient of thermal expansion that limits the stresses due to thermal excursions. The encapsulant also has to maintain electrical insulation and to prevent moisture ingress. In some cases, the module is sealed around all its edges. The edge sealing provides a very high moisture barrier and makes the module packaging almost impermeable. The main functions of the rear cover are to provide electrical insulation (protecting people from dangerous high voltages and preventing current leaks from the circuit) and to prevent the ingress of moisture. The junction box is installed at the back side of the module, where the electrical connections exit the package. It is a plastic box that protects the connections from the environmental factors and hosts the bypass diodes, used to protect substrings from reverse biasing that may be caused by shading. A good sealing of the junction box to the backsheet is required to ensure good adhesion throughout the module lifetime. Finally, a metal frame is often added along the module perimeter. Glass/glass modules are often frameless. The role of the frame lies in its mechanical characteristics that bring benefits to the handling, storage, fixation, and grounding of the modules, and improves their resistance against mechanical loads such as wind or snow.

Good packaging is therefore essential to ensure a long lifetime of the PV module.

1.3 Reliability in photovoltaics

1.3.1 PV module degradation modes

As discussed in Section 1.1.2, increasing the lifetime of PV modules is a crucial factor for minimizing financial risks and is therefore of great importance for all stakeholders (investors, system owners, financial institutions, etc.). Modules operate outdoors for several years, exposed to a variety of environmental stresses. Weather factors such as temperature, humidity or wind loads can degrade the module materials reducing their power performance. PV module aging and degradation mechanisms have been documented over the past decades from field inspections worldwide. The main degradation modes are known and their causes have been identified in most cases. We recall that the focus of this thesis in on c-Si PV modules: in the following of this thesis we will always implicitly refer to this technology unless differently specified.

Typically, in reliability engineering, the failure rate of a system or component throughout its operation time is pictured with the so-called bathtub curve (Figure 1.4) (see [117] or [72] among others). The bathtub curve illustrates the idea that the operation of a device can be considered as composed of three periods:

1. An infant mortality period, with catastrophic failures occurring at the very initial stage of deployment, mainly due to defective items and causing the end-of-life of the product.
2. A midlife failure period, where failures are generally random and occur at a constant rate.
3. A wear-out period, where the failure rate increases again.

Generally, well-designed qualification testing should prevent or mitigate severe failures in the early life stage. Midlife and wear-out failures will strongly depend on the specific climatic conditions of the installation site.

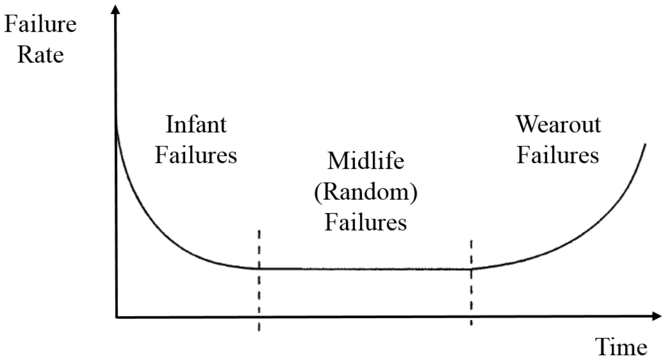

Figure 1.4: The bathtub curve.

In the case of a PV module, the main failure mechanisms at each of these three stages are shown in Figure 1.5, from a 2014 report of the International Energy Agency (IEA) dedicated to PV module failure modes in the field [51]. Their effect is typically quantified in terms of module “power degradation”, referring to the relative loss in the module maximum power P_{max}, *i.e.* the decrease of P_{max} with respect to the nominal power, normalized by the nominal power. For example, a degradation of 60% means that the module maximum power is the 40% of the nominal power.

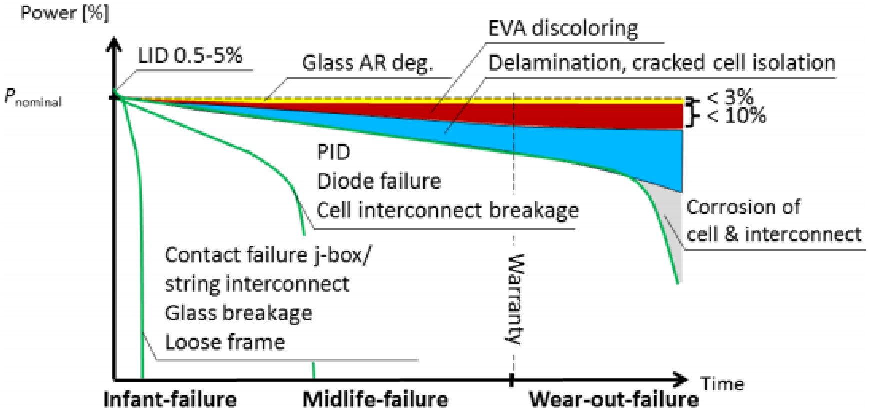

Figure 1.5: Three typical failure scenarios for c-Si modules. Source [51].

In this thesis, we examine two specific degradation modes: potential-induced degradation (PID) and power degradation due to defects in the module electric interconnections. Both of them fall into the category of midlife failures, even if PID can be considered as an infant failure. However, for the sake of completeness, we include here a short description of the other degradation mechanisms.

1. Infant failures occur at the beginning of the outdoor exposure of a PV module. Light-induced degradation (LID) is normally not considered to be a failure mechanism, as it occurs in the very first hours of operation and the module power then stabilizes. Infant failures are caused mainly by manufacturing defects of the module, transportation, or installation, or could be caused by poor design or selection of materials. Some of the most frequently observed infant failures are junction-box failures, glass breakage, defective cell interconnects, and loose frames. Note that PID can be considered as an infant failure as it was detected in some PV plants after less than three years of operation. We address this topic in greater detail in Chapter 3.

2. Failures relative to the midlife of PV modules were described in a study by DeGraaf [22]. PV modules in operation for eight years were inspected and showed defects mostly in the internal electrical circuit (detachment of ribbons and interconnects) and glass (*e.g.* delamination of the anti-reflecting coating).

3. Wear-out failures occur after many years of deployment, as a result of the steady degradation of materials due to continuous exposure to stresses. Typical examples are delamination and the corrosion of the metallic cell interconnections, both requiring long-term exposure to moisture ingress, and discoloring of the encapsulant. Wear-out failures determine the maximum lifetime of PV modules.

The module aging and the decrease in performance with time are complex processes that involve the interaction of several factors, namely:

i Service use weather conditions;

ii Module materials (cell technology, encapsulant material, etc.) and design;

iii Module mounting system; and

iv Module manufacturing process and quality control practices.

i The degradation processes that can affect PV modules are linked to climate conditions [88]. As recently confirmed by Jordan from NREL in an extensive literature survey on PV module field reliability [68], discoloration of the polymeric encapsulant is the most frequent degradation mode in hot climates. In tropical areas, a high relative humidity acts as preponderant stress factor and the most frequent degradation modes like delamination of the backsheet from the rear encapsulant are caused by water ingress. One degradation mode can be caused by a combination of various environmental stresses. For example, the delamination between the encapsulant and the front glass depends on the combination of UV irradiation, temperature, and relative humidity conditions [104]. As we discuss in Chapter 3, PID is triggered by a combination of high temperature and relative humidity. Furthermore, some degradation mechanisms are interdependent. Backsheet delamination, for instance, enhances moisture diffusion into the encapsulant which in turn increases the risk of corrosion of the metallic interconnects in the long term.

ii The materials employed in the module sandwich clearly play a prominent role in minimizing the risk of power degradation. For example, as we discuss in Chapter 6, encapsulants with a high volume electrical resistivity are very effective at limiting PID. The choice of materials should be based on the specific climate where the modules are to be installed, as two modules with the same bill of material (BOM) are not likely to suffer from the same failures in temperate locations, such as Continental Europe, or in desert climate countries, such as Saudi Arabia.

iii Module mounting systems (such as roof-mounted or building-integrated) that lead to a higher module temperature than the standard open-rack configuration will generally result in higher degradation rates.

iv Finally, quality control during the module manufacturing process is essential to ensure a good performance in the long run. For instance, a bad soldering of the metallic interconnections on the solar cells might induce damages in the cells' metallic fingers, which might then further degrade during exposure to thermal cycles.

In view of these considerations, it is evident that a proper estimation of the module aging requires a clear understanding of the degradation mechanisms as well as their impact on module power output.

Failure modes and effects analysis for PV modules

In the first phase of our work, we studied and analyzed in detail the most relevant papers in the literature, understanding the possible consequences of the various failure modes on the performance of PV modules. We also examined the likelihood of such failures to occur as a function of climate and module technology.

Among studies that report inspection of failures in old PV installations, SunPower's analysis [22] of more than 1.5 gigawatts (GW) of installations of various types of silicon modules from 21 manufacturers showed that the major failure mode observed is failed solder bonds (*e.g.* interconnect ribbons breakage, solder creep, etc.).

However, these analyses are mostly based on visual defects observed on modules; a quantification of their effect on power reduction is rarely available. In fact, not all failure modes have severe effects on the performance of PV modules. Moreover, the real impact of each failure mode on module performance depends on the climate where the module is installed. For instance, encapsulant yellowing in Switzerland does not significantly affect the power output [137], but it becomes a serious concern in hot and dry regions like Arizona where effect of UV radiation is harsher. There, it was estimated to be responsible, together with solder bond fatigue, for relative power drop as high as 42% [7].

Finally, failure modes are directly related to module materials and they, hence, continuously evolve with the material adjustments made by module manufacturers. For instance, the backsheet detachment observed on 95% of the modules in the 26-year-old PV plant at SUPSI [29] is not likely to happen in more recent installations, as that specific backsheet design by Arco Solar (Tedlar-aluminum-Tedlar) was particularly brittle.

Our analysis, which included participation in workshops, visits to research centers, and discussions with PV module reliability experts, led to the identification of two dominant failure modes to be considered for a prediction of long-term performance: PID and failures in electric interconnections. These degradation modes are of great interest in that they occur not only in extreme climatic conditions (*e.g.* tropical climates) but in temperate climates, such as in Switzerland, as well.

In the above-mentioned statistical survey of 2017 [68], Jordan *et al.* extensively analyzed the photovoltaic field reliability literature and deduced a ranking of the degradation modes based on both their frequency (number of affected modules) and their effect on power loss (severity). For the younger installations, those with less than 10 years of operation, the most observed degradation modes are hot spots and internal circuitry discoloration (both related to electric interconnections), encapsulant discoloration, broken cells, and PID (see Figure 1.6). Among these, encapsulant discoloration, though the most noticeable degradation mode, in fact has a low severity. Hot spots and PID are instead identified as the highest severity degradation modes for PV systems less than 10 years old.

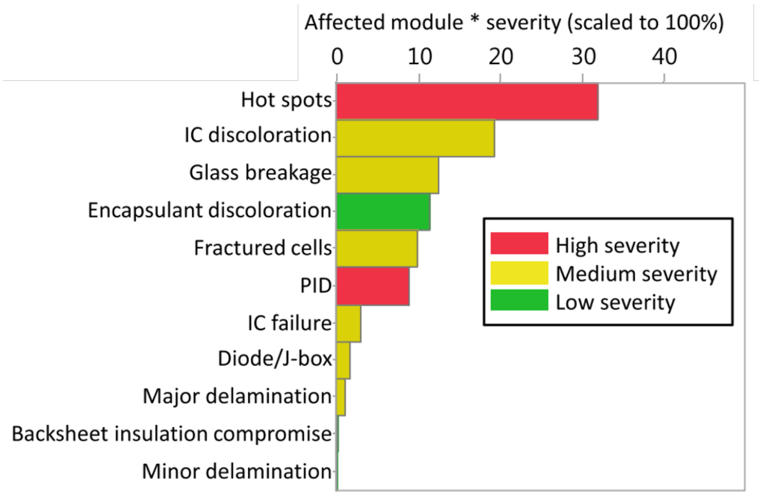

Figure 1.6: Pareto chart of the most significant degradation modes for systems installed in the last 10 years. PID is ranked as a high-severity degradation mode. Interconnection failures, which include hot spots and internal circuitry (IC) discoloration, also play a large role in degradation. Image adapted from [68].

These findings further justify our choice for the work carried out in this thesis, whose main goals are (i) to predict PID in different climatic conditions and identify module encapsulation architectures that prevent or limit the occurrence of PID, and (ii) to improve the understanding of the failures in the module electrical interconnections.

1.3.2 PV module reliability

The performance degradation described in the previous section must be quantified, and this is typically done in terms of loss of module maximum power with respect to its nominal power. The module maximum power, P_{max}, is the maximum power output of the module when measured at standard test conditions (STC), *i.e.* irradiance of 1000 W/m^2, solar spectrum AM1.5G, and temperature of 25°C. The nominal power, P_{nom}, indicates the initial maximum power of the module measured by the manufacturer (*i.e.* the nameplate value). More details on module performance characterization are provided in Chapter 2.

Presently, PV module manufacturers typically guarantee 80% of the nominal power for 25 years. If we assume a linear power degradation rate, this corresponds to an annual degradation rate D of 0.8%/year. Many manufacturers also give a double warranty of 90% of the initial maximum power for the first 10 years, and 80% of the initial maximum power for 25 years. Some top-tier companies started in the last few years to propose their own warranty curves. Some of the warranty curves that can be currently found in the PV market are presented in Figure 1.7.

There are reported cases of PV installations in which a high percentage of modules is still

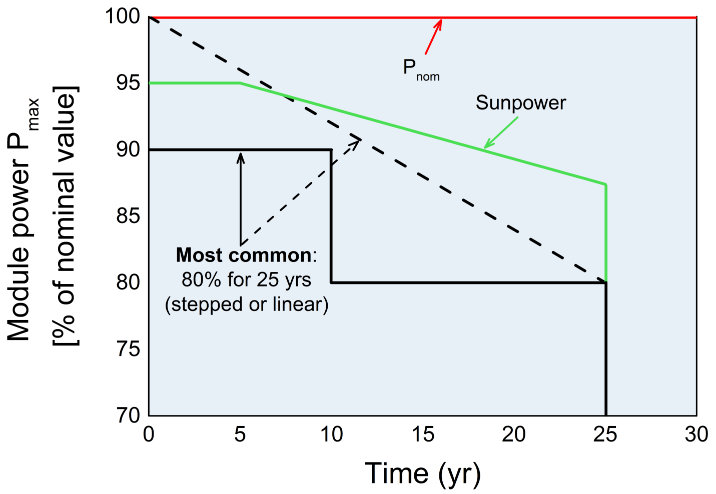

Figure 1.7: Typical power warranties for c-Si PV modules (black lines). The module maximum power P_{max} is expressed as percentage of the nominal power value, P_{nom}, *i.e.* the maximum power rated by the manufacturer (red line). The green line shows the warranty provided by Sunpower, which guarantees a higher energy yield during 25 years.

performing well after 20 or 30 years, with power performance exceeding the warranty criteria of 80% of the nameplate power [141], [29]. On the other hand, some PV plants have shown high power losses at the module level or safety concerns after only a few years of operation [71], [7]. On average, however, c-Si PV modules meet the traditional warranty specifications, as the mean degradation rate is in the 0.8–0.9%/year range and the median in the 0.5–0.6%/year range [68].

We remark that applying a linear degradation rate D for LCOE estimations (Equation (1.1)), though a reasonable preliminary approximation, may not be sufficiently accurate to give good predictions. In [66] Jordan *et al.* show how the power decline follows non-linear curves when caused by certain degradation modes, for example solder bond fatigue. Furthermore, we point out that, as already discussed in the previous section, the degradation rate is strongly dependent on the technology, module location, and year of installation (older PV modules tend to degrade more).

The period of 25 years guaranteed from the manufacturers is normally referred to as module “lifetime”. It would however be restrictive to define a PV module lifetime as the period in which the power output is at least 80% of the nominal power: if the energy production is still satisfactory to the user, then the module has not yet reached the end of its lifetime. In the remainder of this section we elaborate on the terms “lifetime”, “failure”, and “reliability” and on how they should be used for PV modules.

In reliability engineering, the lifetime (or useful life) of a product is defined as the “time interval from first use until user requirements are no longer met, due to economics of operation and maintenance, or obsolescence" (from the standard IEC 60050-191 [54]). Lifetime is typically linked to the occurrence of a failure, *i.e.* "the loss of ability to perform as required". Creating a consistent definition of failure for a PV module is challenging as its aging is generally characterized by a gradual degradation rather than a catastrophic event determining a complete interruption of its performance. The term "failure" is often used in publications in an unclear way, and modules are said to have "failed" without a definition of the term.

In this work, failure is defined as any effect that degrades the module power and that occurs under conditions that the module normally experiences.

Reliability is a research field in many industries. The term is defined in [54] as the "ability [of a system or component] to perform as required, without failure, for a given time interval, under given conditions". Failure is "the loss of ability to perform as required". Reliability is described by a probability function, $R(t)$, called the reliability function, that expresses the probability that a product performs properly (or "survives") by time t. Survival is the complementary event to failure. Reliability at time t is therefore given by $R(t) = 1 - F(t)$, where $F(t)$ is the cumulative failure distribution function (*i.e.* the probability that the product fails by time t).

A slightly different term often used is durability. The durability of an item is the "ability to perform as required, under given conditions of use and maintenance, until the end of useful life", where useful life (or lifetime) is the "time interval from first use until user requirements are no longer met, due to economics of operation and maintenance, or obsolescence". Durability is often measured as a time (*e.g.* years or cycles) and can be thought of as the expected value for the useful life. As noted in [161], whereas a reliability test is performed with the aim of reproducing failures in order to fix the issues and improve the device design, a durability test is performed to determine the length of the maximum failure-free period. A reliability test might turn out to be a durability test if the stress conditions are too weak to induce unscheduled failures. The tests performed to assess PV modules' resistance against degradation modes generally fall into the category of durability rather than reliability testing. Nevertheless throughout this work the term module reliability is often used in reference to module quality and long-term performance.

In the next section we briefly describe some of the accelerated aging testing procedures currently regulated by international qualification standards for PV modules, and discuss how the PV reliability community is working in order to improve such tests to obtain accurate lifetime predictions.

1.3.3 Accelerated aging testing

As do many other industries (*e.g.* electronics, space, automotive), photovoltaics addresses the topic of reliability by employing accelerated life tests (ALTs), whose aim is to reproduce in a short time the failure modes observed during a product's operational life. A test is said to be accelerated when the level of at least one stress factor that causes degradation is kept at a higher level with respect to the service situation.

Accelerated tests are performed in the PV industry with different purposes.

Qualification tests are used by manufacturers to certify modules before selling them on the market. For c-Si PV modules, the set of design qualification tests that modules should pass to enter the market is described by the current International Electrotechnical Commission (IEC) standard "IEC 61215: Terrestrial photovoltaic (pv) modules – design qualification and type approval" [56]. A module passes the qualification if, at the end of the tests, it satisfies some prescribed requirements on power output, visual appearance, and safety. Such tests to identify, as we saw in Section 1.3.1, the main degradation mechanisms and the stress factors that cause them are based on more than 35 years of field experience. Several studies describe how accelerated tests such as those in IEC 61215 affect a module's power output; see [155] and [39] among others. It has been demonstrated that they are able to reproduce some of the failure modes observed in the field (see Table 1.1 for a summary). For instance:

- Damp Heat test: modules are exposed to a temperature (T) of 85°C and a relative humidity (RH) of 85% for 1000 h. This test, included in IEC 61215, aims at determining the ability of the module to withstand the effects of long-term penetration of humidity. Failures such as corrosion of metallic components of the module and delamination can be reproduced. A module passes the test if its power $P_{\max}$ at the end of the 1000 hours is not less than the 95% of the initial $P_{\max}$.
- Thermal Cycling test: modules are subjected to 200 cycles with T from −40°C to 85°C (with injection of a current equal to the STC peak power current of the module). This test, included in IEC 61215, simulates the stress induced by thermal variations, and is particularly useful to duplicate failures in the electrical interconnections or cell cracks. Here again the threshold to pass the test is a power loss of less than 5%.
- PID test: this test is not included in the IEC 61215 standard but in a dedicated test specification that was developed recently and is currently in the status of a technical specification "IEC 62804-1:2015: Photovoltaic (pv) modules - test methods for the detection of potential-induced degradation - part 1: Crystalline silicon" [59]. The goal is to make it a qualification test that certifies the resistance of PV modules against PID when operated in outdoor conditions. One of the two accelerated test methods proposed to replicate PID is to subject the module to 60°C, 85% RH in a climatic chamber with a voltage of −1000 V applied between the cell's circuit and the grounded frame, for 96 h.

These qualification tests have been essential to identify materials that lead to early failures in the field and to achieve a high reliability for PV modules. However, they present some limitations if one wants to interpret them as reliability – predictive – tests. As specified in the IEC 61215 standard, qualification tests aim at showing "that the module is capable of withstanding prolonged exposure in general open-air climates. The actual lifetime expectancy

Table 1.1: Summary of the main accelerated tests for c-Si PV modules. Adapted from [158].

Accelerated Stress Test	**Failure mode**	**International regulation**
Thermal cycling	Broken interconnections Cell cracks Solder bond failures Module open-circuit - potential for arcing Junction box adhesion	IEC 61215, [56]
Damp heat	Corrosion Delamination Encapsulant loss of adhesion & elasticity Junction box adhesion Inadequate edge deletion	
Humidity freeze	Delamination Junction box adhesion Inadequate edge deletion	
UV exposure	Delamination Encapsulant loss of adhesion & elasticity Encapsulant & backsheet discoloration Ground fault due to backsheet degradation	
Static Mechanical Load	Structural failures Broken glass Broken interconnect ribbons Broken cells Solder bond failures	
Dynamic Mechanical Load	Broken glass Broken interconnect ribbons Broken cells Solder bond failures	
PID test	Potential-induced degradation	IEC 62804, [59]

of modules so qualified will depend on their design, their environment and the conditions under which they are operated.” (cit. from [56]). Their major limitations are thus:

1. They are not climate-specific. Two module types could pass the same test but later

experience very different degradation rates if installed in different climates.

2. It is not clear how to interpret the output of the tests in terms of module lifetime, because we do not know how the parameters of the tests (duration, stress levels) are related to the real stress conditions in the field (*i.e.* it is difficult to calculate an acceleration factor for such tests).

3. Two different module types might both pass a given qualification test but show very different performances if the stress conditions are increased, for example if the test is prolonged. An example is shown in Figure 1.8, from [46]. The power degradation of different module types is very similar after the 200 cycles prescribed by the IEC 61215, and the power loss is lower than 5% of the initial power so that all modules pass the test. However, if the test is extended beyond 200 cycles, a very different behavior is observed among the module types. From these results, one imagines that such modules might perform very differently when exposed in the field.

The general problems in industry of interpreting accelerated tests are addressed in detail in a paper by Meeker and Escobar [101].

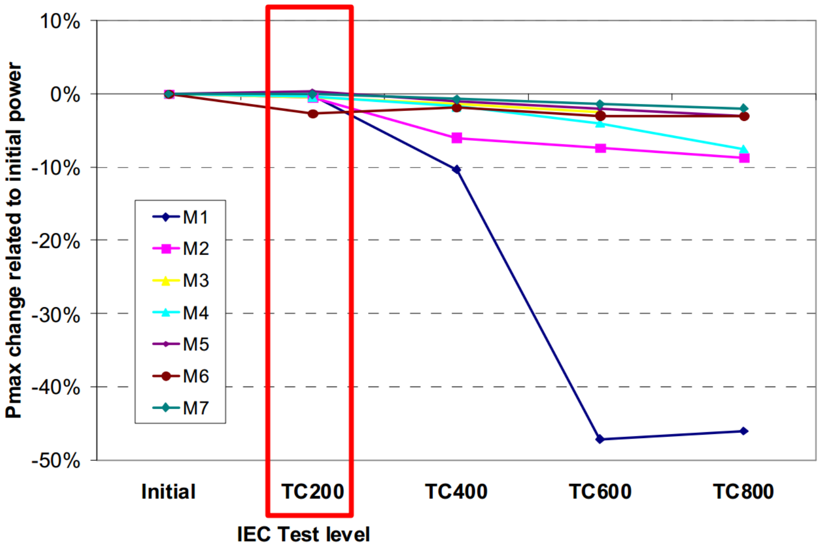

Figure 1.8: Change in maximum power P_{max} of different module types during an extended Thermal Cycling (TC) test. The x-axis represents the number of cycles. Image from [46].

Correlating indoor accelerated testing with outdoor exposure: towards lifetime testing of PV modules

In the last few years, the PV reliability community has begun to address the issue of correlation between indoor accelerated testing and outdoor prediction, as well as the need to differentiate the products. Even though the qualification tests prescribed in IEC 61215 are not suitable for lifetime predictions, they are still a good basis for lifetime tests. A lot of effort is aimed at developing new accelerated test programs (see Table 1.2 and [88]), based on IEC 61215, that will allow for increased confidence in long-term investments. For instance one target is to introduce comparative and lifetime tests in the assessment of module reliability.

- Comparative tests differentiate products according to their expected long-term durability in a specific use environment. They provide a relative quantification of the performance of different modules.
- Lifetime tests aim at predicting the performance in the long term in the desired location, providing an absolute quantification of a module's "lifetime".

Table 1.2: Three types of accelerated tests employed in the PV industry, adapted from [88].

	Qualification	**Comparative**	**Lifetime**
Purpose	Minimum design requirement	Comparison of products	Lifetime estimation
Quantification	Pass/fail	Relative	Absolute
Climate	Not differentiated	Differentiated	Differentiated

Great progress has been made in recent years towards the development of climate-specific and lifetime testing procedures. The International Photovoltaic Quality Assurance Task Force (PVQAT) gathers the efforts of many research groups worldwide in order to improve the understanding of the reliability of PV modules. One goal is to propose a test protocol climate specific. Three representative climates were identified based on the IEC standard for climate designation 60721-2-1: temperate (or moderate), tropical (warm damp, equable), and desert (extremely warm and dry). For example, Task Group 2 is focusing on failures of cell interconnects and solder bonds and seeks to define climate-specific conditions for the thermal cycling test.

The topic of reliability has been addressed in different industries for many decades, and some mathematical models for lifetime prediction of products are available. A review of accelerated test models is provided in [27]. Modeling in reliability engineering is typically based on statistical methods, where reliability functions are used and modeled with probability distributions such as the Weibull or Lognormal distributions; see for instance [116] and [72]. Failure modes dependent on others can be modeled with methods as multivariate survival analysis or competing-risks analysis [99]. Such techniques are applied in many industry sectors; for instance to study the reliability of MEMS (Micro-Electro Mechanical Systems), see *e.g.* [42] and [145].

Mathematical modeling is an emerging area of reliability in photovoltaics as well. Here reliability is addressed mostly by means of empirical lifetime models, such as the Peck model, that can be used for mechanisms that depend on humidity and temperature [124]. We briefly illustrate two examples where a correlation between accelerated testing and outdoor exposure, as well as a lifetime prediction, can be easily obtained because the kinetics of the degradation are completely known.

1. In [77], Kempe estimates the numbers of years that are equivalent to the Damp Heat test exposure for the particular degradation mode of PET hydrolysis (PET is commonly used as a backsheet material). For PET, the degradation kinetics $\mathscr{D}$ are known to follow a relation of this type:

   $$\mathscr{D} = A \cdot t \cdot RH^2 \cdot e^{-\frac{E_a}{\kappa T}}$$

   where A has units 1/time, T is the temperature, RH the relative humidity, t time, and E_a the activation energy of the chemical reaction. Kempe then shows how the Damp Heat test (at the standard Damp Heat conditions, 85°C, 85% RH for 1000h) extremely overstresses the module, as the hydrolysis induced is comparable to about 530 years of exposure of the module to the hot and humid climate of Miami.

2. Suppose that the power of a PV module, installed in a given location, is affected by a single degradation process. Suppose also that this process is caused by a chemical reaction that depends on temperature T only, and whose rate $\mathscr{R}$ follows the Arrhenius law:

   $$\mathscr{R} = A \cdot \exp\left(\frac{-E_a}{\kappa \cdot T}\right)$$

   where $\kappa = 8.6171 \times 10^{-5}$ is the Boltzmann constant [eV/K], A is a parameter independent of T and characteristic of the module materials, with units [1/time], and E_a is the activation energy of the chemical reaction. The degradation at time t is then $D(t) = \mathscr{R} \cdot t$ and the consequent module power $P(t) = 1 - D(t)$. Let us suppose a value for the activation energy of $E_a = 0.7$ eV, and take $A = 10^5$ h^{-1} (arbitrary values). If the time interval is divided into subintervals $(\Delta t)_i$, $i = 1, \ldots N$, each with a module temperature of T_i, one way (see *e.g.* [85]) to express the module power degradation at time j is

   $$P_j = 1 - \sum_{i=1}^{j} (\Delta t)_i \cdot A \cdot \exp\left(\frac{-E_a}{\kappa \cdot T_i}\right) . \tag{1.5}$$

   Supposing for example that the module is installed in Miami, and using as inputs the Typical Meteorological Year (TMY) data for this location (we will talk in detail about TMY in Chapter 5), where the time intervals have the length of 1 h, we can predict the evolution of the module power. We obtain, with the hypothetical values assumed for the Arrhenius parameters, that the module power after 25 years is 77% of the initial power (thus below the warranty limit of 80%).

In general, however, the study of PV module reliability cannot be addressed by simple relationships as in the two examples above. Factors that make the prediction of the power performance challenging include the fact that the kinetics of the degradation mechanisms are in general not so well known, the dependency of degradation on time-varying weather factors, and the interplay of multiple mechanisms.

This doctoral work fits directly into these open problems in PV module lifetime prediction. The goal of the research conducted here is to improve the understanding of module reliability, especially by providing a correlation between the indoor performance of modules during accelerated testing and their expected power output in different climates. The main focus is on the degradation mechanism of PID, for which peculiar challenges come from the fact that PID is caused by multiple stress factors (temperature, voltage, etc.) and from the non-monotonous behavior induced on the power evolution of the module. This follows, indeed, different phases (of degradation and regeneration, depending on the weather conditions), thus approaches that use cumulative damage or acceleration factors are inappropriate for lifetime prediction in the case of PID. Here, we propose a test sequence to be performed in laboratory, specifically developed here, that when applied in combination with a mathematical model and a simulation procedure allows for the prediction, for a given installation site, of the effect of PID on the electricity production of a PV module in the long term.

A second degradation mode, *i.e.* failures in the module electrical interconnections, is then analyzed. We contribute to the understanding of this failure mechanism by quantifying experimentally its effect on module electrical output. This data is then used to develop an electrical model that allows the simulation of the performance of a module with disconnections in the electric circuit.

1.4 Structure of this thesis

Following this chapter, introducing to the topic of reliability of solar modules, this thesis is organized as follows.

Chapter 2 provides a short review of the experimental techniques employed throughout this thesis. The setups for the characterization of module electrical performance and defects diagnostics, as well as some tools to measure material properties relevant to module reliability, are presented. The procedure for accelerated testing to reproduce potential-induced degradation (PID) in PV modules is then described.

In Chapter 3 we introduce the main subject of this dissertation, PID, to which we devote Chapters 3, 4, 5, and 6. For an easier reading of the chapters on PID, their structure and their interdependency is illustrated schematically in Figure 3.10. We start by offering in Chapter 3 a literature review on PID. The twofold effects that PID has on power performance (*i.e.* degradation and regeneration) are described and the most accepted physical model for such mechanisms is explained.

In Chapter 4, the experimental work aimed at developing a predictive model for PID is presented. First, by performing a matrix of laboratory-performed accelerated PID tests, on two-cell mini-modules, at different stress levels, we extract an empirical equation that describes the power loss due to PID as a function of temperature, relative humidity, applied voltage, and time. Secondly, with dedicated matrices of accelerated tests, we derive empirical equations to describe the nighttime power recovery (in the dark, with no voltage bias applied) and the daytime recovery (under illumination and with voltage bias).

In Chapter 5 we then apply the equations described above, obtained from indoor testing, to simulate the outdoor performance of the two-cell mini-modules with respect to PID assuming that they are installed in different climatic conditions.

In Chapter 6, our last chapter on the topic of PID, we conduct an analysis on the effectiveness of some strategies currently available on the market to limit or prevent PID at the module level. By manufacturing and testing materials with different properties in terms of both PID and water diffusion, we investigate how the module architecture could be reinforced to limit or delay the occurrence of PID. We use an accelerated PID test method in the IEC 62804-1:2015 (Test Method (a), described in Chapter 2.5) to differentiate the resistance against PID of various encapsulation schemes and materials. By extending the duration of the tests and by optimizing the stress conditions to the specific materials, we apply a qualification test as a comparative test.

Chapter 7 is devoted to disconnection failures. We assess experimentally for the first time the impact of one or more disconnected ribbons on the electrical performance of strings made of six serially connected cells. We then apply these experimental results to validate a model that we develop in LT- SPICE, which simulates the performance of a string with disconnected ribbons. A good agreement is found between the simulations and the measurements.

1.5 Contribution of this thesis to the research field

The work presented in this thesis led to the following contributions to the research field of PV module reliability and lifetime prediction:

1. We proposed a new sequence of accelerated tests that can be used as a lifetime testing protocol for PID.
2. An empirical model for PID as a function of the main stress factors was developed, starting from accelerated tests, which takes into account both the power degradation and regeneration mechanisms and contains new elements in respect to previous work. For the degradation mechanism, we introduce the dependency of power loss on voltage, which will allow for the prediction of PID in a PV plant at the string level.
3. For the regeneration mechanism, we demonstrated that, under irradiance, power regeneration can occur even with very high negative voltages applied. These effects were

previously observed in outdoor monitoring only in very few cases. Moreover, they were never included in general PID predictive models. Our study of the daytime regeneration led thus to a model that is more complete than previous work in that it covers all the different phases of PID during outdoors operation. Moreover these findings led to the conclusion that a complete matrix of lifetime tests for PID should include regeneration tests under illumination and with negative voltage bias (for reproducing the real operating conditions of modules during daytime).

4. When going from indoor testing results to outdoor performance prediction, the use of a mathematical method based on the concept of *equivalent time* allows us to "concatenate" the key equations at different time-steps in a consistent way alongside the time line, thereby obtaining a "piece-wise" model that approximates the continuous one. A similar approach was used in [15]. Here it is explained in detail, along with a mathematical proof of its validity, and employed to simulate a complex mechanism such as PID, constituted by different phases each described by a different equation. We believe that this approach could be employed to simulate the effect of other degradation mechanisms on PV module performance, thereby offering a possibility for improved lifetime predictions.

5. Special attention is given to the treatment of meteorological data. We propose some thresholds on, *e.g.* relative humidity or module temperature, to discriminate which phase of the PID mechanism is occurring in each time interval. In particular, our model employs a threshold that determines whether the module surface is wet, a condition mostly occurring during early morning and evening hours and that is responsible for harsh degradation. This threshold is identified from the literature on PID and is included for the first time in a PID predictive model.

6. By observing that the formation of dew on the surface is caused by the module temperature dropping below the dew point during the night, we remark that an accurate estimation of module temperature over the nighttime is required to properly simulate PID. King's model is not sufficient for this purpose, and we propose for example to combine it with a model by Myers and Kempe, this last one to be used for calculating module temperature at night.

7. At the module materials level, some strategies are now known to prevent PID, such as the use of "PID-free" cells. By performing accelerated tests on one-cell mini-modules manufactured with different combinations of materials, we evaluate the effectiveness of such strategies, identifying cost-effective solutions to obtain "PID-free" modules. An important finding is that the use of "PID-free" cells does not guarantee a "PID-free" module. Indeed, the encapsulant material also plays a crucial role. It turns out that devices consisting of a standard cell and laminated with a good encapsulant (*i.e.* with a high volume resistivity) are more PID-resistant than devices with a "PID-free" cell laminated with a low-resistive encapsulant. We also show how limiting water ingress into the module sandwich reduces the occurrence of PID.

8. We contribute to the understanding of failures in the electric interconnections by establishing a link between ribbon damage and module performance loss. By means of experimental measurements, we quantify the impact on the electrical performance of one or more broken ribbons for standard cells with three busbars. These measurements are then used to validate a model in LT-SPICE. The good agreement obtained is promising for the application of our model to new interconnection solutions such as four or five busbar cells or multiwires.

At the time of writing, two publications were submitted to *Progress in Photovoltaics* (see [152] and [3]). The technique used in Chapter 6 to simulate water diffusion into PV modules was also employed in the frame of an experimental work in collaboration with the University of Ljubljana. This work led to a peer-reviewed publication as a co-author [63]. The experimental validation of the water diffusion simulations was presented with a poster, which received a "Best Poster Award", at the 2015 NREL Photovoltaic Reliability Workshop. The outcomes of this research also led to presentations at various international conferences: a complete list of presentations and conference proceedings is given in the Curriculum Vitæ section.

2 Experimental methods

In this chapter we present the experimental tools used in this thesis. We describe the setups employed for the fabrication of mini-modules used for the experimental work, the characterization techniques and some additional measuring tools, and some accelerated-aging test methods.

2.1 Lamination process

The assembly of the different elements of a PV module is done through the encapsulation, or lamination, process. As discussed in Chapter 1, this step is crucial to ensure a high quality and reliability of the PV module. The samples used for the accelerated testing in this work are mainly mini-modules (*i.e.* small modules, with typically 1 or 2 cells) that we manufacture at PVLAB. The solar cells are commercially available c-Si cells. The first step is called stringing and consists in connecting the cells electrically. This is done by manually soldering cell interconnect ribbons on the cell busbars. These ribbons are made of a metallic material, typically copper-based and tin-coated. The next step consists in stacking the module components: the stringed cells are placed between a glass (in the front) and a backsheet or glass (in the rear). An intermediate layer of encapsulant is added on both sides that acts as adhesive. The module lay-up is then placed into the laminator to undergo the encapsulation process.

The encapsulation is done with a typical flat-bed vacuum-bag laminator. An illustration of this type of laminator is given in Figure 2.1. The laminator is composed of two chambers separated by a flexible silicon membrane. Below the lower chamber, a heating plate allows controlling the temperature of the lamination process. The lamination parameters (temperature-pressure-time profile) generally depend on the encapsulant material only. The module stack is introduced into the laminator. Vacuum is created into the chambers to remove the air between the materials, which could result in voids in the encapsulated module. The temperature is set to the prescribed lamination. For a standard EVA, temperatures between 145°C and 165°C are used. The module stack is initially lifted from the heating plate by some metal pins for around 300 s. This pre-heating step allows the glass to heat up gently minimizing the risk of warping or breakage. The pins are then retracted, so that the stack lays directly on the heating plate, and a pressure, of typically 1 bar, is applied into the upper chamber and consequently by the silicon diaphragm onto the lay-up.

At this point, the curing process starts and typically lasts from 300 to 900 s. Curing is the process of crosslinking of the polymer chains. Its purpose is to increase the mechanical and thermal stability of the encapsulant. Moreover, during the curing the encapsulant becomes transparent. Curing is a critical step in module fabrication for module reliability. To ensure a good performance in the long term, a gel content (the ratio between the crosslinked and the non-crosslinked mass of polymer) of at least 80% is generally required in the industry. Whenever needed, we adjust the temperature-pressure-time profile of the lamination process of our samples in order to obtain a sufficient gel content.

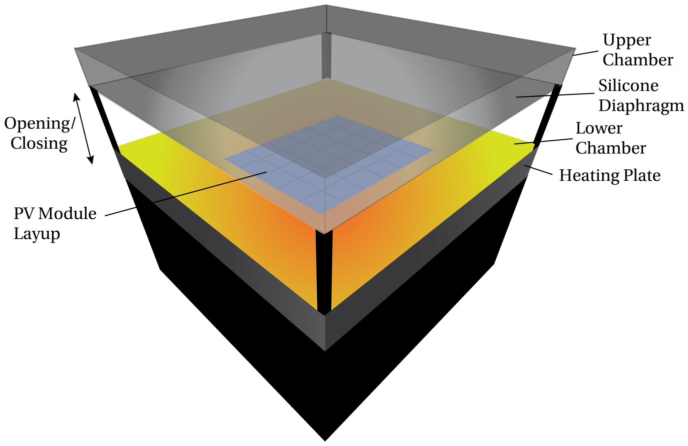

Figure 2.1: Schematic illustration of a flat-bed vacuum-bag laminator. Image reproduced from [95].

2.2 Characterization of the module performance

2.2.1 IV measurements

Current-voltage relationship for a solar cell

In a first approximation, a solar cell is a bipole (*i.e.* a two-terminal electronic component) that, under irradiance and with the two terminals connected, generates a current. The current intensity (from now on simply “current”) is proportional to the irradiance hitting the surface of the cell. We can picture the effect of the light-generated current I_L by means of an electric circuit with a generator and in short-circuit conditions.

Because of the presence of the p-n junction, current can flow in one direction only. In terms of electric circuit, this can be described as a diode: the cell does not allow current flow when the voltage across it is negative, and has very low (for an ideal diode, zero) resistance against current flow when the voltage is positive. In the dark, the current-voltage (IV) curve of a solar cell is indeed the typical IV-curve of a diode. In particular, the current in short-circuit conditions is zero. Under light, the current I of the cell is the sum of the diode current I_D and the light-generated current I_L (superposition principle of the IV-curve of the diode in the dark with the light-generated current):

$$I = I_L - I_D \,, \tag{2.1}$$

where I_D is given by the IV-curve of the diode:

$$I_D = I_0 \left(\exp \left[\frac{qV_D}{nkT} \right] - 1 \right) .$$

In Equation (2.1), q is the elementary charge (q =1.602×10^{-19} C), V_D is the voltage through the diode, k is the Boltzmann constant (k =1.3801×10^{-23} J/K), n is the ideality factor of the diode, I_0 is the diode saturation current, and T is the temperature of the cell in degrees Kelvin.

Compared to the curve of Equation (2.1), the measured IV-curve of a solar cell can show a lower derivative in a neighborhood of $V_D = 0$. This behavior reflects the presence of alternate paths that the light-generated carriers might follow within the cell, mainly because of recombination processes due to manufacturing defects. This point is represented in the electrical circuit by means of a resistance in parallel with the diode, called shunt resistance, R_{sh}. In order to have a good cell, the R_{sh} must be high: the higher the shunt resistance, the lower the current flowing through the shunt, I_{sh}, and therefore the higher the current I delivered by the cell. Applying Kirchhoff's current law we have $I = I_L - I_D - I_{sh}$. Substituting the expressions for the currents we get:

$$I = I_L - I_0 \left(\exp \left[\frac{qV_D}{nkT} \right] - 1 \right) - \frac{V_D}{R_{sh}} \tag{2.2}$$

However, this is still not an accurate electrical representation of a cell. Indeed, when a current is flowing through the cell, then for each value of current the corresponding measured value of voltage is lower than that predicted by the equation. This is due to the presence of some resistance in series with the previous components of the circuit. Such series resistance, R_s, is the result of a variety of contributions: (i) contact resistances (between the silicon and the metallic busbars, between the busbars and the interconnect ribbons), (ii) resistances of the top metal contacts, *i.e.* fingers, busbars and ribbons, and of the rear metal contacts, and (iii) the resistance of the lateral conduction in the emitter. The voltage that one actually measures between the cell's terminals is therefore $V := V_D - R_s I$, and consequently the equation that describes the equivalent circuit becomes:

$$I = I_L - I_0 \left(\exp \left[\frac{q(V + R_s I)}{nkT} \right] - 1 \right) - \frac{V + R_s I}{R_{sh}} \,. \tag{2.3}$$

Equation (2.3) is known as the *single-diode model* or *one-diode model* (see [149] among others). The final equivalent circuit of a solar cell described with this approach is illustrated in Figure 2.2.

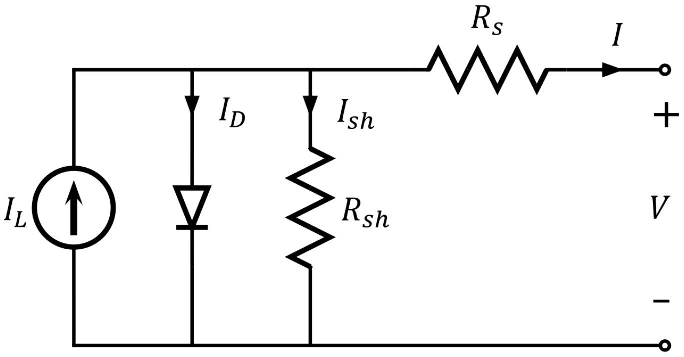

Figure 2.2: Equivalent circuit for a solar cell modeled with the single-diode model.

A more accurate representation of the solar cell is provided if a second diode is assumed, in parallel with the first one:

$$I = I_L - I_{01}\left(\exp\left[\frac{q(V+R_sI)}{n_1kT}\right]-1\right) - I_{02}\left(\exp\left[\frac{q(V+R_sI)}{n_2kT}\right]-1\right) - \frac{V+R_sI}{R_{sh}}\,. \tag{2.4}$$

In Equation (2.4), called *double-diode model* or *two-diode model*, I_{01}, I_{02}, n_1, and n_2 are, respectively, the diode saturation currents and the ideality factors of the first and second diode. We use Equation (2.4) in Chapter 7 to build a model that simulates the presence of disconnections in the module's electrical circuit.

Current-voltage relationship for a PV module

The single-diode model is used not only for a solar cell but also for a PV module or an array. A PV module is composed of several cells connected in series. Let us denote with N_s the number of cells in series, for example N_s =60 for most commercial c-Si modules. Then the module current is described by the following relationship, where n, R_s, and R_{sh} are the values of a single cell:

$$I_M = I_L - I_0\left(\exp\left[\frac{q(V_M+N_sR_sI_M)}{N_snkT}\right]-1\right) - \frac{V_M+N_sR_sI_M}{N_sR_{sh}}\,. \tag{2.5}$$

Measurement of IV curve characteristics

As with many other electrical devices, a fundamental electrical characterization method for PV modules is given by the IV measurement. The International Electrotechnical Commission

(IEC) norm 60904-3:2016 [55] defines the standard test conditions (STC) for PV module IV measurements: the module is at 25°C, illuminated by a simulated light (close to AM1.5G) of intensity 1000 W/m^2, with AM1.5G being the reference solar spectrum.

We perform IV curves measurements indoors with a solar simulator that was developed within a joint project between EPFL PV-LAB and PASAN. The device (PV module, mini-module or solar cell) is placed horizontally over a glass table, with the cells facing downwards. In the bottom part of the simulator, a system combining halogen and LED light sources illuminates the device with a spectrum replicating the AM1.5G. The temperature of the device is controlled with a temperature sensor (*e.g.* a PT100 or a thermocouple) placed in contact with the backsheet, in correspondence to a cell. The IV curve is corrected by the software to STC for temperature deviations using the measured temperature and the temperature coefficients for V_{oc}, I_{sc}, and P_{mpp}. No mismatch factor correction is applied to the measured curve to compensate for spectral deviations from AM1.5. The measurement uncertainty of the setup is estimated at ±3%, and the reproducibility at ±1% [106]. An example of IV curve is shown in Figure 2.3.

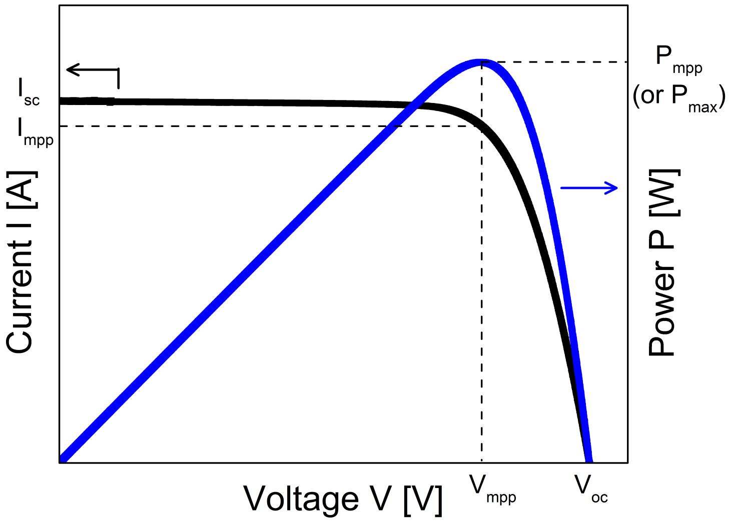

Figure 2.3: IV and power-voltage curve of a PV module, with relevant electrical characteristics.

From the IV measurements, the following parameters, indicative of the device performance, can be obtained. Some of them are reported in Figure 2.3.

- The short-circuit current, I_{sc}.
- The open-circuit voltage, V_{oc}.
- The current at the maximum power point, I_{mpp}.

- The voltage at the maximum power point, V_{mpp}.
- The maximum power, P_{mpp}.
- The efficiency, η, defined as $\eta := \frac{P_{\text{mpp}}}{P_{\text{in}}}$ where P_{in} is the power incident on the device.
- The fill-factor, FF, defined as $FF := \frac{I_{\text{mpp}} \cdot V_{\text{mpp}}}{I_{\text{sc}} \cdot V_{\text{oc}}}$.
- The series resistance, R_{s}, extracted from a linear fit of the IV curve in proximity of the V_{oc} point.
- The shunt resistance, R_{sh}, extracted from a linear fit of the IV curve in proximity of the I_{sc} point.

2.2.2 Electroluminescence

Electroluminescence (EL) is a common non-destructive technique for PV module characterization. It allows performing a qualitative analysis and a diagnosis of the cells defects, and is therefore very useful as a complementary tool to IV measurements to evaluate the degradation of a PV module. The module is supplied with a DC current (typically of the value of the I_{sc} current of the module) that induces a radiative recombination of electrons and holes in the solar cells. This results in emission of photons, which are detected by a high-resolution camera. The camera used is a NIKON with fixed focal length and a pixel resolution of 1660 × 1252. EL images are taken in dark conditions to reduce the background noise. A number of defects can be detected with EL imaging, for instance cell cracks, breakage of metallic interconnections, and cell shunts due *e.g.* to PID. An EL image is shown in Figure 2.4. For a more exhaustive list of failures detectable by EL the reader may refer to [51].

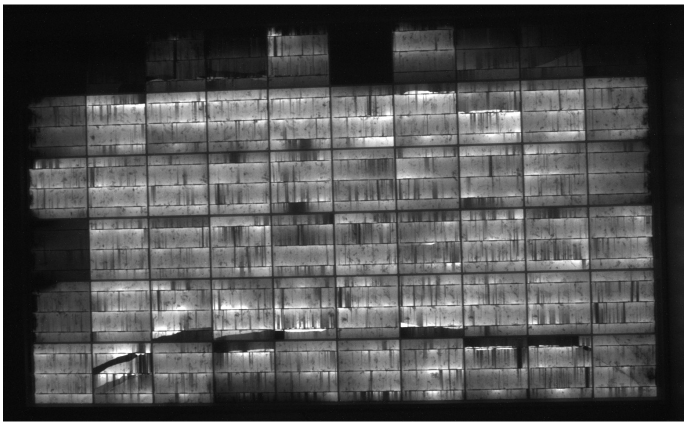

Figure 2.4: EL image of a commercial module after accelerated aging testing, revealing shunted regions (mainly in the cells close to the perimeter), cell cracks, and disconnected cell fingers.

2.3 Electrical resistivity measurements

The encapsulant materials are characterized in terms of electrical resistivity based on Method B in the standard that was recently developed specifically for PV materials, IEC "62788-1-2: Measurement procedures for materials used in photovoltaic modules – part 1-2: Encapsulants – measurement of volume resistivity of photovoltaic encapsulants and other polymeric materials" [58]. We use a Keithley 8009 resistivity test fixture and a Keithley 6517B electrometer. The samples are 55 mm × 55 mm squares of encapsulant (EVA) made of two layers laminated together with the standard lamination process for the given EVA. After measuring the sample thickness with a micrometer, the sample is preconditioned at the required conditions. Measurements of volume resistivity at high temperatures are carried out with the test fixture inside the climatic chamber where the samples are preconditioned. The sample is then placed between the two electrodes inside the test fixture. The electrometer is turned on and the voltage is cycled between $+1000$ V and -1000 V in 5 cycles of 1 min each. The current measurements are recorded at the end of each cycle, and a final averaged current value is calculated as described in [58].

2.4 Procedure for simulating water ingress into PV modules

Water vapor ingress into a material is a diffusion phenomenon. Diffusion is the process by which matter is transported from one part of a physical system to another as a result of random molecular motions. The mathematical theory for diffusion [20] was first developed by Fick (1855), who recognized an analogy with the process of heat conduction, also due to random molecular motions. He adopted the mathematical equation for heat conduction derived some years earlier by Fourier (1822): the rate of transfer of the diffusing substance through the unit area of a section is proportional to the concentration gradient measured normal to the section. The physical property which governs this relation is the diffusion coefficient D of the substance into the material (letters in bold denote vectors):

$$\mathbf{J}(\mathbf{x},t) = -D\nabla c(\mathbf{x},t) \tag{2.6}$$

With $\mathbf{J}$ we denote the rate of transfer per unit area of section (or flux) [g/(m$^2\cdot$ s)], c is the concentration of diffusing substance [g/m^3], and $\mathbf{x}$ is the space coordinate measured normal to the section. Here the diffusion coefficient D [m^2/s)] is assumed to be constant in all directions (*i.e.* isotropic material). Equation 2.6 is known as Fick's first law of diffusion.

The time evolution of the solute concentration inside the material is described by the solute conservation equation. In the case of water diffusing into a PV module (no source term, no velocity field) it is given by Equation 2.7.

$$\frac{\partial c(\mathbf{x},t)}{\partial t} + \nabla\mathbf{J}(\mathbf{x},t) = 0. \tag{2.7}$$

The flux **J** can be expressed according to Equation (2.6) in terms of a physically measurable quantity: the diffusion coefficient. Equation (2.7) takes the following form:

$$\frac{\partial c(\mathbf{x},t)}{\partial t} - \boldsymbol{\nabla}\left(D \cdot \boldsymbol{\nabla} c\left(\mathbf{x},t\right)\right) = 0. \tag{2.8}$$

Here we assume Fickian diffusivity, *i.e.* the diffusion coefficient does not depend on the concentration. With this hypothesis the solute conservation equation is linear, and can be written in a more compact form:

$$\frac{\partial c}{\partial t} = D\frac{\partial^2 c}{\partial \mathbf{x}^2}. \tag{2.9}$$

Equation 2.9 is known as Fick's second law of diffusion. It is a linear parabolic partial differential equation of the second order. Solutions of this equation give the time evolution of the concentration of diffusing substance into the material.

We first characterize the water diffusivity properties of the EVA and the backsheet needed as inputs in our simulations by means of water vapor transmission rate measurements as described in the next subsection.

2.4.1 Water vapor transmission rate measurements

A typical way to characterize the properties of a polymer (*e.g.* an encapsulant or a backsheet) with respect to water diffusivity is to measure its water vapor transmission rate (WVTR). The WVTR is defined as the flux of water through a material, *i.e.* the amount of water flowing per unit time through a unit area of the material surface. Units for WVTR are typically [g/m^2/day].

WVTR measurements are performed in two laboratories: (i) the Packaging Laboratory (LEC) of the University of Applied Sciences of Western Switzerland (HEIG-VD) based in Yverdon-les-Bains, Switzerland, and (ii) the Laboratory for Processing of Advanced Composites (LPAC) at EPFL. The measurements are carried out on a Mocon Permatran twin 3/33. The EVA sample, of thickness L, is set between two chambers. Some hydrogen with a controlled amount of water vapor inside is flowed into one chamber to keep a constant relative humidity of $RH = 90\%$. The other chamber is kept totally dry ($RH = 0\%$) by means of a constant flow of dry hydrogen. The water concentration inside the sample is initially null. As the test starts, the sample begins to absorb water from the wet chamber, while the water concentration on the dry side is kept null. The concentration gradient within the polymer film evolves (transient regime) and eventually reaches a linear profile. The WVTR is measured at every time interval from the beginning of the test until the stationary regime is reached. At this point the test is stopped.

The measured WVTR data can then be fitted with the equation for the WVTR curve:

$$\mathrm{WVTR}(t) = \frac{D \cdot c_{\mathrm{sat}}}{L}\left(1 + 2 \cdot \sum_{n=1}^{\infty} (-1)^n \exp\left(\frac{-D \cdot n^2 \cdot \pi^2 \cdot t}{L^2}\right)\right) , \tag{2.10}$$

where t is time and c_{sat} is the water saturation concentration of the polymer, expressed in [g/m^3]. Both D and c_{sat} depend on the measurement temperature. Equation 2.10 can be obtained by solving Fick's first law of diffusion (Equation (2.6)) with a Fourier series, imposing the boundary and the initial conditions as given by the WVTR measurement setup.

The steady-state value of the WVTR is calculated by taking the limit of Equation 2.10 for $t \to \infty$:

$$\mathrm{WVTR(steady\text{-}state)} = \lim_{t \to \infty} \mathrm{WVTR}(t) = \frac{D \cdot c_{\mathrm{sat}}}{L} . \tag{2.11}$$

An example of a typical WVTR curve with the fitting line is displayed in Figure 2.5.

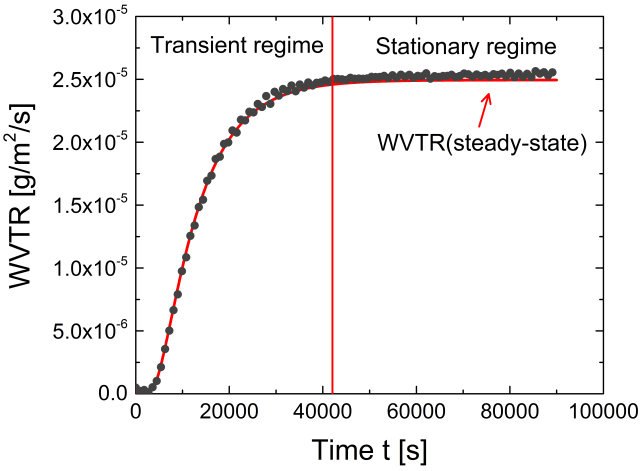

Figure 2.5: Typical WVTR curve of a backsheet as measured (black dots) and its fitting curve (red line) obtained with Equation (2.10). After an initial increase (transient regime), the WVTR values eventually reach a steady-state value.

2.4.2 Extracting the diffusivity properties needed as inputs for the simulations

With the purpose of simulating water diffusion at any environmental temperature, we measure for each material the WVTR at three different temperatures. The diffusivity properties of the materials (encapsulant and backsheet) and their dependency on temperature can thus be extracted. The procedure we use, described in this subsection, was previously set up by two of my colleagues, Valentin Chapuis and Federico Galliano. A similar procedure is used in some work where the topic of water diffusion into PV modules is addressed by means of simulations, *e.g.* [73], [79], and [85].

For each of the three measurement temperatures, we calculated the diffusion coefficient, the permeability, the solubility and the saturation concentration.

- By fitting the measured curve of the WVTR with Equation (2.10), the diffusion coefficient D and the factor $D \cdot c_{\text{sat}}$ are extracted. The latter is the value of the plateau of the curve, WVTR(steady-state).

- We use the following definition of permeability P:

  $$P := D \cdot S \, , \left[\frac{g}{m \cdot s \cdot mbar} \right] \tag{2.12}$$

  where S is the solubility of the material. By expressing the concentration of water at the surface of the polymer film in Equation (2.10) with Henry's law and denoting by $p_{\text{H}_2\text{O}}$ the water vapor partial pressure:

  $$c_{\text{sat}} = S \cdot p_{\text{H}_2\text{O}} \, , \left[\frac{g}{m^3} \right] \tag{2.13}$$

  we get

  $$\text{WVTR(steady-state)} = P \cdot \frac{p_{\text{H}_2\text{O}}}{L} \, . \tag{2.14}$$

  The water pressure inside the wet chamber of the WVTR setup is computed using the definition of relative humidity

  $$RH := \frac{p_{\text{H}_2\text{O}}}{p_{\text{H}_2\text{O}}^{sat}} \tag{2.15}$$

  where the water saturation pressure $p_{\text{H}_2\text{O}}^{\text{sat}}$ (expressed in [mbar]) is calculated as a function of the temperature T with the Arden Buck equation:

  $$p_{\text{H}_2\text{O}}^{\text{sat}}(T) = 6.1121 \cdot \exp\left(\left(18.678 - \frac{T}{234.5} \right) \cdot \frac{T}{T + 257.14} \right) \, . \tag{2.16}$$

  The permeability can now be calculated:

  $$P = \frac{\text{WVTR(steady-state)} \cdot L}{RH \cdot p_{\text{H}_2\text{O}}^{\text{sat}}}$$

- The solubility S is computed from the permeability definition (Equation (2.12)).

- The saturation concentration c_{sat} is obtained from the fitted value of $D \cdot c_{\text{sat}}$.

2.4.3 Finite elements method simulations

The diffusivity properties obtained and their dependency on temperature (Arrhenius relationship) are then used as inputs in our simulations of water diffusion into the module packaging. The moisture ingress is modeled as a diffusion problem using the *Transport of Diluted Species* interface in Comsol Multiphysics (version 4.4). For the purpose of this work, finite elements method (FEM) simulations are employed to model the water ingress into a glass/backsheet one-cell mini-module exposed to specific accelerated-aging conditions (*i.e.* temperature and relative humidity). The two-dimensional geometry employed in Comsol represents a vertical cross-section of the mini-module (see Figure 2.6).

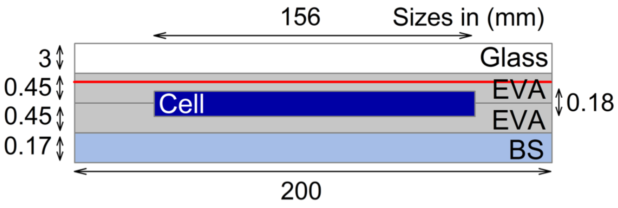

Figure 2.6: Schematic representation of a 2D geometry used in Comsol Multiphysics for simulating the diffusion of water into a one-cell mini-module. Water penetrates from the exposed surfaces of the EVA and BS. The maximum amount of water able to penetrate depends on the solubility S of the material. The diffusion through the materials is fast or slow depending on the value of the diffusion coefficient D of the material. An interface condition is added in Comsol that takes into account the different solubilities of the BS and EVA.

We impose the following conditions for the FEM simulations:

- Initial conditions
  We assume that the EVA and the backsheet are initially dry.

- Boundary conditions
  We suppose that the external surfaces of the EVA and of the backsheet are in equilibrium with the environment. Therefore the concentrations in the boundaries are calculated using Henry's law (Equation (2.13)).

- It is important to notice that the backsheet (BS) and the EVA have different water solubilities. The model developed in this thesis takes this into account, by specifying a condition at the interface between the two materials. As proposed in [133], we impose a continuity of the mass flux across the interface while a discontinuity in the concentration is set.

  - Continuity of the mass flux:

$$D_{\mathrm{BS}}\frac{\partial c_{\mathrm{BS}}(x,t)}{\partial x} = D_{\mathrm{EVA}}\frac{\partial c_{\mathrm{EVA}}(x,t)}{\partial x} \,,$$

for x belonging to the interface backsheet/EVA, where the equation for the flux comes from Fick's First Law of diffusion.

- Discontinuity of the concentration:

$$c_{\mathrm{BS}}(x,t) = K_{eq} \cdot c_{\mathrm{EVA}}(x,t) \ ,$$

for x belonging to the interface backsheet/EVA. K_{eq} is the partition coefficient, which is defined as the ratio of the solubilities $K_{eq} := \frac{S_{BS}}{S_{EVA}}$.

The simulation is run with a time step of 3600 s over the time interval of interest. The output of the simulation is the time evolution of the water concentration inside the mini-module encapsulation materials.

We should point out that this procedure was applied to samples made of glass, encapsulant, and backsheet (no cell), exposed outdoors in Neuchâtel (Switzerland) using real meteorological data as inputs. In the same samples, some commercial humidity sensors (SHT25 from Sensirion) were encapsulated, soldered on a strip made of a printed circuit board communicating with an electronic interface. This *in-situ* monitoring technique for RH in PV modules was developed by Marko Jankovec (University of Ljubljana), and more details can be found in [63]. A good agreement between the simulated results and the outdoor monitoring was achieved. These results were presented at the 2015 NREL Photovoltaic Reliability Workshop (see Curriculum VitæSection) but are not included in this dissertation.

2.5 Accelerated aging test for detecting PID in c-Si modules

The measure of a module sensitivity to PID is addressed in the IEC Technical Specification "62804-1:2015: Photovoltaic (PV) modules - test methods for the detection of potential-induced degradation - part 1: Crystalline silicon" [59], where two test methods are proposed.

Method (a) prescribes to test in a climatic (or environmental) chamber at 60°C and 85% RH for 96 h. As prescribed by the technical specification, temperature and humidity are applied as depicted in Figure 2.7. First, the chamber temperature is ramped from ambient to the specified stress temperature. Then, when the chamber and the module temperature reach the specified value, the relative humidity is progressively increased to the set value. When both the temperature and the relative humidity are at the set points, the module is still left without any voltage for 12 hours to 24 hours to stabilize the environmental conditions. At the end of this period, the voltage is switched on at the selected stress level and throughout the prescribed test duration.

Method (b), a dry test, instead, consists in covering the module's glass surface with a grounded conductive electrode (*e.g.* an aluminum plate) while the module is kept at 25°C and a RH of less than 60% for 168 h.

In both methods, the module leads are short circuited and a negative voltage is applied to the cells by means of a high-voltage supply (Iseg ECH 224), while the frame is grounded (see Figure 2.8).

The two methods differ not only in the stress conditions but also in the type of degradation induced in the module. In Method (a), the high temperature enhances the sodium ions diffusion within the module, while in Method (b) it is the presence of a conductive material all over the module surface that accelerates the PID process. In Method (a), the climatic conditions are such that there is no condensation layer on the module glass, even if the high air humidity can provide a conductive pathway over the glass surface. As a consequence, this test tends to stress less in the center of the module and the PID is more pronounced close to the edges. Such PID pattern, with the cells in the module edges more degraded than those in the center, is frequently observed in PID-affected modules outdoors, mostly in temperate climates. On the other hand, in Method (b) the cells degrade more uniformly independently of their position in the module. Such degradation has been observed in some installations located in hot and humid climates. In general, results of Method (b) are harsh compared to the degradation found in the field, and are more difficult to correlate with real outdoor climatic conditions, as there is no direct assessment of the impact of humidity on PID.

In this thesis, we make use of climatic chambers (a WEISS C180-40 and an ATT DY250) and apply Method (a). We chose this method because it allows us to evaluate the effect of ambient relative humidity on the power degradation, thereby providing useful information for modeling the evolution of PID for modules exposed to real outdoor conditions.

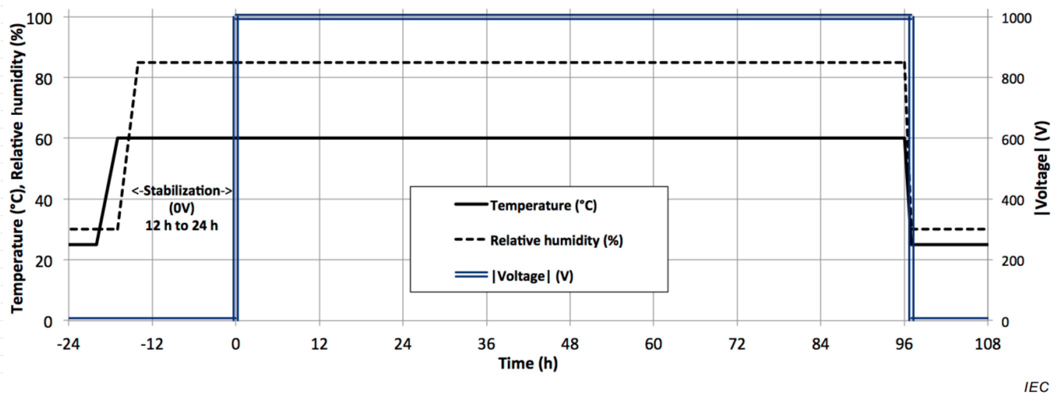

Figure 2.7: Profile of the stress factors – temperature, relative humidity, and voltage – during the PID test in a climatic chamber as prescribed in IEC TS 62804, Test Method (a) [59].

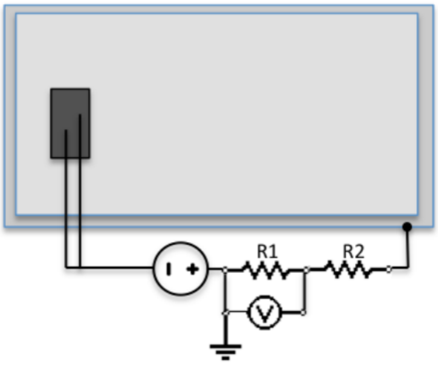

Figure 2.8: A voltage is applied to the short-circuited module leads that replicates the system voltage. The module’s frame is grounded. The leakage current is measured by a voltmeter across a resistor R1 of known resistance. A second resistor R2 may be added to protect the voltmeter from over-voltage. Picture reproduced from [40].

3 Potential-Induced Degradation

This chapter is an introduction on the topic of potential-induced degradation (PID). It is an introduction to the experiments and modeling of PID that will be presented in Chapters 4 to 6.

We first give evidence of the occurrence of PID in PV plants and explain the importance of addressing this topic to improve PV module reliability.

We then describe in Section 3.2 the physical mechanism that leads to the power degradation, by reporting the most widely accepted physical model for PID in c-Si cells. The multiple factors that may lead to the appearance of PID in a PV plant, such as the electrical layout of the installation or the module mounting system, are listed and briefly described.

Because PID is a reversible process, *i.e.* a module's degraded power can regenerate under some specific circumstances, we describe in Section 3.3 the physical mechanism behind regeneration according to the most accepted physical model.

The current IEC testing procedure to assess the PID resistance of commercial PV modules already presented in Chapter 2 is further discussed in Section 3.4 with reference to the use of the test for the prediction of PID outdoors.

In the last section, we give an overview of the main predictive models for PID available in the literature and anticipate the main elements of novelty of the model we present in Chapters 4 and 5.

3.1 Introduction and motivation

Among the different failure mechanisms that can affect PV modules, the so-called potential-induced degradation (PID) has caught much attention in recent years as it can be particularly detrimental. PID is a critical issue for PV plant reliability as the degradation of a module's power output can be rapid and severe. As reported in [8], module power losses of up to 27% were detected in a PV plant in Spain after only 4 months, while in a PV plant in southern Italy the modules' power degradation reached 50%. For this work, we retrieved field inspection data from a large owner of PV plants, where inspection reports revealed module power losses of up to 66% in a PV plant in Greece (as shown in Figure 3.6) and of even 85% in an installation in central Italy. Both the PV systems were in operation for less than 3 years.

The effects of PID in a PV plant are not visible to the naked eye, which might be one reason why it went mostly unnoticed until recently. The rising awareness of the problem has led to an increased number of reported cases of PID in PV plants worldwide. The growing system size, making PV modules operate at higher voltages, is another reason for the increasing frequency of the phenomenon. While PID was first observed mostly in hot or coastal climates, in the last few years it has been reported in moderate climates too [8]. The map in Figure 3.1 (from [10]) shows some c-Si technology PV plants in Europe affected by PID.

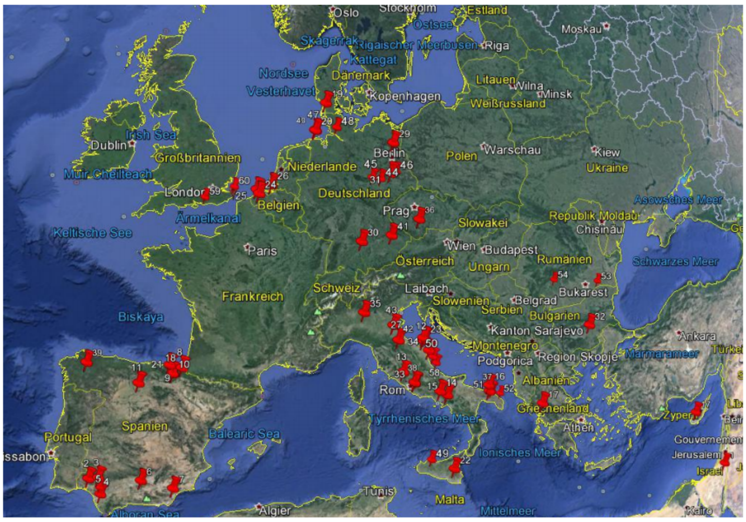

Figure 3.1: PV plants in Europe affected by PID and the subject of study by PI-Berlin. This image shows that PID was detected in various regions in Europe having different climatic conditions, but it does not provide any quantitative information on the impact of the phenomenon on the performance of the PV plants. Image from [10].

Depending on the module or cell technology, different forms of PID can occur. (An exhaustive review is given in [97].) A phenomenon of module performance degradation caused by the electric potential was reported in 1985 by the Jet Propulsion Laboratory for both c-Si and amorphous silicon (a-Si) thin-film modules. NREL also conducted numerous studies in the early 2000s on the risks related to high-voltage bias on different types of modules (see e.g. [23]). In *thin-film* modules, PID is attributed mostly to sodium ion migration within the module materials towards the semiconductor layer. This leads to charge recombination [160] or, in presence of moisture, to non-reversible electrochemical corrosion of the transparent conductive oxide (TCO) layer between the front glass and the cell surface [105]. In 2005, Swanson *et al.* [144] discovered a degradation induced by high voltages for *n-type* back-contact c-Si cells in Sunpower modules. This specific mechanism was called the surface polarization effect. In 2010, some works by Pingel and Hacke ([129] and [33]) started to clarify the physical mechanism of PID for the standard technology of *p-type* c-Si cells, and introduced the term “PID”. The PID process that occurs more often in p-type cells is a PID of the *shunting type*, sometimes denoted by PID-*s*. Other types of PID in p-type cells are the dissolution of the anti-reflective coating and the corrosion of the cell fingers [33].

In this thesis, we focus on the most deleterious and frequent type of PID for p-type c-Si cells, which is the shunting-type PID, and from now on we always refer with the term “PID” to the PID-*s* mechanism exclusively. The physical phenomenon behind this degradation mode is reviewed in Sections 3.2 and 3.3.

After the first publications on PID, especially [129] and [33], PID has generated a considerable interest in the PV reliability community and has been intensively investigated. Some research groups examined the phenomenon and investigated it at the microscopic scale (see [6], [83], [115], [90], among others), while others focused on developing suitable testing procedures to reproduce PID in the laboratory (e.g. [40], [35], [84], [10], [109]). We comment further on the PID testing procedure, already presented in Chapter 2, in Section3.4.

3.2 The physical mechanism of performance degradation

We give in this section an overview of the physical mechanism of PID in the mainstream technology of p-type c-Si cells.

PID occurs when a potential difference between cells and other module materials induces a migration of ions between the semiconductor material and other elements of the module. The higher the potential difference, the stronger the degradation of the module performance.

In a PV plant, modules are commonly connected in series, in groups called strings, in order to increase their total voltage output. In the standard case of framed c-Si modules, the module frame is typically grounded, for safety reasons, while the module (*i.e.* the set of cells) operates at a certain voltage relative to ground that depends on the module’s position in the string. This voltage difference between the cells and the frame may give rise to leakage currents, caused by mobile ions in the electric field, inside the module materials (see Figure 3.2).

Conventional p-type cells, in particular, are sensitive to negative voltages with respect to ground. The physical mechanism is shown more in detail at the cell level in Figure 3.3. The most widely accepted explanation of the physical mechanism behind PID assumes that sodium ions, Na^+, play a major role in the process (see [33], [40], and [6] among others). The driving force for PID is the electric field $\vec{E}$ in the anti-reflective coating layer SiN_x, caused by the potential difference between the cell and the frame. Such field $\vec{E}$ drives Na^+ from the external surface of the anti-reflective coating layer SiN_x towards the interface with the bulk silicon Si, where they accumulate in the SiO_x layer. From there, they may diffuse into the bulk silicon, mainly through favored diffusion paths given by stacking faults (*i.e.* crystal defects), causing shunts when such stacking faults penetrate the p-n junction [110].

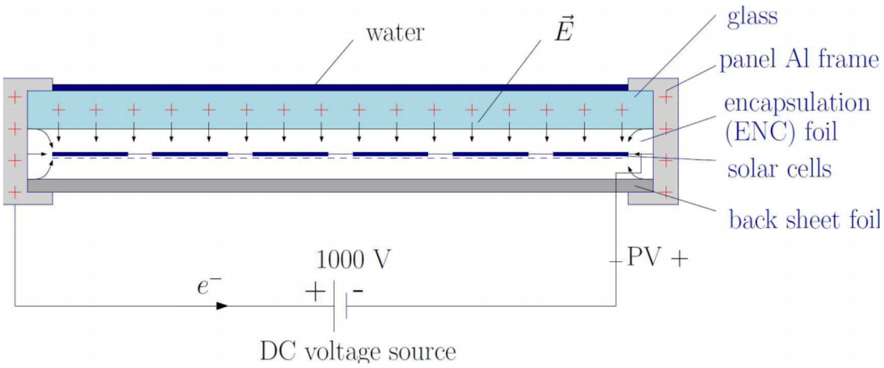

Figure 3.2: Illustration of the physical mechanism causing PID, at the module level. Image from [129].

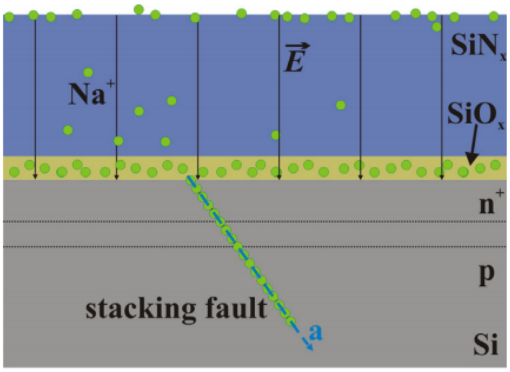

Figure 3.3: Close-up illustration of the PID mechanism inside a p-type c-Si cell. The image is a schematic representation of a cross-section of the cell. The driving force for PID is the electric field $\vec{E}$ in the anti-reflective coating layer SiN_x, caused by the potential difference between the cell and the frame (see Figure 3.2). Such field $\vec{E}$ drives Na^+ from the SiN_x layer towards the interface with the bulk silicon Si. From the SiO_x they diffuse (as Na atoms) into stacking faults. If the Na concentration in a stacking fault that crosses the p-n junction reaches a certain level, a shunting will be caused. Image reproduced from [115].

The factors leading to PID are multiple and related to the PV plant at various levels:

1. Module design aspects related to the mounting solution (such as the presence or absence of a frame or of back rails).
2. The electrical layout (*i.e.* mostly the grounding and polarity) of the PV array/string.
3. The inverter choice.
4. Module materials (encapsulants, solar cells, glass, backsheet, etc.) used in the fabrication of the sandwich.

5. The climatic conditions of the installation site.

We briefly discuss each of these points in the following subsections.

3.2.1 Role of the module mounting solution

As mentioned, the grounding of the metallic module frame is the reason for the appearance of PID. The potential difference between cells and the frame is the highest for the cells next to the frame while it decreases away from the module perimeter due to the glass surface resistivity. However, if the glass surface resistivity is reduced by factors like the presence of a water film (dew or rain), salt particles, or soiling, then the ground potential of the frame may be more uniformly distributed over the module surface, therefore exposing a wider portion of cells to a high potential difference to ground. In recent years it has been observed, through electroluminescence imaging in fielded modules, that in dry climates the PID occurs mainly on the edge cells, while in humid conditions the PID-affected cells are distributed more uniformly in the module (see e.g. [10]).

Hacke *et al.* performed accelerated PID tests on 60-cells commercial modules with different mounting designs [36]. The authors find that modules with a modified frame placed on only two edges degrade slower that modules with a standard four-edge frame, and that a third module design, with fiberglass rear support rails as the mounting system and no metal frame, does not degrade at all even after very long test (22 days).

Mounting structures alternative to the four-edge frame, such as for example the use of clamps, could constitute a solution to prevent or mitigate PID. With regard to new applications of PV technology, especially building integrated photovoltaics (BIPV) as well as some new lightweight solutions where the glass is replaced by lighter materials like a polymeric frontsheet, we remark that modules are generally frame-less and therefore less susceptible to PID.

3.2.2 Role of the PV plant's electrical layout

During its operation, each module is affected not only by its own operating voltage (of the order of the module V_{mpp}, generally around 30 V for a 60-cell module), but also by the cumulative voltage of the previous serially connected modules in the string. Considering that the maximum system voltage allowed in Europe is 1000 V and in U.S. 600 V, this translates into cell-frame voltage differences of potentially hundreds of volts (for modules at the extremity of a string). As already mentioned, since there is no perfect insulation between the frame and the cells, this high negative bias causes a leakage current within the module materials, which can have a detrimental impact on module performance.

The electrical layout of the PV plant is therefore an important factor for PID, in particular the length and polarity of the strings. In Figure 3.4 we show the possible grounding schemes available depending on the possibilities provided by the inverter (this aspect is addressed in Section 3.2.3). In Figure 3.5 we report from [129] an interesting electroluminescence (EL) image of a string with floating potential, which shows clearly that the module degradation is more pronounced moving towards the positions exposed to a higher negative potential relative to ground.

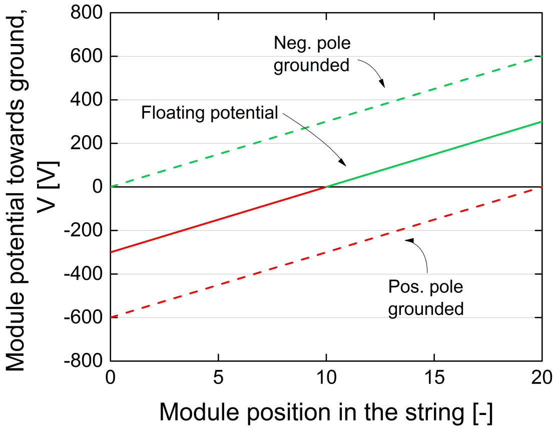

Figure 3.4: Module voltage as a function of its position within the string, for the three possible grounding schemes: negative or positive pole grounded, and no grounding (floating potential). Image re-adapted from [129].

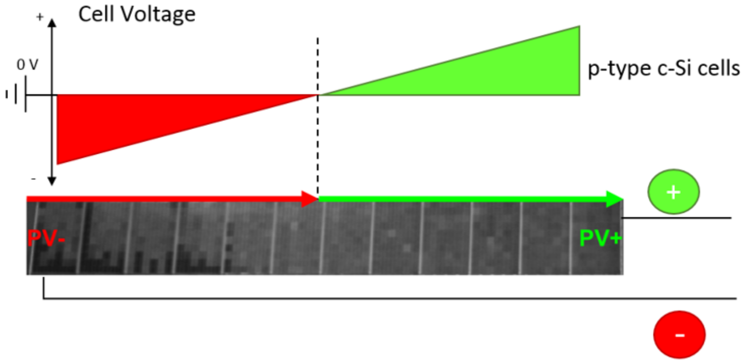

Figure 3.5: EL image of a string with floating potential (image adapted from [129]). PID-affected modules are on the negative side only, and the strongest degradation is observed for modules at the string's extremity (*i.e.* with the greater negative voltage towards ground).

Another case of PID in the field is shown in Figure 3.6, where the measured $P_{\max}$ is plotted against the module voltage for two strings of the PV plant. These data, which were shared by a private company, concern an open-rack PV system in Greece. It is striking that such modules, installed for less than three years, show such extreme levels of degradation, of up to 66% of their $P_{\max}$. As a first approximation, the dependency of relative power on (negative) voltage can be described as linear (see the dashed line in Figure 3.6), a relationship that we also obtain from our accelerated tests in Chapter 4. However, in general it is more difficult to identify a pattern because of the variability among the module's performance that might follow, for instance, from the cell variability (defects in the silicon that could lead to the formation of stacking faults), the presence of degradation modes other than PID, or from the actual use of different material formulations in the modules.

The current trend of the PV industry to increase the maximum system voltage to 1500 V [100] is an additional source of concern, and further justifies the effort to understand PID and to find countermeasures to its appearance [14].

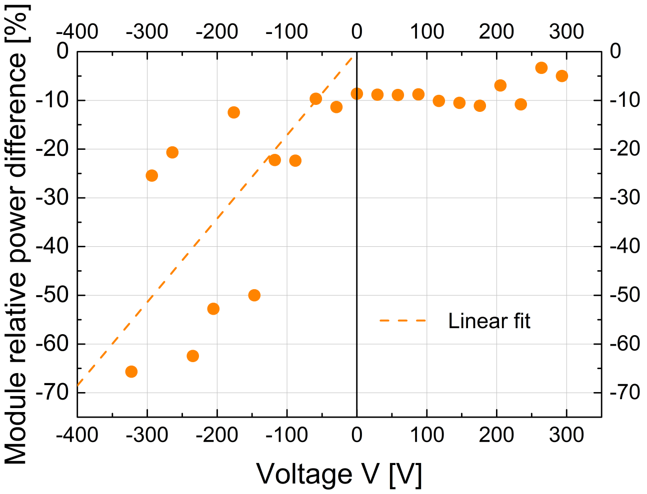

Figure 3.6: Module power loss with respect to the nominal power as a function of the module voltage for a string with floating potential. Data were shared by a company and refer to an open-rack PV system in Greece).

3.2.3 Role of the inverter

If a transformer-based inverter is used, which allows for grounding of the negative or positive system pole, PID can be prevented in p-type modules by grounding the negative pole. However, transformer-less inverters are increasingly employed in the PV industry, which results in a floating potential in which part of the modules in the string are negatively biased with respect to ground (see Figure 3.4).

3.2.4 Role of the module materials

PID is the result of a shunting of the solar cell caused by stacking faults penetrating the p-n junction and that become decorated with sodium. Naumann *et al.* found that the stacking faults are not necessarily already present in the cell but can be formed during PID stress, and they grow through penetration of Na. The authors hypothesized that stacking faults develop in correspondence to surface defects on the silicon surface. The quality of the silicon is therefore of primary importance for the prevention of PID. Moreover, such sensitivity to cell surface defects make PID very cell-dependent and brings to a high variability in cells resistance against PID. Modules of the same type can indeed show different susceptibility to PID, as it is the case for some of our tests in Chapter 4. Often a high variability in the degradation of the single cells in a module is observed, and can be seen for instance in the electroluminescence image in Figure 3.9, where for example the cells in the module perimeter did not degrade all the same way.

The origin of the Na^+ was also largely investigated in the last few years. While it was first speculated that Na^+ originate from the soda-lime glass used as front cover, it was later found that Na (or other metals) ions in the glass are in fact not necessary for PID. Indeed, Na^+ can already be present at the cell surface, as the result of contamination of the solar cell during the manufacturing process. In Ref. [114] the authors showed that PID can occur at bare silicon solar cells without the use of a glass cover.

In fact, the driving force for PID is the electric field $\vec{E}$ in the anti-reflective coating SiN_x layer, which causes the drift of Na^+ through the SiN_x layer (see Figure 3.3). The stronger this electric field, the stronger the possible degradation of the cell performance. The strength of such field results from the potential difference between the cell and the frame, and from how such potential difference is distributed over the various electrical paths for the ions within the module (given by the glass and the front encapsulant). As explained in [112], the electric field in the SiN_x layer can be assumed, with some assumptions, to be linked to the leakage current $\vec{J}$ by

$$\vec{E} = \vec{J} \cdot \rho_{SiN}$$

where ρ_{SiN} is the resistivity of the SiN_x layer. A detailed explanation of the relationships between leakage current and material properties is provided in Ref. [112]. What we want to highlight here is that there exist different approaches at the materials level to reduce the electric field $\vec{E}$.

- One approach is to reduce the leakage current $\vec{J}$. This can be achieved by employing materials that limit the mobility of ions, namely using a glass with increased resistivity (e.g. sodium-free glass) or an encapsulant with increased resistivity. As discussed in Section 3.2.2, leakage currents can also be prevented at system level by avoiding high negative voltage bias of the cells with respect to the module frame.
- The second approach is to act at the cell level, by reducing the resistivity ρ_{SiN} of the SiN_x layer. Indeed, if the SiN_x layer had a low electronic conductivity this would cause a reduction in the mobility of the drifting ions, with a consequent pile up of charges at the SiN_x surface. This charge pile up would increase the potential across the SiN_x, enhancing the drift of existing Na^+ across the SiN_x layer. On the contrary, a SiN_x with high electronic conductivity would allow the leakage current to drain away without building up a high voltage.

In particular, we point out that the effect of a sodium-free glass is twofold. On the one hand the amount of Na^+ available for PID is reduced. On the other hand, as mentioned, thanks to a higher glass resistivity the leakage current is reduced and so is the electric field in the SiN_x layer. In this case, even if the sodium resulting from the contamination of the solar cell surface was enough for causing the PID effect, the reduced electric field $\vec{E}$ would limit the drift of such ions towards the interface with the bulk silicon (see Figure 3.3).

The role of the encapsulant material is also fundamental. Encapsulant materials with high resistivity such as polyolefin or ionomer have been shown to prevent or significantly delay the occurrence of PID compared to standard EVAs ([94], [9]). We address this aspect in Chapter 6, where we evaluate the PID resistance of different combinations of materials in the module (cell, encapsulant, and rear cover).

PID can be critical for many of the solar parks built in the early phase of PV deployment (2000–2012), however it can still occur in modern modules when lower grade materials are used in PV manufacturing (e.g. encapsulants), a choice often driven by the need for cheap solar electricity.

3.2.5 Role of the climatic conditions

PID is strongly dependent on the climatic conditions in which modules operate. High temperatures accelerate the phenomenon due for example to reduced resistivity of the glass and the encapsulant material. As discussed in Section 3.2.1, high relative humidity conditions, rain events, or the presence of dew over the module surface also lead to harsher degradation by making the glass surface equipotential to the frame. We address these points in Chapter 4, where we investigate with accelerated testing the relationship between power loss and the environmental stress factors. In Chapter 5 we then simulate the PID for modules installed in sites with different climatic conditions.

3.3 The physical mechanism of performance regeneration

A peculiarity of PID with respect to other degradation modes is that it is reversible. The module shunt resistance and thus the power can indeed recover, partly or completely, under certain weather conditions. The reversibility holds for the PID of the shunting type (the focus of our thesis) but does not apply to the other degradation modes related to high potential such as the corrosion of the metallic fingers.

Some studies on samples exposed outdoors (see [81] among others) showed that regeneration (or recovery) can happen:

- at night, when the cells' operating voltage is null. We refer to this case as regeneration in the dark or thermal recovery;

- during hot and dry days (regeneration during light exposure), when the low conductivity of the glass surface limits the leakage currents and the high potential difference remains limited to the cells in the perimeter of the module.

Power recovery can also be induced by applying a positive voltage bias between the cells and the grounded frame during the night by means of dedicated electrical devices [130]. In the remainder of this section we describe these three kinds of power recovery from PID.

3.3.1 Regeneration in the dark

At night, in the absence of a voltage, regeneration is purely a diffusion mechanism, therefore driven by temperature. This process of thermal recovery was extensively examined in the last few years, with major contributions especially by Lausch and Naumann from Fraunhofer CSP. By means of microscopic investigations, they proved that thermal recovery is due to diffusion of the Na^+ out of the stacking faults [91]. In the absence of a bias voltage, indeed, the Na^+ current towards the cell surface stops and the Na atoms diffuse from the stacking fault back into the oxide (SiO_x) layer where now the Na concentration is lower (see Figure 3.7). Once in the silicon oxide layer SiO_x, Na spreads laterally. Diffusion of Na into the SiN layer can also take place (and Na converts to Na^+ again), even if the diffusivity of Na in SiN is lower than in the SiO_x. The thermal recovery process was also studied through accelerated laboratory testing, where previously degraded modules are tested in conditions of regeneration. For instance, in [93] an equation for regeneration in the dark, with no bias voltage, as a function of the temperature is proposed.

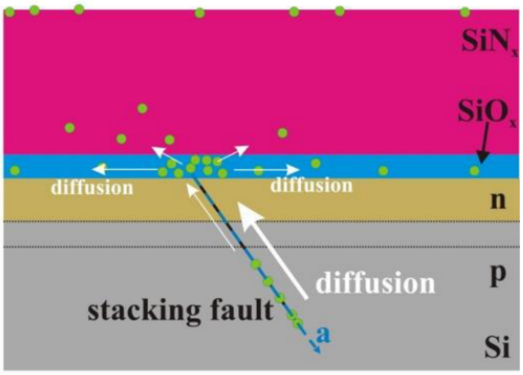

Figure 3.7: Schematic drawing of a p-type c-Si cell cross-section and illustration of the physical mechanism of thermal recovery from PID. The Na atoms diffuse out of the stacking faults back into the oxide (SiO_x) layer, where they spread laterally. They may also diffuse into the SiN layer (and convert to Na^+ again), a slower process. The white arrows indicate the paths of the Na^+ and Na atoms (green circles). Image reproduced from [91]

3.3.2 Regeneration during light exposure

The mechanism of recovery that occurs during the day, when the cells are exposed to negative voltages towards ground, is less known. In [82], the authors show that regeneration can be affected by irradiance. We further analyze the regeneration mechanism in Chapter 4 by reproducing in the laboratory the power recovery under irradiance and with applied negative voltage. The complex interaction between degradation and regeneration still requires further investigation, and one aim of our work is to improve the understanding of this aspect and of how to model it in simulating the performance of PV modules outdoors.

3.3.3 Methods to recover PID affected modules in the field

In addition to the previous power recovery processes, which occur during natural operating conditions, methods to artificially recover modules affected by PID in a PV plant exist.

- One method consists in applying a high positive voltage (e.g. +1000 V) to the modules (see e.g. [130]). As proposed for solar cells in [91], the process that allows for power recovery can be explained with the out-diffusion model also in this case. Indeed, in correspondence to the positive voltage applied, an electric field results inside the SiN_x layer and is such that the Na^+ accumulated at the interface between SiN_x and bulk Si (*i.e.* in the SiO_x) are driven out of the Si bulk, towards the cell surface. The reduction of Na^+ concentration at the interface inverts the concentration gradient between the interface and the stacking faults decorated by Na, which now starts to diffuse out of the stacking faults. With respect to a purely thermal recovery, the process of out-diffusion with a reverse bias applied is accelerated because a greater concentration gradient of Na is induced.

  Some industrial products (“offset kits”) are available on the market use this principle and apply a positive voltage to the full module string during the night (e.g. iLUMEN’s PID box [60] or Pidbull [128]). The module power is thus recovered during the night, thereby limiting the impact of PID.

- Another method to recover degrade modules or strings is to proper ground the strings: by grounding the negative pole of the inverter all the modules would be exposed to a positive potential relative to ground (see Figure 3.4). However, this is not possible when the inverter is transformerless, a topology that is increasingly employed in the PV industry.

The effectiveness of these methods was analyzed in some recent studies. For example, in [47] the authors compared the recovery ability of PID-affected strings of modules treated with the first and second method. They found that the grounding solution proved less efficient than the use of anti-PID devices. All the modules treated with the anti-PID device showed a power recovery over the 70 days of test, even if in some cases the level of recovery was lower than expected and in partial contradiction with the device supplier announcements. In particular, the recovery for the severely degraded modules was very slow, which highlights the importance of an accurate monitoring of PV plants for an early detection of PID.

A drawback for the use of such anti-PID devices is primarily the addition of costs. Secondly, it has been pointed out that applying a high voltage to modules always induces leakage currents that may cause other degradation modes in the modules, such as electrochemical corrosion [38].

In this work, we are interested in studying and modeling the natural evolution of PID. The use of these recovery devices will therefore not be considered. We will on the contrary focus on the thermally-driven power recovery that occurs during the night (Section 4.2.2) and at daytime (Section 3.3.2). From the methodology that we propose in Chapters 4 and 5, starting from indoor accelerated tests on a given module type it is indeed possible to predict the effect of PID on the module in normal operating conditions in the field. In the planning phase, these predictions should allow an investor to evaluate whether a given PV module type is suitable to resist PID for a specific climate condition. The need of recovery devices would increase the OPEX and therefore the LCOE of the PV plant. Additionally, no information about the performance and safety of these kits on the long-term is generally available. Further experience is thus required before envisaging a large-scale adoption of these devices. Moreover, as mentioned, if PID is detected in field modules at an advanced state, the use of recovery devices might not be sufficient to recover the module performance to its initial level. The use of modules resistant to PID is therefore recommended, and in Chapter 6 we treat this topic in detail by identifying combinations of materials that allow us to manufacture modules with good resistance against PID.

3.4 PID: accelerated stress test

The ability of a module to withstand high system voltages is currently assessed by means of the accelerated tests prescribed by the IEC Technical Specification 62804-1:2015 [59]. The stress conditions of the Method (a) test (the method used throughout this thesis) originated from the case of a module design that degraded by 5% during the test (with a bias voltage of −600 V applied) and showed a similar range of degradation in the Florida environment for over 28 months with the same bias voltage applied during daylight [36].

Even though this testing procedure is very effective in reproducing PID effects on PV modules, it does not provide sufficient information to predict the performance of the modules in the field. It presents, indeed, the typical limitations of any *qualification* test that were discussed in Chapter 1.1. Modules that degrade by the same amount during the PID test might exhibit different values of power loss in different climatic conditions, as our simulations of outdoor PID in Chapter 5 indicate. As pointed out in the TS [59]: “The actual durability of modules to system voltage stress will depend on the environmental conditions under which they are operated. These tests are intended to assess PV module sensitivity to PID irrespective of actual stresses under operation in different climates and systems."

Some module manufacturers have started to sell modules labeled as "PID-free", meaning that the module exhibited a power variation of less than −5% after the PID test. However, "PID-free" is a purely commercial label as the PID testing TS [59] does not provide any threshold in the power loss that guarantees that the module will not suffer from PID in the field. In addition, some modules that are sold with such label by some Tier 1 companies were shown not to pass the proposed standard test. We purchased indeed a commercial module type labeled as being "PID-free" under 85°C/85% RH. After the test at the same conditions and with the standard value of voltage bias (−1000 V), we measured a power variation of −69% (see Figure 3.8a), by far stronger than the value of −5% considered as the limit to be labeled "PID-free". The module does not prove to be "PID-free" even at 60°C (Figure 3.8b).

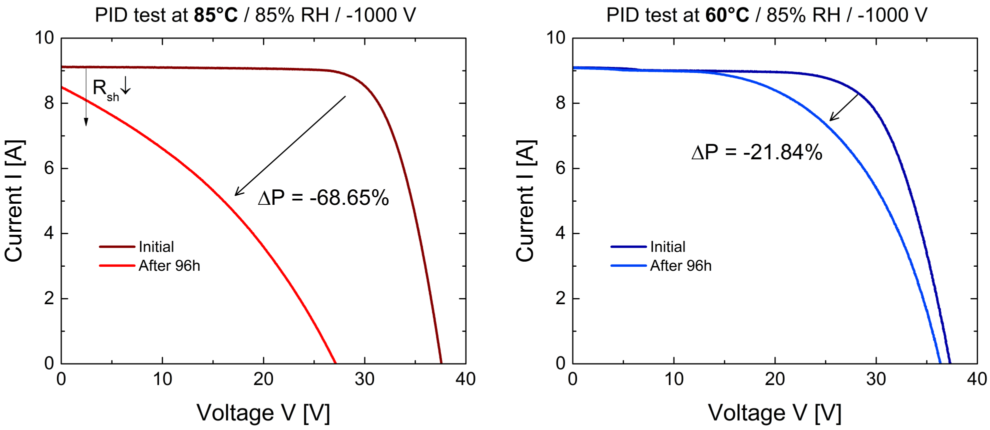

(a) (b)

Figure 3.8: Two commercial modules, of the same type, that are sold by a Tier 1 company as "PID-free" at the 85°C/85% RH condition, were tested in our laboratory with −1000 V voltage bias applied for 96 h and at two environmental conditions. (a) IV curves of the module before and after the test at 85°C/85% RH show instead a power loss of ∼ −69%, much larger than the limit of 5% considered as threshold to be labeled as "PID-free". The power loss is mainly due to a reduction in the shunt resistance R_{sh}, confirming that the test actually reproduces the typical effect of PID. (b) The module does not prove to be "PID-free" even at 60°C.

The shunting effect typical of PID is evident in the EL pictures of the module after the test as shown in Figure 3.9.

In Chapter 4 we start from the Method (a) test to build a matrix of tests at different stress levels, in order to develop a lifetime model for PID that allows us to simulate PID in different climates.

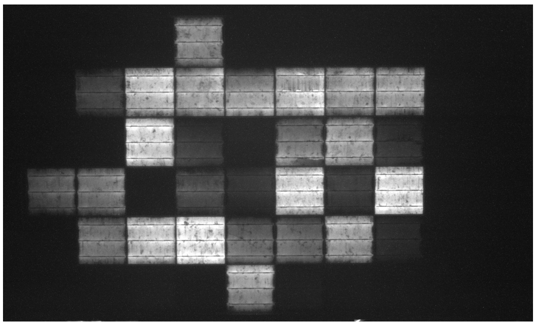

Figure 3.9: EL image of the module tested at 85°C / 85% RH / −1000 V / 96 h, related to the IV curves in Figure 3.8a. This image illustrates that the PID test actually reproduces the effect caused by PID, as the degradation mode detected from this image is a darkening of the cells that is a consequence of shunting.

3.5 Modeling PID

3.5.1 An overview of the different attempts to model PID

Empirical models of PID based on indoor accelerated aging testing have been proposed in recent years (see [97] and [52] for a review). The models express the PID effect as a function of the four stress factors, and have been used to predict PID in real outdoor conditions.

In [50], Hoffmann and Köhl derive a model for the module leakage current. Leakage currents on the order of microamperes are indeed present in modules subjected to PID testing, and are known to be linked to relative humidity and temperature. However, the correlation between the leakage current and the power degradation is not clear, as we also show from results of our accelerated tests in Chapter 4.

Taubitz *et al.* in [146] model the time evolution of the shunt resistance R_{sh} of one-cell mini-modules during indoor testing at high temperature. When a voltage of −1000 V is repeatedly switched on and off, the shunt resistance is found to experience three phases: a shunting phase under bias voltage, a transition phase when the bias is switched off, and a consequent regeneration phase. This model shows quite a good correlation when compared to outdoor measurements of the R_{sh}, however a quantification of the module power degradation is not explicitly provided.

Koch *et al.* also develop a model for the shunt resistance, for which a logistic function is employed to describe the degradation process and an exponential function for the regeneration [82].

Hattendorf *et al.* propose a PID model based on the module maximum power P_{mpp} [45]. A matrix of accelerated degradation tests at different stress levels is performed, assuming that the stress factors for the power degradation are the applied voltage, the temperature, the ambient relative humidity, and the time. The degradation curves follow a sigmoid shape, reaching a stabilization level — dependent on the value of the applied voltage — after which the power stops degrading. The same authors investigate the regeneration mechanism in [44] by subjecting pre-degraded modules to tests with no applied voltage. The regeneration model they extract describes the temperature-driven power recovery in dark conditions with no bias voltage. The final predictive model including both degradation and regeneration has 10 parameters to be determined experimentally. It is finally applied to simulate PID in outdoor conditions in different climates.

In 2015 [37], Hacke *et al.* extracted a model based on accelerated degradation testing that does not include the regeneration mechanism. In this case the power loss is described as parabolic in time and its dependency on temperature and humidity is based on the Peck equation.

3.5.2 The contribution of this work

Even though the understanding of PID has made important progress since the issue was first identified, some aspects still need to be further investigated. Our work addresses two areas: the prediction of module power degradation in different climates and the identification of module materials (e.g. cell, encapsulant, backsheet) combinations that prevent or limit the occurrence of PID.

About the first point, we propose a mathematical model to predict PID as a function of the stress factors (T, RH, and voltage), which takes into account both the degradation and the regeneration processes. The model we present here contains new aspects with respect to those described above. First, we investigate the regeneration mechanism under irradiance and with applied bias voltage with accelerated testing and obtain a set of equations to model it. To the best of our knowledge, this issue was not addressed before. Our predictive model is therefore able to treat with two different equations the power regeneration that occurs at night and the one that, under some specific conditions, takes place during daytime. Moreover, we improve the understanding of the influence of weather especially by integrating a condition for the module surface to be wet. In contrast with some previous approaches, we use a mathematical adaptation that allows a consistent way to apply the equations, obtained at indoor constant conditions, with real outdoor conditions, where the stress factors (weather) vary continuously. This approach also allows us to consider the environmental stress factors with a time resolution of one hour, in contrast with some other works where for example day average values are used.

With regard to the role of module materials in PID, we test mini-modules manufactured with different combinations of cell, encapsulant and rear sheet materials and show that, for instance, the use of PID-free cells is not always the best option to prevent PID. We also investigate the role of the rear sheet as well as the impact of water ingress into the sandwich on the occurrence of PID.

3.6 Structure of the chapters on PID

Our discussion of PID develops in the following three chapters as illustrated in the diagram in Figure 3.10. Each block of the diagram will be further developed in the corresponding chapter. To briefly anticipate, Chapter 4 and 5 concern, respectively, the development of a predictive model for PID obtained from indoor laboratory testing, and the application of the model to simulate the power evolution of modules in various climates.

First, in Chapter 4 we present the experimental work performed in order to develop a model of PID as a function of its stress factors. Results of accelerated degradation tests at different stress levels are shown, from which we deduce an equation that describes the power degradation at constant stress conditions and the values of the relative parameters for our samples. We then present two sets of tests that we carried out in order to investigate, respectively, regeneration at night and regeneration during the daytime. In this case as well, we deduce a mathematical equation to describe these mechanisms at constant stress conditions, and extract the parameters for our module type. In Chapter 5, we apply these equations to simulate the power performance in outdoor conditions, using weather data as inputs as well as the parameter values from the accelerated tests. In Chapter 6 we continue our investigation into PID with a closer study on the role that module materials and their combination play in preventing PID.

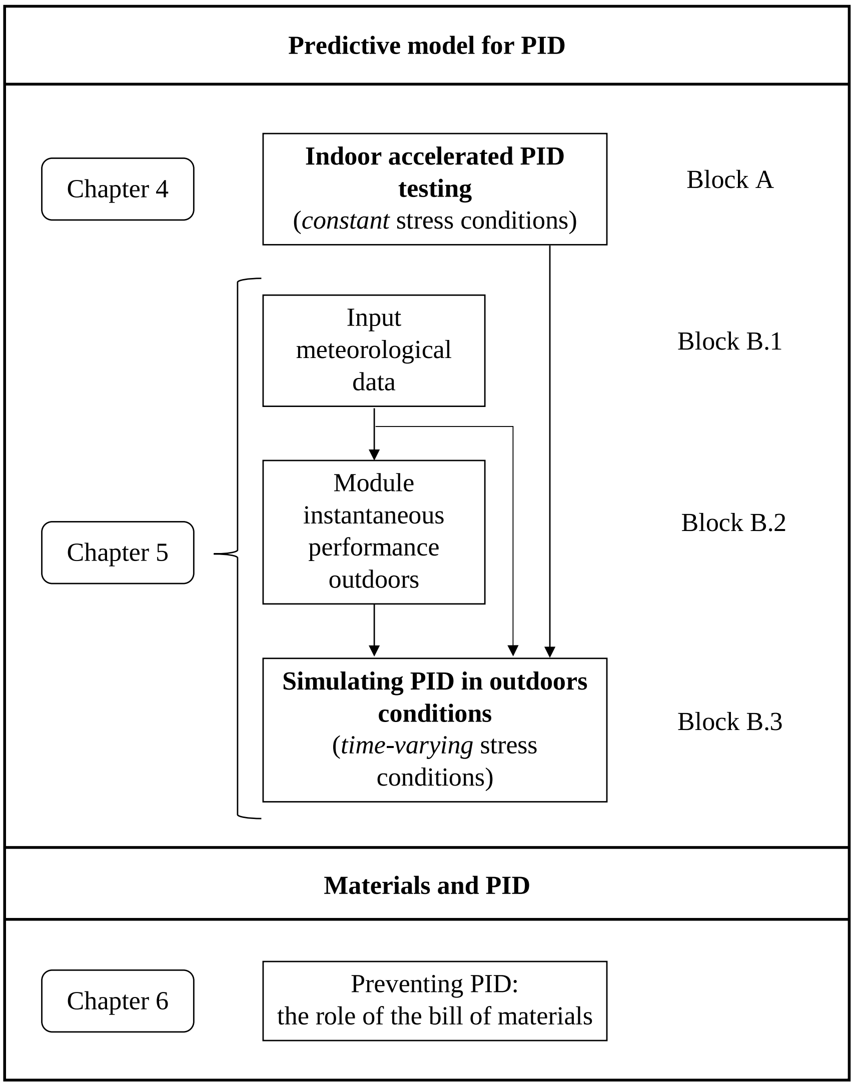

Figure 3.10: Flowchart visualizing the structure of the chapters dedicated to the topic of PID.

4 PID: Indoor accelerated testing at constant stress conditions

In this chapter, we develop empirical equations that describe PID as a function of the stress factors. This is done by performing a matrix of accelerated tests at different stress levels on two-cell mini-modules. The equations we obtain describe PID at constant stress conditions, as it is the case during indoor testing. In Chapter 5 we employ these equations to develop a model that predicts PID in real outdoor conditions, and the parameters extracted here are used as inputs in our simulations. Both the degradation and the regeneration mechanisms are investigated experimentally in this chapter.

The leakage current, used by some authors as a physical quantity representative for PID, is not found to be strictly correlated with the performance loss, and we decide to consider instead the mini-module maximum power P_{max} as the physical quantity to model.

Concerning the degradation mechanism, we perform a matrix of tests at different combinations of the stress factors (temperature, relative humidity, voltage, and time) and derive a dependence of the P_{max} on temperature, relative humidity, and time in agreement with that proposed by Hacke *et al.* in 2015 for 60-cells commercial modules. Here, we add the influence of the applied voltage, a key parameter for predicting the PID in field modules, where the extent of voltage varies depending on the module position in the string.

The regeneration (or recovery) mechanism is investigated by means of two sets of tests. First, we expose degraded samples to different temperatures in the dark with no voltage applied, in order to reproduce the recovery occurring in the field during the night. We obtain an exponential dependence of the recovery on T in the form of what proposed by Lechner *et al.* in 2015 [93]. Secondly, we contribute to the understanding of the regeneration during light exposure and clearly show that, when the ambient conditions are favorable (high temperature and low relative humidity), a power recovery can occur even for samples exposed to very high negative voltages. We finally derive an equation for power recovery during light exposure.

The equations obtained in this chapter hold for stress conditions that remain constant in time. As mentioned, we then apply these equations and their parameters in Chapter 5, where we simulate what the effect of PID would be if these mini-modules were exposed to real outdoor stress conditions continuously varying in time.

The structure of this chapter and its relation with Chapter 5 is illustrated in Figure 4.1.

The results in Section 4.1 were included in the conference proceeding in Ref. [2] and some of the results in Section 4.2 were presented in [4].

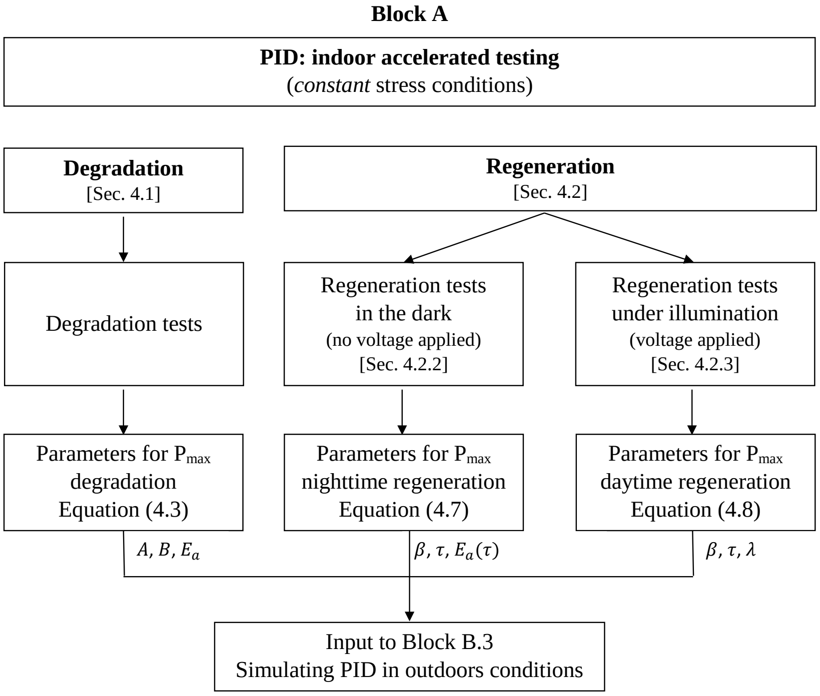

Figure 4.1: Outline of the chapter. The parameters of the PID degradation equation, A, B, and E_a are defined in Section 4.1 and in Table 4.2. The parameters for regeneration, $\beta, \tau, E_a(\tau)$, and λ are defined, respectively, in Section 4.2.2, Table 4.3 and in Section 4.2.3, Table 4.6.

4.1 A mathematical model for PID: power degradation

In this section, we derive an equation that describes the power loss of a module due to PID as a function of the main stress factors for PID: temperature T, relative humidity RH, voltage V, and time t.

4.1.1 Experimental work

The experimental tests described in this chapter are done on two-cells mini-modules such as that depicted in Figure 4.2. Testing such mini-modules (size 20 cm × 40 cm) in place of full-size commercial modules (typically 100 cm × 160 cm) offers the clear advantage that a larger number of samples can be tested simultaneously to collect sufficient data in a non-prohibitive time.

The mini-modules are manufactured with a standard lamination process as presented in 2.1. All the samples are encapsulated with a 3-mm-thick, 200 mm × 400 mm solar-grade soda-lime glass at the front, and a 0.360-mm-thick polymer-based sheet at the rear (backsheet). Each mini-module consists of two monocrystalline silicon p-type cells with a single p-n junction. Before lamination, we manually solder three ribbons (standard copper-based and tin-coated) over the three busbars of the cells and connect the two cells in series. The encapsulant material is a standard EVA (ethylene vinyl-acetate) for PV applications, from Bridgestone (EVA model S88). The backsheet is from Dunmore, model PPE+, and is comprised of two layers of polyethylene terephthalate (PET) laminated to a single layer of adhesion-promoting film. After different trials on ways to simulate the presence of a metallic frame (by *e.g.* covering the entire surface or only edges with an aluminum (Al) foil as in [136], we decide to use an electrically conductive aluminum tape on the four sides, as done for instance in [50].

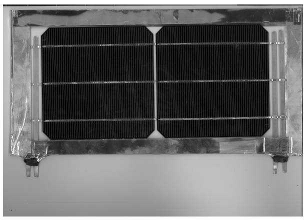

Figure 4.2: Example of a two-cell mini-module used for our PID tests. The aluminum tape simulates the frame assuring a good and homogeneous adhesion on the glass surface.

To degrade their performance, the mini-modules are tested in climatic chamber according to the procedure prescribed by the IEC TS 62804-1:2015-08 [59] and described in Chapter 2. In order to model the contribution of each stress factor, we vary the stress levels in each test sequence, as illustrated in Table 4.1. Between two and four samples are tested at each stress condition. Moreover, the test duration is extended from the 96 h prescribed by the TS to 192 h in order to gain more information on the degradation process. Electrical parameters of the mini-modules are determined (i) initially, (ii) after 96 h, and (iii) at the end of the test, by means of IV measurements at standard test conditions (as described in Chapter 2.2.1).

Throughout this section, the mini-module's initial maximum power (*i.e.* before the degradation) is denoted by P_{ini}; the maximum power at time t by $P_{\max}(t)$, or simply $P(t)$ in the plots; the power loss at time t is defined as $\Delta P := P_{\text{ini}} - P(t)$.

Table 4.1: Matrix of accelerated-aging test conditions to investigate PID dependence on temperature T, relative humidity RH, and voltage V. Duration of all tests is 192 h, and the bias voltage applied to the cells with respect to the grounded frame is −1000 V. Tests at 85°C / 85% RH are repeated with additional bias of −600 V, −400 V, and −200 V. Between two and four samples were tested at each condition.

T/RH	65%	75%	85%	95%
45°C			−1000 V	
60°C	−1000 V	−1000 V	−1000 V	−1000 V
85°C			−1000 V −600 V −400 V −200 V	

4.1.2 Leakage current

In an initial phase of the PID investigation, some authors proposed the leakage current flowing through the module as a possible indicator for PID ([50, 15]). It is well documented that the leakage current increases at higher temperature, higher ambient humidity and with the module's surface wetness. However, some studies ([62, 36]) show that the leakage current is not always proportional to the actual power degradation, and is therefore not a good indicator of PID when the focus is performance prediction.

Nevertheless, we measured the leakage current during our tests to validate our test setup. In agreement with published studies, the leakage current demonstrates an Arrhenius dependence on temperature (see Figure 4.3). The activation energy we determined equals 0.69 eV, well in line with the published values in [136] for their one-cell mini-modules. Also the leakage currents absolute values are very similar. We should mention that leakage current values up to 10 times higher were also reported in [50] for their 4-cells mini-modules. Such a difference can be attributed not only to the different module size (accumulated charge) but also to the use of a different bill of materials (glass, encapsulant, and cell type).

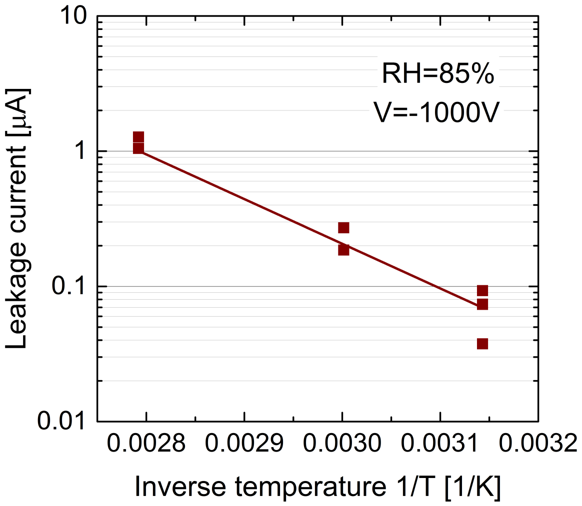

Figure 4.3: Semi-log plot of the leakage current measured on our mini-modules tested at 85% RH and −1000 V, as function of the inverse of the temperature. An Arrhenius behavior is observed.

In addition, we confirmed that a higher leakage current is indeed not always correlated with a stronger power loss, as shown in Figure 4.4.

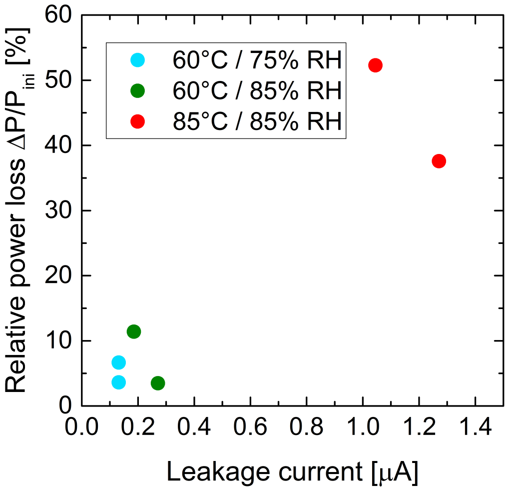

Figure 4.4: Power loss after 192 h of PID test versus leakage current (obtained as the average of the leakage current measured all over the test duration): no correlation is observed.

4.1.3 Temperature

As documented in several studies, [36] among others, temperature is one of the degradation factors for PID. Indeed, at high temperatures both the glass surface and the encapsulant become more electrically conductive, which facilitates the ion migration from the glass to the cell. The experimental tests performed in this work show an Arrhenius dependence of the power loss on temperature (see Figure 3). The activation energy E_a we derived for the power loss is 0.86 eV.

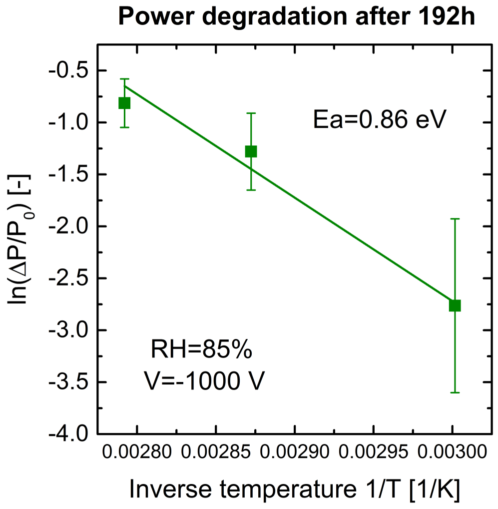

Figure 4.5: Normalized power loss after 192 h of PID test at 85% of RH and −1000 V applied. Error bars denote the standard deviation. An Arrhenius behavior is deduced with respect to temperature, with an activation energy E_a of 0.86 eV.

4.1.4 Relative humidity

A complete description of PID requires modeling the effect of relative humidity on the power loss. Monitoring of modules in outdoor conditions reveals a strong degradation during periods of high relative humidity ([81], [50]). Relative humidity affects the process of PID in different ways.

1. It is known that the electrical conductivity of glass depends on the air relative humidity [11]. In dry conditions, the PID mainly affects the cells close to the module edges, as they are more equipotential to the grounded frame than the cells in the center of the module. The higher the conductivity of the module glass (humid conditions), the more the ground potential of the frame is distributed over the glass surface. This leads to high leakage currents also for the cells in the center of the module, and the PID effect on the module is stronger as it concerns more uniformly all the cells. A particularly harsh case is when a water film is created over the glass. In [81], for instance, outdoors PID measurements revealed a relevant reduction in shunt resistance together with high values of leakage currents during the mornings, when water condenses on the module surface, and during rainy days.
2. Under humid conditions, moisture can penetrate into the encapsulant material, reduc-

ing its resistivity and thus accelerating the Na ions transport through the material.

3. For EVA encapsulants, moisture is also considered to be related to PID in that it can result in formation of acetic acid, which enhances the release of ions from the glass [153], [143], [119].

Here, we perform PID tests on two-cell mini-modules at different relative humidity levels in order to model the dependence of the power degradation on RH. We assume that the main effect of RH on PID during the 192 h of our tests is mainly the one in point 1 (*i.e.* increased glass surface conductivity at high RH), and we suppose the effects in points 2 and 3 negligible.

In Figure 4.6 we show the results of our tests by plotting the power loss against the RH level. Even though results present some variability, we can describe the dependence of power loss on RH with a polynomial curve (see Equation (4.3) in Section 4.1.7). We observe that the value of RH=40% appears to be the minimum RH level to detect an effect of PID, at least after 192 h of testing at these stress levels. We apply this consideration in our simulations of PID on modules in operation in Chapter 5 as a criterion to distinguish the phase of power degradation and power regeneration during daytime hours.

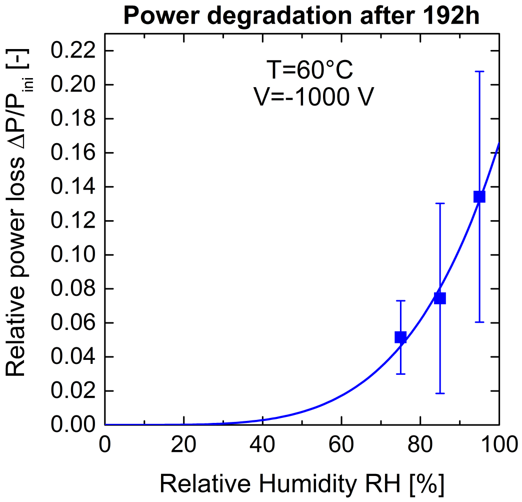

Figure 4.6: Normalized power loss after 192 h at 60°C and −1000 V exhibits a polynomial dependence on relative humidity.

4.1.5 Time

As mentioned, mini-modules are characterized by means of IV curve measurements before the test and after 96 h and 192 h in climatic chamber. In agreement with what found in [37] for commercial modules, the evolution of the maximum power of our mini-modules is quadratic in time, in our case at least during the first 192 h, as shown in Figure 4.7 and reported in Equation (4.3).

This parabolic function provides a good description of the initial phase of the PID curve. Some authors (*e.g.* [45]) showed that for long testing times the power rather follows a logistic function behavior, tending to stabilize to a minimum value. However, describing the power time evolution with a parabolic function, although with some mathematical limitations, has the advantage of avoiding the need of very long accelerated tests and makes the realization of the whole test matrix for PID power degradation less prohibitive in terms of time costs.

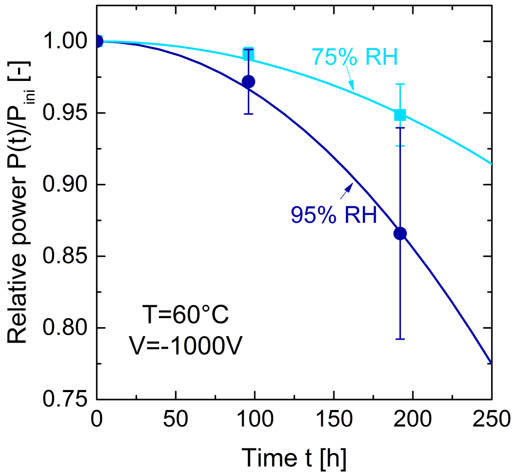

Figure 4.7: Evolution in time of maximum power P_{max} for some of the test conditions performed: the behavior in the first 192 h can be fitted with a quadratic curve.

4.1.6 Voltage

A necessary condition for the occurrence of PID is the presence of an electric field across the materials constituting the module sandwich. Several inspections on PV plants (we showed some examples in Chapter 3) clearly indicate that the degradation of modules within a string is stronger when moving towards higher negative potentials with respect to ground. This latter term is, therefore, needed to approach real field conditions, as field PID degradation will depend on the module's position within the string. Here, we perform tests at several voltage levels and observe that the power losses at a fixed time (*e.g.* after 96 h) vary linearly as a function of the applied voltage, as Figure 4.8 shows.

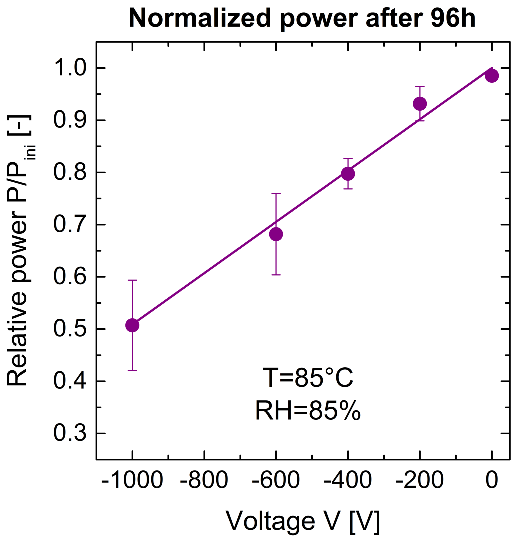

Figure 4.8: A linear behavior is observed for maximum power $P_{\max}$ after 96 h of PID tests at 85°C/85% RH as a function of the voltage.

4.1.7 Mathematical equation for the power degradation

We finally combine the effect of all distinct contributions and propose a simplified relation, Equation (4.1), describing the power degradation as function of PID at constant stress test conditions:

$$\frac{P_{\max}(t)}{P_{\text{ini}}} = 1 - C_V \cdot V \tag{4.1}$$

where $P_{\max}(t)$ is the module's measured maximum power after t hours of exposure to constant stress levels, P_{ini} is the initial power, and C_V is a coefficient for the voltage, which includes the effect of T, RH, and t. The coefficient C_V represents the equation previously proposed by Hacke *et al.* in [37], which was established based on PID tests on commercial modules with 60 monocrystalline silicon p-type cells. We recall this relationship hereunder in the form of Equation 4.2, where $k = 8.6173 \cdot 10^{-5}$ eV·K^{-1} is the Boltzmann constant.

$$C_V(T, RH, t) := A \cdot V \cdot RH^B \cdot e^{-\frac{E_a}{\kappa \cdot T}} \cdot t^2 \tag{4.2}$$

By fitting Equation (4.1) for our mini-modules, we obtain the following values for the parameters: $A = 6.0188 \cdot 10^{-5}$ h$^{-2}V^{-1}$, $B = 4.43$ [-], and $E_a = 0.86$ eV, reported in Table 4.2. Note that E_a is interpreted here as the activation energy of the power loss. Other authors concentrate, instead, on the activation energy of the time to reach a certain level of power loss (what we define here “time to failure”). It is possible to mathematically verify that Equations (4.1) and (4.2) imply that the activation energy of the power loss is twice the activation energy of the time to failure. Values reported by Hacke *et al.* in [37] and Raykov *et al.* in [136] are 0.85 eV and 0.75 eV respectively: this would therefore mean an activation energy of 1.7 eV and 1.5 eV for the power loss. We conclude that the value of 0.86 eV obtained by us is lower compared to the mentioned references. Reasons for this might lie for instance in the particular type of encapsulant employed or in the samples configuration (*e.g.* sample size, shape, etc).

To conclude, for a mini-module with initial maximum power P_{ini}, subjected to constant temperature T, relative humidity RH, and voltage V, the maximum power $P_{\max}$ at time t is given by the following equation, which has the form of a classic Peck model with a linear contribution of the voltage:

$$P_{\max}(t) = P_{\text{ini}} \cdot \left(1 - A \cdot V \cdot RH^{B} \cdot e^{-\frac{E_a}{\kappa \cdot T}} \cdot t^2\right). \tag{4.3}$$

Table 4.2: The parameters obtained for Equation 4.3 describing the power degradation due to PID.

A [$\mathrm{h}^{-2}V^{-1}$]	B [-]	E_a [eV]
$6.0188 \cdot 10^{-5}$	4.43	0.86

4.1.8 Summary

We subjected test devices (two-cell mini-modules) to accelerated PID tests at different stress levels. From the matrix of tests, shown in Table 4.1, we developed an empirical mathematical model that describes the power degradation as a function of the main PID stress factors, *i.e.* temperature, relative humidity, voltage, and time. On the one hand, tests results suggest that mini-modules behavior can be described by the model that Hacke *et al.* developed in [37] for commercial modules, based on the Peck model where in particular the power degradation is described with a parabolic behavior over time. On the other hand, we contributed to the modeling of power degradation by adding a term that describes the dependence of degradation on voltage, obtaining the final expression in Equation (4.3). The values of the parameters appearing in Equation (4.3), reported in Table 4.2, are extracted by fitting the experimental results, and are specific to the mini-modules considered here in the accelerated testing.

4.2 A mathematical model for PID: power regeneration

In this section, we complement the model presented above by including the contribution of a regeneration term. First, we subject two-cell mini-modules to PID tests in order to degrade their performance. Then we use a similar approach as the one used for modeling the degradation: regeneration tests are performed at different conditions, from which we extract an empirical equation describing the recovery of the maximum power $P_{\max}$. The same method is used in other contributions, *e.g.*, [93] and [44]. As mentioned, one contribution of our work is to analyze of the regeneration process that occurs during light exposure, when samples are exposed to negative voltages towards ground resulting in an interaction between the degradation and the regeneration mechanisms.

4.2.1 Experimental work

For the regeneration tests we use the same type of coupons employed in the degradation tests, *i.e.* two-cell mini-modules laminated at PVLAB, of size 20 cm × 40 cm. All samples feature the same materials as those described in Section 4.1: commercial mono crystalline silicon p-type cells, soda-lime glass at the front, a polyethylene-based backsheet, and a commercial EVA as encapsulant material. The same electrically conductive aluminum tape is placed on the four sides to simulate the presence of a metallic frame.

All the samples for regeneration tests are prepared with the same processes, the same bill of material, and in a single batch. To degrade their performance, we subject the mini-modules to PID tests in climatic chamber at 85°C and 85% RH (or 85/85). The temperature is increased to 85 °C instead of the specified 60 °C in order to accelerate the degradation. The mini-modules are characterized electrically by IV measurements initially (the initial power is denoted by P_{ini}) and at the end of the degradation tests (96 h, $P_{\min}$). After the degradation, the same mini-modules are subjected to regeneration tests. On the one hand, to investigate the regeneration occurring at night, tests are performed at different temperatures in dark and with no applied voltage (Section 4.2.2). On the other hand, to reproduce daytime regeneration (that may occur during hot and dry periods), the samples are exposed to different irradiance levels (Section 4.2.3). We also investigate for the first time the effect that load conditions (open-circuit (OC), short-circuit (SC), and maximum power point (Mpp)) have on the regeneration under light exposure. We do this to investigate regeneration under conditions close to those experienced by modules in a field (Mpp vs OC). In addition we simulate the effect of applying a negative bias voltage to the samples during the exposure to light at high temperature.

4.2.2 Regeneration in the dark

For the study of nighttime recovery, we subject pre-degraded mini-modules to recovery in dark. Regeneration tests are performed in an oven, at different temperatures and under dry conditions (RH around 8%). Samples are kept in open-circuit conditions.

Let us define, as done by Lechner *et al.* in [93], the relative recovery at time t as:

$$RR(t) := \frac{P_{\max}(t) - P_{\min}}{P_{\text{ini}} - P_{\min}}, \tag{4.4}$$

where we recall that P_{ini} and P_{min} are the mini-module maximum power at, respectively, the beginning and the end of the degradation test. We obtain the following relation for the relative recovery as a function of the temperature, see Figure 4.9, in agreement with the results obtained in [93] (on commercial 60-cell modules):

$$RR(t) = 1 - \exp\left(-\left(\frac{t}{\tau(T)}\right)^{\beta}\right), \qquad \text{where } \tau(T) = \tau_{\text{ref}} \cdot \exp\left(-\frac{E_a(\tau)}{\kappa} \cdot \left(\frac{1}{T} - \frac{1}{T_{\text{ref}}}\right)\right). \tag{4.5}$$

The parameter β seems to be independent from temperature and has an average value of 0.55 [-]. The parameter τ [h] follows an Arrhenius law with respect to temperature T (expressed in [K]), with an activation energy E_a of 0.52 eV (κ is the Boltzmann constant [eV/K]). A summary of the parameters found from the fittings is given in Table 4.3.

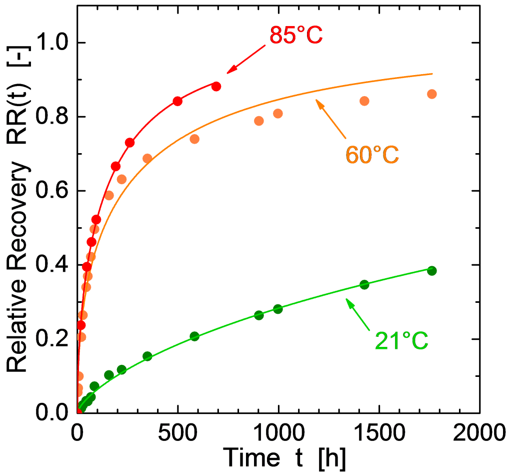

Figure 4.9: Relative recovery over time for mini-modules during indoor testing in the dark at different temperatures, with fitting curves according to Equation (4.5).

Table 4.3: The parameters obtained experimentally on our mini-modules for Equation (4.5) describing the relative recovery in the dark.

T [°C]	τ [h]	$E_a(\tau)$ [eV]	β [-]
21	4805.79	0.52	0.55
60	277.65		
85	137.87		

The fact that higher temperatures induce a faster power recovery is consistent with the theory of the regeneration as an out-diffusion process of Na atoms from stacking faults in the pn junction. As previously suggested in [93], this indicates that, under dry conditions, power regeneration might be more pronounced during daytime, with higher temperatures, than during nighttime, even in the presence of a negative applied bias to the modules. This is the main motivation for the work presented in the next section.

4.2.3 Regeneration during light exposure

Here we aim at modeling the effect of irradiance on power recovery. As for regeneration in the dark, all the samples are pre-degraded in climatic chamber at 85/85/ −1000 V for 96 h. The recovery is then performed at different irradiance levels, in dry conditions (relative humidity around 15%) in a temperature-controlled light-soaking chamber (Hönle sun simulation system, a solar simulator of class C for spatial homogeneity). The temperature can be set in the range of 40°C to 60°C and can vary during operation with an error of ±5°C.

Effect of load conditions

While the samples regenerating in the dark are kept at open-circuit conditions, here we want to reproduce the conditions in which field modules are kept during daylight. For this reason, we apply to some of the samples a negative voltage (simulating modules at the negative extreme of a string). In order to assess the impact on regeneration of irradiance only, other samples are left with no voltage applied. Additionally, for a specific set of conditions (1000 W/m^2, 60 °C, - 1000 V) we investigate the effect of load conditions as well, by exposing the modules, respectively, in short-circuit (SC), open-circuit (OC), and, by applying a resistive load, maximum power point (Mpp). The experimental matrix is summarized in Table 4.4.

Table 4.4: Experimental matrix for the first set of tests to investigate the regeneration mechanism during light exposure. Temperature T is the set chamber temperature.

T [°C]	Irradiance [W/m^2]	Load conditions	Voltage [V]
60	1000	PID (SC)	−1000
		SC	/
		OC	/
		Mpp	/
	800	PID (SC)	−1000
		Mpp	/
	640	PID (SC)	−1000
		Mpp	/

Figure 4.10 shows the recovery over time of the samples regenerating under 1000 W/m^2 at different load conditions. On the left (Figure 4.10a), the complete power evolution is shown,

with the initial degradation induced by the PID test and the subsequent regeneration at low humidity. Two samples were tested per each condition but only one representative sample per condition is shown for the sake of clarity. A slight difference among the samples can be seen in the regeneration speed and in the extent of maximum recovery. This difference is more clear if we look at the relative recovery, plotted in Figure 4.10b. For instance, samples in OC conditions show the strongest recovery, which we tend to ascribe to the slightly higher temperatures (a few degrees) experienced by these devices.

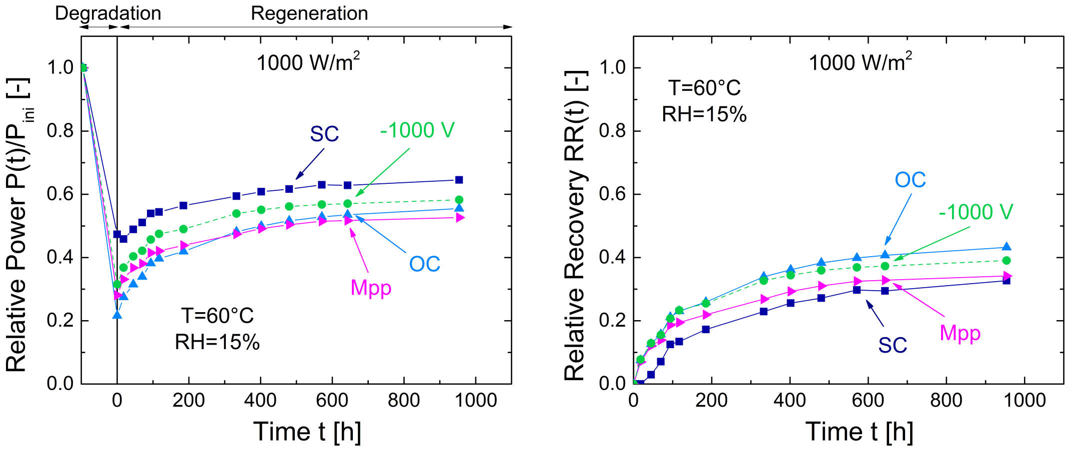

(a)

(b)

Figure 4.10: (a): Power evolution of mini-modules normalized to their initial power (before degradation). PID degradation is performed at 85 °C / 85% RH / −1000 V for 96 h. Regeneration starts at time 0 h, with samples exposed to 60 °C and at different load conditions. Relative humidity was low to enhance the regeneration (around 15%). Lines are a guide to the eye. (b): Relative recovery, defined in Equation (4.4), referred to the same samples as in the figure on the left.

Note that, under these test conditions, even samples with a high negative applied voltage are regenerating. This means that daytime regeneration can occur in the field even for modules in strings exposed to high negative voltages towards ground, at least when humidity is low or in the absence of rain. A recovery of the performance during hot and dry periods was also observed in [81], where the shunt resistance of a mini-module kept at −1000 V negative bias voltage first decreased in the early morning hours under humid conditions, followed by an increase (corresponding to a recovery) during hot and dry hours. This phenomenon can find an explanation in the frame of the theory for PID regeneration. Indeed, when the glass surface is dry it becomes less conductive and as consequence the leakage current through the module materials drops. If it is low enough, the electric field across the SiN layer is reduced, and the out-diffusion process of Na out of the stacking faults can take place and prevail over the inwards drift of Na ions that would cause performance degradation.

Effect of irradiance

Regeneration under different irradiance levels is shown in Figure 4.11. Dotted lines are for samples with −1000 V applied, while full lines represent samples in Mpp conditions. The effect of irradiance on the power regeneration seems not to be very pronounced. For the same samples, also the values of relative recovery, as defined in Equation (4.4), suggests that irradiance may have a secondary relevance in promoting the regeneration compared to load conditions (see Figure 4.11 on the right).

In addition, even if – in order to avoid contradictory results – particular care has been dedicated in sample processing (same bill of material, processes, and processing time), the samples show different level of degradation or "pre-damage" (*i.e.* not all samples degrade by the same amount), as can be seen in Figure 4.11 (left). This variability then translates into different levels of recovery or of relative recovery (plot on the right in Figure 4.11). As we show later on for another set of tests, the level of degradation has a considerable impact on the recovery. It is indeed widely observed (and reported in the literature, e.g. [44]) that the samples undergoing a more severe degradation tend to recover less.

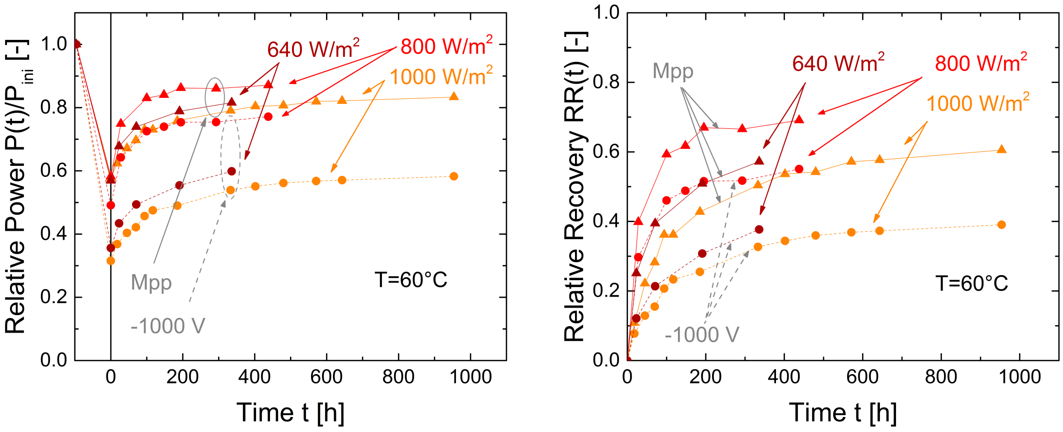

(a)

(b)

Figure 4.11: (a): Power evolution of mini-modules normalized to their initial power (before degradation). PID degradation is performed at 85 °C / 85% RH / −1000 V for 96 h. Regeneration starts at time 0 h, with samples exposed to 60 °C and different irradiance levels. Relative humidity was low to enhance the regeneration (around 15%). Lines are a guide to the eye. Dotted lines are for samples with a −1000 V bias voltage applied, full lines are for samples in Mpp conditions. (b): Relative recovery for the same samples as in the figure on the left.

Effect of temperature

A second set of tests is then performed to further understand the mechanism of power regeneration under irradiance by investigating the role of temperature. Here again, two-cell mini-modules are first subjected to power degradation at 85/85/ −1000 V and subsequently exposed to irradiance. The irradiance level is fixed at 1000 W/m^2, and temperature and applied voltage are varied according to the experimental matrix in Table 4.5. The temperature of each sample is monitored throughout the test with PT100 sensors placed on the samples' backsheet.

Table 4.5: Experimental matrix for the second set of tests to investigate the regeneration mechanism during light exposure. Temperature T is the sample temperature.

Irradiance [W/m^2]	T [°C]	Voltage [V]
1000	40	−1000
	50	
	60	−400
		−600
		−1000

In Figure 4.12 we show the relative recovery RR of the samples regenerated at different temperatures (time $t = 0$ h is the time at which the regeneration test starts). Values for the conditions at 40°C and 60°C are the averages of two samples, the bars representing the standard deviations; values for the condition at 50°C refer instead to one sample only.

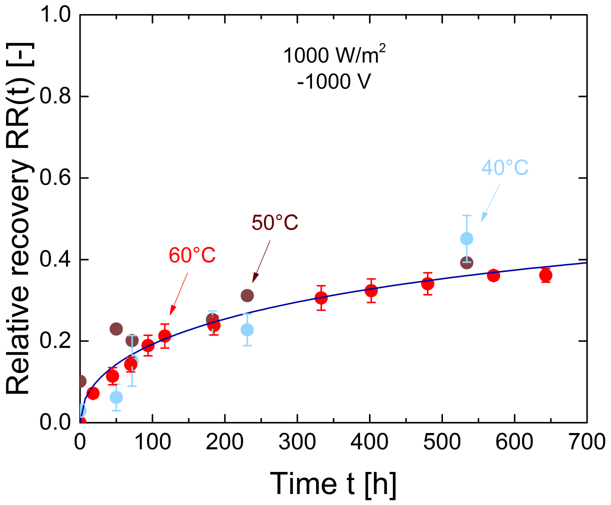

Figure 4.12: Relative recovery of samples exposed to 1000 W/m^2 / −1000 V at different temperatures. The values at 50°C refer to one sample only, while for the 40 and 60°C the values are averages of two samples, the error bars indicating the standard deviations. The dependence of the RR on temperature is not very clear from these results, and we approximate the three sets of data (at 40, 50, and 60°C) with the same fitting function (blue curve).

The impact of temperature on RR is not very evident: even if samples at 40°C seem to regenerate faster than the others, the very slight difference between the three sets of values does not allow us to establish a model for the dependence of RR on temperature. We therefore deduce from these tests that the RR is independent of the sample temperature, and fit these datasets with one single curve. A good fitting is obtained with the following function:

$$RR(t) = \lambda \cdot \left(1 - \exp\left(-\left(\frac{t}{\tau}\right)^{\beta}\right)\right), \tag{4.6}$$

where the values extracted for the parameters are $\tau = 800$ h, $\beta = 0.50$ [-], and $\lambda = 0.65$ [-].

The fact that temperature does not have a pronounced effect on regeneration when a voltage is applied might be due to a counterbalance between the Na^{+} drift from the glass towards the cell surface (responsible for performance degradation and enhanced by high temperatures) and the temperature-driven out-diffusion of Na from the staking faults. Tests at a wider temperature range could possibly provide further information on this aspect.

Effect of voltage and of degradation level

For a fixed temperature of 60°C, we then regenerate samples applying different voltage levels. This is done to assess the distribution of the daytime recovery process as a function of the position of the module in a string. The results, in Figure 4.13, show that differently from what was expected the extent of voltage is not clearly related to the dynamics of the recovery process. For example, one of the two samples exposed to −400 V shows a slower relative recovery (plot on the right) than the samples exposed to −600 V and even than those at −1000 V. For the second sample with −400 V applied, instead, the RR curve follows closely the curves of those at −600 V.

By looking at the plot of the relative power (on the left in Figure 4.13), we see that the quantity that affects mostly the RR and in particular its maximum extent for $t \to \infty$ is the relative power at the end of the degradation period (*i.e.* the extent of the degradation). We observe that, for samples with a lower $P_{\mathrm{min}}/P_{\mathrm{ini}}$ (*i.e.* samples that degraded more), the RR occurs more slowly and tends to stabilize at a value $\lambda < 1$ meaning that the power will not fully regenerate to its initial conditions. By fitting these data with Equation (4.4) with the values for parameters τ and β previously found ($\tau = 800$ h, $\beta = 0.50$ [-]), we extract the parameter λ, and we attribute the difference in the value of λ to the pre-damage level exclusively. We draw a twofold conclusion from these data: (i) the voltage does not seem to affect the daytime regeneration, and (ii) the pre-damage level seems to be the quantity that affects the RR dynamics the most, in terms of both the speed and the maximum extent λ of recovery.

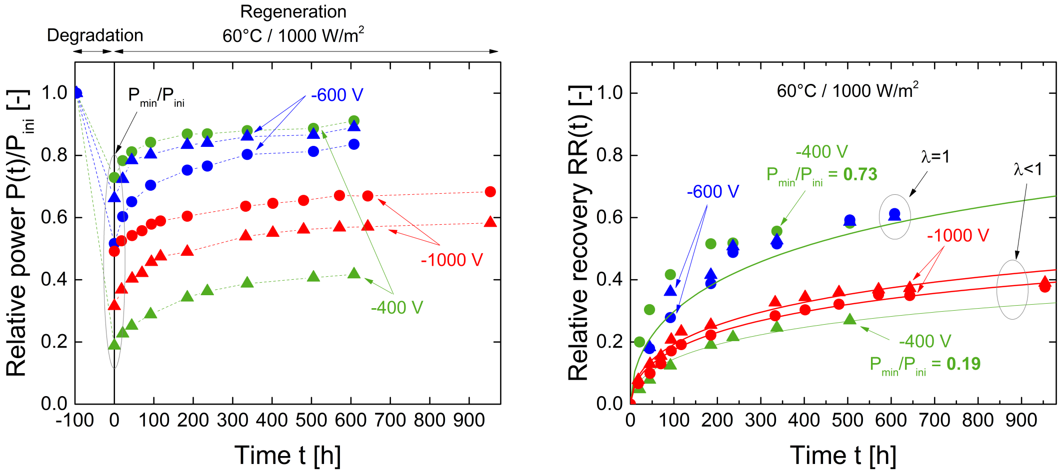

(a)

(b)

Figure 4.13: (a): Power evolution of mini-modules normalized to their initial power (before degradation). PID degradation is performed at 85 °C/ 85% RH / −1000 V for 96 h. Regeneration starts at time 0 h, with samples exposed to 60 °C, 1000 W/m^2 and different (negative) voltage levels. Relative humidity is low to enhance the regeneration (around 15%). Lines are a guide to the eye. (b): Relative recovery RR of the same samples. Lines are fittings with Equation (4.4). The top green curve is used to fit the three sets of values corresponding to the samples with the highest ratio $P_{\text{min}}/P_{\text{ini}}$ (plot on the left).

In view of the observation above, we look at the dependence of the parameter λ on the pre-damage. In Figure 4.14 the values of λ obtained from our fittings are plotted against the relative power at the end of the degradation $P_{\text{min}}/P_{\text{ini}}$. We find that, if the power at the end of the degradation is higher than 50% of the initial power, then the recovery will be complete at infinite time; otherwise, the maximum extent of recovery λ is <1 and we can approximate it with the relation $\lambda = 2 \cdot P_{\text{min}}/P_{\text{ini}}$.

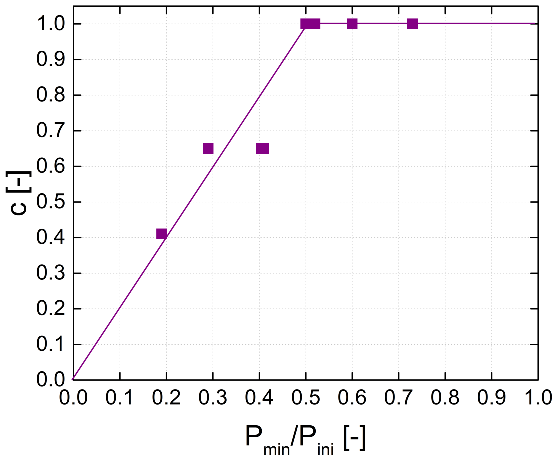

Figure 4.14: Maximum level λ of relative recovery (Equation (4.6)) as a function of the PID damage level of the sample at the beginning of the regeneration test (*i.e.* $P_{\mathrm{min}}/P_{\mathrm{ini}}$). Samples for which the degraded power was less than 50% of their initial power will not regenerate completely.

The values of the parameters obtained for the daytime recovery are summarized in Table 4.6.

Table 4.6: The parameters describing the relative recovery under irradiance.

τ [h]	β [-]	λ [-]
800	0.50	1, if $P_{\mathrm{min}}/P_{\mathrm{ini}} > 0.5$
		$2 \cdot P_{\mathrm{min}}/P_{\mathrm{ini}}$, if $P_{\mathrm{min}}/P_{\mathrm{ini}} < 0.5$

4.2.4 Mathematical equations for the power regeneration

We collect here the final equations that model the process of power regeneration in the dark and under light exposure.

Equation for the nighttime (dark) regeneration

$$RR(t) = 1 - \exp\left(-\left(\frac{t}{\tau(T)}\right)^{\beta}\right), \qquad \text{where } \beta = 0.55 \text{ [-] and}$$

$$\tau(T) = \tau(T_{\mathrm{ref}}) \cdot \exp\left(-\frac{E_a(\tau)}{\kappa} \cdot \left(\frac{1}{T} - \frac{1}{T_{\mathrm{ref}}}\right)\right), \text{ with}$$
$$E_a(\tau) = 0.52 \text{ eV}, \; T_{\mathrm{ref}} = 30 + 273.15 \text{ K}. \qquad (4.7)$$

Equation for the daytime (light) regeneration

$$RR(t) = \lambda \cdot \left(1 - \exp\left(-\left(\frac{t}{\tau}\right)^{\beta}\right)\right) \qquad \text{where } \tau = 800\text{ h},\ \beta = 0.50\ [\text{-}], \text{and}$$

$$\lambda = \begin{cases} 1 & \text{if } P_{\text{min}}/P_{\text{ini}} > 0.5 \\ 2 \cdot P_{\text{min}}/P_{\text{ini}} & \text{otherwise} \end{cases} \tag{4.8}$$

The final goal of this work is to model the evolution of the PID phenomenon and the impact on module performance as a function of different climatic conditions. In the next Chapter we apply the equations obtained from indoor testing (Equations (4.3), (4.7), and (4.8)), in combination with a set of input meteorological data for specific locations, to predict the time evolution of PID on modules in operation.

4.2.5 Summary

We analyzed by means of accelerated tests the mechanism of power recovery on mini-modules previously degraded in laboratory. In dark conditions (replicating nighttime recovery), our results are in agreement with [93]: power regeneration is promoted by higher temperatures and follows a stretched exponential law with a time coefficient that depends on temperature through an Arrhenius law (Equation (4.7)). The parameter values of the equation extracted for our mini-modules are listed in Table 4.3. Our contribution consists in investigating in greater detail the mechanism of power regeneration that occurs during daytime, when the modules are exposed to a negative potential towards ground. Our findings indicate that, under illumination (daytime recovery), the level of irradiance, temperature, and applied voltage do not seem to affect the recovery. The starting level of degradation of the samples plays, instead, a major role and the regeneration mechanism during daytime can, in conclusion, be modeled with a stretched exponential with a pre-factor that depends on the degradation level (Equation (4.8)). Table 4.6 reports the values of the daytime regeneration parameters obtained for our mini-modules.

4.3 Conclusion

In this chapter, we subject test devices (two-cell mini-modules) to accelerated PID tests at different levels of the stress factors. At each test condition, the stress levels are maintained constant throughout the duration of the test.

No direct correlation is found between the value of leakage current measured during the test and the final extent of power loss of the mini-modules. We therefore confirm that leakage current is not a good indicator of PID when the aim is performance prediction, and decide to consider instead the $P_{\max}$ as the physical quantity to model.

4.3.1 The power degradation

$P_{\max}$ of the mini-modules is measured initially and at fixed time intervals during the tests. We correlate the $P_{\max}$ degradation to each stress factor by obtaining the following empirical relationships.

1. With respect to temperature, the power loss after the degradation tests has an Arrhenius dependence, with an activation energy E_a of 0.86 eV.
2. The power loss is related to the relative humidity through a polynomial dependence.
3. The evolution of the maximum power of our mini-modules is quadratic in time, at least during the first 192 h. This is in agreement with [37] for commercial modules. Even if some authors observed a behavior similar to a sigmoid function, with a stabilization level at infinite time, here we assume that the power loss is parabolic, keeping in mind that this approximation might be good only in the initial phase of the curve. Using this model has the advantage of making the realization of the whole test matrix for PID power degradation less prohibitive in terms of time costs.
4. By performing tests at different voltage levels, we find that $P_{\max}$ varies linearly as a function of the applied voltage.

The relationships in points 1, 2, and 3 were previously proposed by Hacke *et al.* in [37] and were based on accelerated PID tests on 60-cell commercial modules.

Here, first we confirm experimentally this empirical model for two-cell mini-modules, and determine the values of the coefficients specific to our sample materials.

We then add a contribution in complementing the model by establishing the dependence of power loss on the applied voltage. This is a crucial factor for predicting the effect of PID in field modules, as the voltage to which a module is exposed during its operation depends on its position in the string.

We also observe that a RH of 40% appears to be the minimum level to detect an effect of PID. This observation is exploited in Chapter 5, where we simulate PID in outdoor conditions, as a threshold to establish if degradation or regeneration are taking place during daytime.

4.3.2 The power regeneration

With respect to the power regeneration process, the accelerated tests presented in this chapter lead to the following findings.

i. In the dark and with no voltage applied (conditions representative of nighttime recovery in the field), the power relative recovery RR is strongly promoted by high temperatures. A “stretched-exponential” function gives a good fitting of the experimental data, as also found by Lechner *et al.* in 2015 [93]. The dependence on temperature enters through an Arrhenius relationship for the time-related coefficient τ.

ii. Under illumination, and at low humidity:

   (a) Regeneration remarkably takes place as well for the samples exposed to a considerable high negative bias-voltage (-1000 V). In the field, this means that daytime regeneration can occur also for modules at the extremity of the negatively biased side of the string, provided the necessary ambient conditions are present (*i.e.* low humidity, high temperature).

   (b) The effect of temperature is less pronounced than for tests in the dark. A possible explanation may lie in a counterbalance between temperature-enhanced degradation (due to a lower resistivity of the encapsulant layer) on the one hand and thermally-driven out-diffusion of Na from the stacking faults (leading to performance recovery) on the other. We simplify the modeling by assuming that the temperature has no effect on the daytime regeneration.

   (c) According to our tests, a higher negative bias voltage is not always correlated to a slower regeneration. The voltage is then also assumed to have a secondary effect in the daytime recovery.

   (d) A major role on the power relative recovery is played by the degradation level of the sample. In particular, we determine a threshold of 50% of power degradation, such that mini-modules that degraded more than this amount are not going to fully regenerate.

The equations and parameters obtained here (Equations (4.3), (4.7), and (4.8)) are applied in Chapter 5, in combination with a set of input meteorological data for specific locations, to predict what would be the time evolution of PID for the same mini-modules if they were operated in real outdoor conditions.

5 PID: prediction of outdoor module performance as a function of climatic conditions

In this chapter, we apply the results obtained in Chapter 4 to simulate the occurrence of PID in real outdoor conditions. We consider the two-cell mini-modules that were subjected to accelerated PID test in Chapter 4, and simulate the effect that PID would have on such devices if they were installed outdoors. The empirical equations obtained in Chapter 4 are applied here with a set of meteorological data as inputs, together with the PID parameters extracted in Chapter 4 and characteristic of such devices. In order to assess the impact of climate on the evolution of PID, we perform the simulations in four locations, representative of four different climatic conditions.

First, we calculate in Section 5.2 the mini-module instantaneous nominal power, *i.e.* the mini-module performance in the absence of degradation, as a function of meteorological factors such as irradiance and temperature and of the electrical properties of the module type under study.

In Section 5.3, we define some thresholds on the meteorological conditions in order to properly simulate the different phases of PID. The implementation of the PID empirical equation obtained at constant laboratory conditions with time-varying stress factors as inputs (such as relative humidity and temperature) is not straightforward. We show a method, based on the concept of “equivalent time”, that allows us to apply our equations with varying stress levels in a mathematically consistent way.

In Section 5.5, we show the time evolution of the mini-module power with respect to PID resulting from our simulations. By comparing the results in the different geographical locations, we evaluate the impact of the climate conditions on the PID effect. An example of application of this model to the case of a string of commercial “full-sized” modules is then shown, where in particular the voltage that causes the PID is the actual instant voltage of each module as a function of the module position in the string.

The prediction model was developed for mini-modules and an adaptation to “full-sized” modules (*e.g.* 60-cell commercial modules) is not trivial. Nonetheless, we propose a way to estimate the power loss of a full-size module starting from results of accelerated PID tests on a mini-module manufactured with the same bill of materials.

In conclusion, recalling the experimental work presented in Chapter 4, we propose a new sequence of accelerated tests dedicated to PID to be performed in laboratory. By combining this test sequence with the simulations methodology presented in this chapter, a prediction of the effect of PID on a PV module will be obtained, as a function of the climatic conditions.

5.1 Introduction

This is the second chapter dedicated to the prediction of PID for modules in operation. In Chapter 4 we developed mathematical equations that describe PID as a function of stress factors when the stress conditions are kept constant in time (as it is the case during indoor accelerated testing). Here, we apply the equations to simulate the effect of PID on the power performance of a mini-module in operation in the field. For the sake of brevity we will sometimes refer to the device as “module” (such as in the flowcharts), however all the simulations are performed assuming a two-cell mini-module, of the same type as those subjected to accelerated aging testing in the laboratory in Chapter 4. Only the simulations of PID at the string level are performed for a commercial 60-cell module (Section 5.5.2). The software we use for the simulations is Matlab, version R2016b.

In order to evaluate the impact of the climate on PID, we perform simulations assuming that the two-cell mini-modules are operating in different climatic conditions. As reference locations we chose: Riyadh, Saudi Arabia, for a hot and dry, desert climate; Catania, Italy, for a hot Mediterranean climate; Miami, U.S.A., for a hot and humid, tropical climate; and Neuchâtel, Switzerland, for a temperate climate. As explained in the following sections, for each location we proceed according to the schema in Figure 5.1.

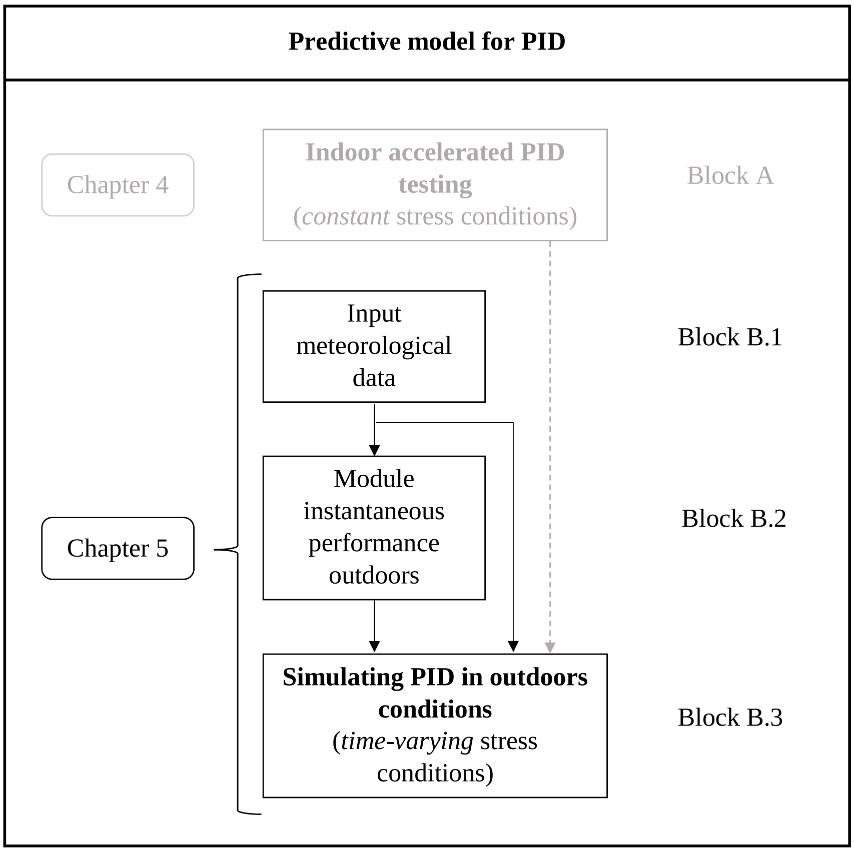

Figure 5.1: Building blocks of the PID model and outline of the chapter: the equations obtained in Chapter 4 (Block A) are applied here to simulate PID on modules in operation, and the parameter values for the PID equations extracted in Chapter 4 are used as inputs in our simulations (gray dashed line, Block A). First the module instantaneous nominal power is calculated (Block B.2), with meteorological data as inputs. The PID equations are then applied to the nominal power, with stress factors depending on the local meteorological parameters, and the impact of PID on module performance is simulated.

5.2 Calculating the module instantaneous nominal power

We first calculate the maximum power P_{max} that the module would have without any degradation. We refer to it as "nominal power", P_{nom}. This section corresponds to Block B.2 in Figure 5.1.

For these calculations we use the PV_LIB Toolbox for Matlab developed by Sandia National Laboratories. This toolbox is a set of functions to simulate the performance of PV systems. It allows us to simulate the module instantaneous nominal power (and electricity production) as a function of the (1) meteorological data of the selected site, (2) array characteristics (tilt, orientation), (3) mounting structure (ventilated *vs* non ventilated), and (4) module structure (number of cells, encapsulation scheme).

The nominal power varies at each instant according to the meteorological conditions. We employ Typical Meteorological Year (TMY) data, which are are commonly used in PV as they offer a representative picture of the local weather [154]. TMY data include such meteorological parameters as irradiance, ambient temperature, and relative humidity, with an hourly resolution. They are obtained by using time series of meteorological data and averaging them (long-term averages (LTA)). The higher the numbers of years used in building LTA, the higher the accuracy of the TMY data series. We obtained them from the software Meteonorm. The LTA are calculated over the period 2000–2009 for temperature, humidity, precipitation, and wind speed, and over the period 1986–2005 for radiation parameters. For locations in the U.S., TMY data are also available for free `http://rredc.nrel.gov/solar/old_data/nsrdb/1991-2005/tmy3/by_state_and_city.html#F`. Alternatively, TMY data, generally derived from satellite meteorological data, can be acquired for most locations on the globe. TMY are generally more accurate for some regions (*e.g.* Europe and North America) and less for others (*e.g.* Africa).

A flowchart of this algorithm is shown in Figure 5.3 (we denote this diagram by Block B.2). The inputs are constituted by the following sets of data.

- Geographical characteristics of the PV plant location, which include the Coordinated Universal Time (UTC) of the site, site latitude, site longitude, and site elevation.
- Properties of the array where the module is located in the PV plant, which include the azimuth of the module's array and the array tilt.
- Module specifications, which include:
  - Encapsulation scheme (glass/glass or glass/backsheet structure) and mounting configuration (open-rack, roof-mount or full-integration).
    We consider here a module with a glass/backsheet encapsulation scheme and that is open-rack mounted. These properties define the coefficients a and b to be used in King's equation for the module temperature (as we will show in Section 5.2.1).
  - Module electrical properties such as the temperature coefficients of the short-circuit current I$_{sc}$, of the open-circuit voltage V$_{oc}$, of the current at the maximum power point, I$_{mp}$, and of the voltage at the maximum power point V$_{mp}$.
    The values of these module parameters can be found for certain commercial module types in some databases included in PV_LIB, for example *SandiaModuleDatabase_20120925.xlsx*. As our simulations consider the two-cell mini-modules used in Chapter 4 for the indoor accelerated testing, we needed to determine the parameters for such specific devices. The parameters of the electrical performance at STC were obtained from our IV curve measurements (*e.g.* V_{oc}, V_{mpp}). The temperature coefficients of I_{sc} and V_{oc} were known from the cells' datasheet. Other parameters, such as those related to the spectral air mass influence, were taken from standard values for c-Si suggested in *SandiaModuleDatabase_20120925.xlsx* as default values.

- Temporal interval: the number N of years for which the simulation is run, using TMY data as the input meteorological data for each year.
- TMY meteorological data for the installation site in consideration, also shown in the diagram Block B.1a (Figure 5.2), inlcude:
    - The irradiance incident on the module surface, or plane-of-array (POA) irradiance, which is computed from the global horizontal irradiance (GHI), [W/m^2] and the diffuse horizontal irradiance (DHI), [W/m^2]. We assume no contribution from the ground reflected irradiance.
    - The module temperature, calculated from ambient temperature [°C] (generally at 2 m height), wind speed [m/s], dew point [°C], and atmospheric pressure [atm].

The dew point and the atmospheric pressure values are used to calculate the module temperature over the night. Details about calculating the module temperature (T_{mod}) are given in Section 5.2.1.

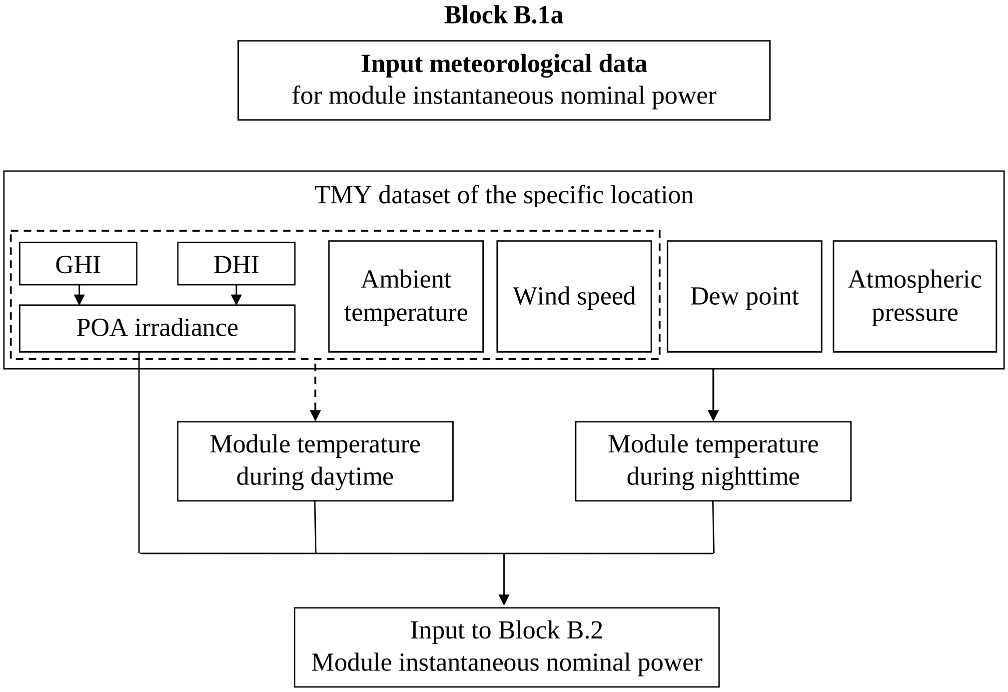

Figure 5.2: Block B.1a flow chart showing the meteorological data used as inputs to estimate the module instantaneous nominal power P_{nom} (see Block B.2 in Figure 5.3).

The module nominal power is then calculated with the above data as inputs (shown in Figure 5.3) and with a time resolution of 1 h. The output is thus a vector, P_{nom}, with a length corresponding to the number of hours over 25 years, *i.e.* $N := 25 \cdot 365 \cdot 24 = 219000$. The flowchart in Figure 5.3 illustrates in more detail the algorithm to calculate P_{nom} (Block B.2 in Figure 5.1).

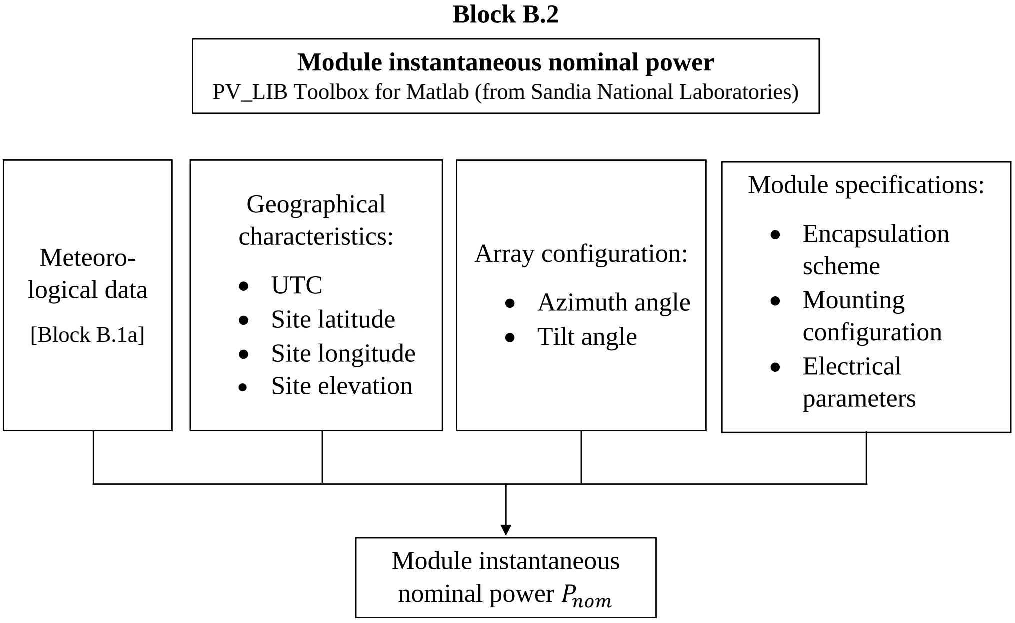

Figure 5.3: Block B.2 flowchart illustrating the calculation of the module instantaneous nominal power. The calculations are performed using the Matlab library PV_LIB, developed by Sandia National Laboratories.

5.2.1 The module temperature

A good estimation of the module temperature is essential to predict the occurrence of PID. Temperature is a stress factor for PID not only because it promotes the migration of sodium ions through the encapsulant (by reducing the resistivity of the encapsulant, as proven experimentally in Chapter 6) but also because it is linked to the formation of dew on the module surface.

In the absence of the film of water, when a strong negative field is present between the frame and the solar cell, the PID effect will generally affect only the cells (and the part of the cell) close to the module edge. Conversely, in general the presence of a thin film of water (dew or rain water) over a module's glass surface evenly distributes the potential from the grounded frame towards the center of the module, aggravating the PID effect. This was experimentally observed in [82], where for a one-cell mini-module installed outdoors sudden drops in the shunt resistance were observed that corresponded to periods when the surface conductivity, measured with a sensor, was higher (*i.e.* in the presence of dew or rain). The condensation of dew over the module surface will generally occur during the night, or, in sunny days, at dawn and during the evenings, when the module temperature cools below the dew point. During overcast days a layer of dew (or of rain) can be present as well during daytime. At night, this phenomenon is related as well to the sky temperature. On clear-sky nights, indeed, the sky temperature is generally lower than the earth (or module) temperature. The module (and earth) will then cool down by radiative heat transfer to the sky and its temperature will decrease below the air temperature [1], [64], [25].

A thin layer of water will be present on the module surface:

1. On clear-sky days: in the early and late hours of day when the temperature is below (equal to or just above) the dew point, as long as there is no direct sunshine light on the module surface, which will make the water immediately evaporate;
2. When it rains;
3. On cloudy or overcast days, the film of water formed by rain or by dew can remain for a much longer time over the module surface. We should stress that, during daytime and under this condition, the PV modules will be under tension (V_{mpp}), so that these are the conditions which will mostly trigger PID degradation.

In Section 5.3.1 we will introduce some thresholds on temperature that are used in the model to discriminate between a wet or dry surface. We continue instead this section presenting the models that we selected from the literature to obtain an accurate calculation of the module temperature at night and during the day. The calculated daily module temperature is then used as an input parameter to estimate the module instantaneous nominal power and to model the evolution of the PID effect.

King model

An empirical relation commonly used to compute the module temperature is that proposed by King in [86]:

$$T_{\mathrm{mod}}^{\mathrm{King}} = T_{\mathrm{air}} + \frac{E_{\mathrm{mod}}}{E_0} \cdot \exp\left(a + b \cdot v_w\right), \tag{5.1}$$

where:

$T_{\mathrm{mod}}^{\mathrm{King}}$ is the module temperature, estimated at the module back surface, [°C];

T_{air} is the ambient air temperature, [°C];

E_{mod} is the plane-of-array irradiance [W/m^2];

$E_0 = 1000$ W/m^2 is the reference solar irradiance on the module;

v_w is the wind speed measured at a height of 10 m, [m/s];

a, b are coefficients that depend on the mounting configuration and module type (refer to Table 1 in [86]). For a glass/backsheet module with an open-rack mounting configuration, as we consider here, $a = -3.56$ [-] and $b = -0.0750$ [-].

Although King's model gives a good estimation for the module temperature during the day under stable climatic conditions (*i.e.* not during transients), this relation might overestimate Tmod during nighttime by setting for $E_{\mathrm{mod}} = 0$, $T_{\mathrm{mod}} = T_{\mathrm{air}}$, which is however still a good approximation for cloudy/overcast nights. For this reason, we consider a second model for the module temperature at night: the Myers/Kempe model.

Myers/Kempe model

In this model, implemented by Kempe (NREL) in [73] using a physical model proposed by Myers in [108], the module temperature is the result of thermal exchange by solar radiation, convection, and thermal radiation to the sky, according to Equation 5.2. The Excel code that implements this model was shared by Mike Kempe for this work. More details about this model are given in reference [73].

$$T_{\mathrm{mod}}^{\mathrm{Kempe}} = \frac{\alpha E_{\mathrm{mod}} + 2T_{\mathrm{air}}h + \epsilon\sigma\left(T_{\mathrm{sky}}^4 + T_{\mathrm{Gr}}^4\right)}{2h + \epsilon\sigma T_{\mathrm{mod}}^3}, \tag{5.2}$$

where:

$\alpha = \epsilon = 0.6$ are, respectively, the module thermal emissivity and absorptivity, [-];

h is the convective heat-transfer coefficient, [-];

$\sigma = 5.6703 \cdot 10^{-}8$ W/(m^{2}K^4) is the Stefan-Boltzmann constant;

T_{sky} is the sky temperature, [°C], computed using the dew point and the atmospheric pressure. We point out that the implementation proposed by Kempe and used here always assumes clear-sky conditions. For more precise estimations, further parameters such as cloud cover factor should be integrated as well, which however are not included in typical meteorological datasets;

T_{Gr} is the ground temperature, assumed equal to T_{air}, [°C];

Comparison of models

In order to evaluate the King and Myers/Kempe models, we compare their outputs to module temperature data measured over five months on fielded modules in a PV plant in Greece, shared with us by a private company. The measurements were recorded on the rear side of the modules (with a glass/backsheet structure) with an hourly resolution over several months. We apply the two models using as inputs weather data collected for the same location and period from Solargis. Figure 5.4 shows the results over a restricted period of four days. The yellow line represents the plane-of-array irradiance. As we can see, the measured module temperature (black line) can indeed drop below the dew point (blue dashed line) during the night and early morning hours. The model by Myers/Kempe (green line) is better able to simulate the lower module temperature (compared to T_{air}) during these hours of the night/day than the model by King (red line), which sets instead the module temperature to the ambient temperature when the irradiance is null. The King model however still gives a better approximation for the daily module temperature when the sun shines.

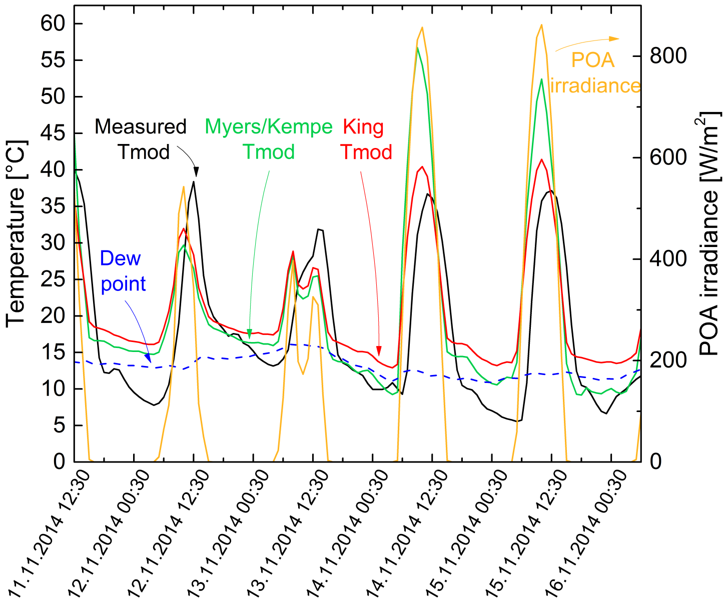

Figure 5.4: Measured temperature T_{mod} of a module installed in Greece (black line) compared to the outputs of the King model (red line) and the Myers/Kempe model (green line). During the night and the early morning hours (as distinguished by the yellow line of the POA irradiance on the right axis) the module temperature can drop below the dew point (blue dashed curve). The Myers/Kempe model gives a more realistic prediction of T_{mod} during such hours, while the King model is more accurate in the daylight hours when the sun shines.

For the same set of data, we then calculate the absolute error between each model and the measured temperature and plot it against the POA irradiance (Figure 5.5), confirming that the Myers/Kempe model is less accurate at high POA irradiance levels.

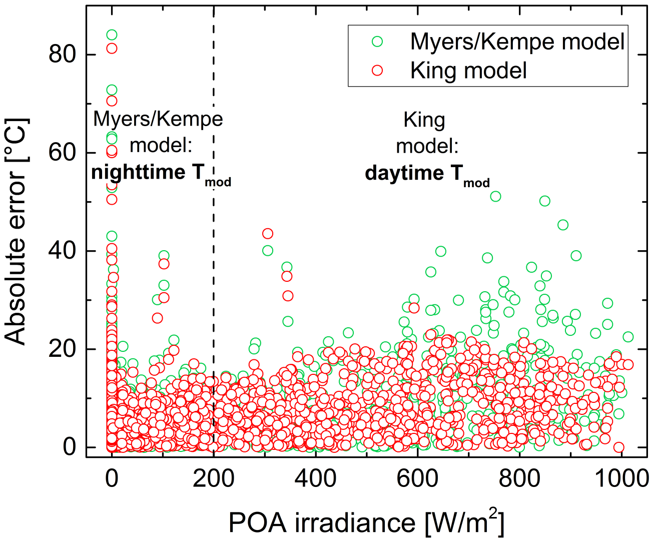

Figure 5.5: Absolute error with respect to the measured values of the two models used to estimate the module temperature $\mathrm{T_{mod}}$. The high errors at null irradiance correspond to some outliers in the measured values, probably due to sensor malfunctions.

Module temperature

Based on the above considerations, we calculate the module temperature at each hour *i* as follows:

- $T_{\mathrm{mod}}(i) = T_{\mathrm{mod}}^{\mathrm{Kempe}}(i)$ if $POA(i) < 200\ \mathrm{W/m^2}$;
- $T_{\mathrm{mod}}(i) = T_{\mathrm{mod}}^{\mathrm{King}}(i)$ otherwise.

5.3 Applying the PID model to field modules

Having calculated the mini-module nominal power, in this section we simulate the effect of PID, as a function of the meteorological conditions for the selected locations, on the mini-module performance if it were installed outdoors. This section corresponds to Block B.3 in Figure 5.1. To do this, we use the coefficients of the distinct aging contributions (*e.g.* temperature, relative humidity, time) as determined in Chapter 4 by means of indoor laboratory testing and specific to our devices.

As PID results from the interplay between power degradation and regeneration and is linked to the meteorological conditions in a complex way, we first define some thresholds on the weather data that allow us to distinguish the different phases in the PID mechanism (i.e degradation or regeneration).

5.3.1 Thresholds

PID at daytime *vs* nighttime

At night, when when there is no built-up voltage in the module, we assume that the module undergoes a temperature-dependent regeneration (this mechanism was analyzed in Chapter 4.2.2). Night is defined as any time interval in which module nominal power P_{nom} is zero.

Daytime: PID degradation *vs* regeneration

As we showed in Chapter 4, the module performance can undergo a certain extent of regeneration not only during the night, when there is no potential difference between the cells and the module frame, but also during the day, provided that specific weather conditions are met (typically, during hot and dry periods). During daytime, two phases of PID can thus occur: a degradation and a daytime regeneration. We model here the trade-off between degradation and regeneration by assuming an alternation between the two processes.

The surface conductivity of the glass is a key factor for PID, and it is increased by a high ambient relative humidity. The dependency of module power loss on the relative humidity was investigated through accelerated tests in Chapter 4. In Figure 4.6), the mini-modules power loss after 192 h was plotted against the RH level of the test and fitted with a polynomial curve. Such curve indicated that the value of $RH = 40\%$ seems to provide a threshold of humidity above which power degradation starts to be observed. In our simulations of outdoors PID we therefore assume that, during daily hours, power degradation occurs whenever the ambient relative humidity is $RH > 40\%$, otherwise daytime regeneration occurs.

Other authors apply different thresholds. In [44], for instance, degradation is applied when it rains or when the relative humidity is above 95%, otherwise regeneration is assumed (thermally-driven, with no voltage bias assumed).

Threshold on wet module surface

The dew point $\mathrm{T}_{D.P.}$ is defined as the air temperature, at a fixed vapor pressure p_{H_2O}, such that the saturation vapor pressure at $\mathrm{T}_{D.P.}$ equals the actual vapor pressure, *i.e.* $p^{sat}_{H_2O}(T_{\text{D.P.}}) = p_{H_2O}$ [123]. From the definitions of dew point and of relative humidity it follows that if, at a fixed pressure p_{H_2O}, the air temperature is lower than the dew point then RH> 100%, *i.e.* liquid water is also present in addition to saturated vapor (with formation of dew, or frost if the dew point is below the freezing point of water). As mentioned, we can thus assume that condensation occurs over the module surface when $T_{\text{mod}} < T_{\text{D.P.}}$. However, the transition phase between the condensed state and the dry state is typically not immediate, and a dew layer may remain over the module surface for a certain time after the module temperature has increased above the dew point, at least as long as there is no direct light impinging on the surface o f the module. This period can have a considerable extension, *e.g.* in cloudy and overcast days, or, for modules affected by shading, during the full year or during parts of the year (typically in winter) and for the early/late hours of the day.

Defining when the module surface is wet starting from weather data is therefore not straightforward. This aspect was investigated by Peter Hacke *et al.* in a paper of 2016 [34], where they analyze different indicators for the surface wetness of a c-Si module. One criterion that they identify is that the module surface is wet whenever the module temperature satisfies $T_{\mathrm{mod}} < T_{\mathrm{D.P.}} + 10°\mathrm{C}$.

Figure 5.6 shows time-lapse photographs we took on a commercial PV module installed in our outdoors testing facility in Neuchâtel, Switzerland, on 15/11/2017 during morning hours. In parallel, the ambient and module temperature, relative humidity and irradiance were monitored. The dew point was calculated from the ambient temperature and relative humidity, using Arden Buck equation to calculate the saturation vapor pressure (see Figure 5.7a). Before the sunrise the module was fully covered with frost (not dew in this case as it was a cold day), as shown in Figure 5.6 (a). The module temperature increases above the dew point at about 08:30 (see the zoom-in at the early morning hours in Figure 5.7b). However, the module surface does not immediately dry as one could expect. Instead, a phase change from frost to liquid state occurred starting 1h 34min later (see (b) and (c)), and the module surface was completely dry only at 10:02 (d). By comparing with the calculated dew point in Figure 5.7b, we see that a water film is present on the module surface until the module temperature is ~10°C to ~15°C above the dew point, consistent with what found by Hacke *et al.* [34].

Figure 5.6: Time-lapse photographs of a PV module installed in PV-Lab's outdoors facility in Neuchâtel. (a) The surface is initially covered by dew/frost, (b) and (c) a phase change from frost to liquid occurs starting from 09:34, and (d) at 10:02 the module is completely dry. The photos were taken by Jarle Austbø as part of his Master's project at PV-Lab [5].

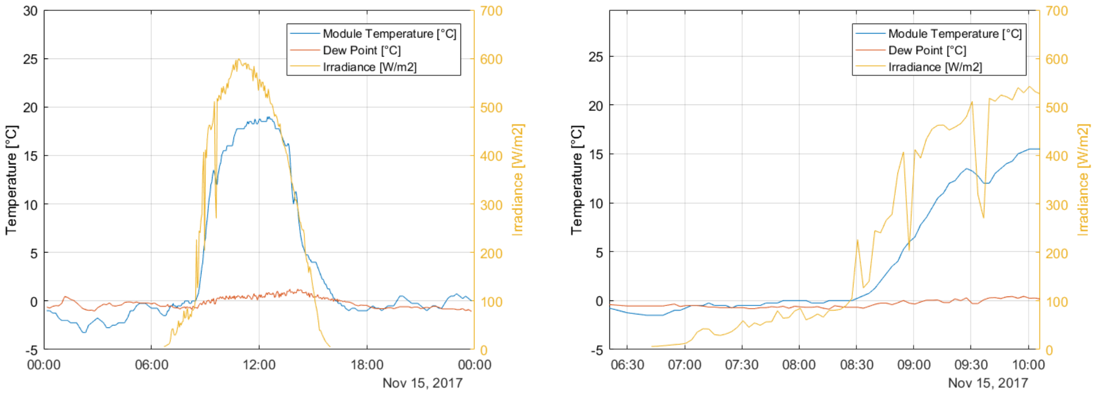

(a) (b)

Figure 5.7: (a) Irradiance and module temperature values over one winter day for the commercial module in Figure 5.6. (b) The first hours of the morning show the correspondence with the phase changes observed in Figure 5.6. The module temperature drops below the dew point over night, leading to the formation of frost (Figure 5.6 (a)); it then increases as the sun rises and at 10:00 its value is ~15°C above the dew point. Only at this time is the module surface completely dry (Figure 5.6 (d)).

This threshold does not consider the presence of direct sunlight, but it provides a reasonable assumption. We therefore adopt it in our model and assume in our simulations that condensation is present over the module surface, and set RH= 100% in Equation 4.3, if at least one of the following conditions is satisfied:

1. Rain;
2. $T_{\text{mod}} < T_{\text{D.P.}} + 10°\text{C}$.

These thresholds provide a more accurate description of the situation of a wet module surface than what we found in other works. In [82], for instance, the presence of dew is assumed for each hour of the morning and in general the module surface is assumed to be wet whenever the relative humidity exceeds 70%. The threshold in point 2, instead, is able to capture the transient dew behavior as the module temperature increases from its overnight condition.

The flowchart Block B.1b, in Figure 5.8, illustrates the meteorological data representing the stress factors for PID (both degradation and regeneration). Such data constitute some of the inputs in the final simulations for PID as shown in Block B.3 (Figure 5.9).

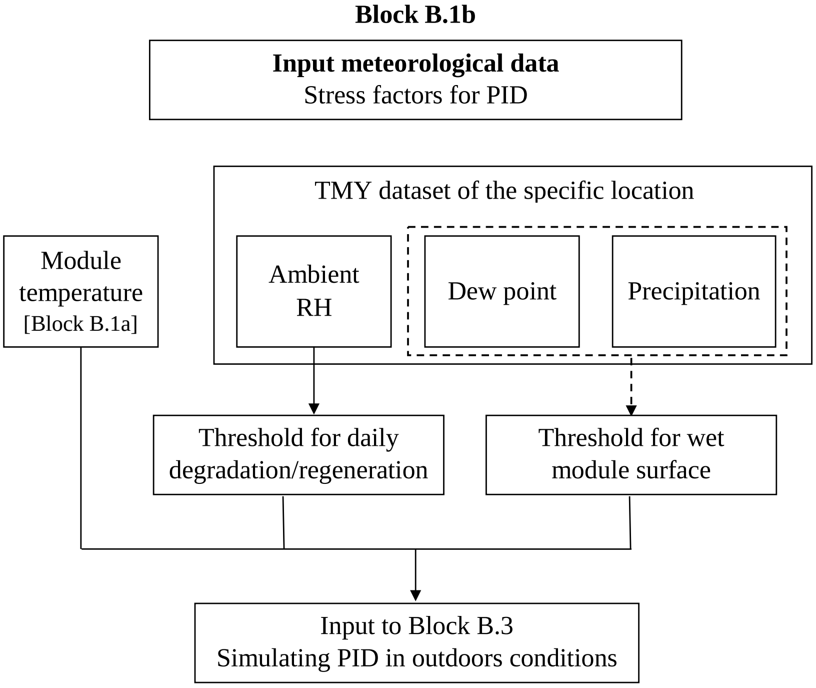

Figure 5.8: Block B.1b flow chart showing the meteorological data used as input stress factors in our simulations of PID for PV modules exposed outdoors (see Block B.3 in Figure 5.9).

5.3.2 Introduction to the PID simulations

We finally simulate PID for a two-cell mini-module, as those tested in Chapter 4, installed outdoors in the four different climatic locations selected. As a preliminary approximation we assume that the module is constantly exposed to a voltage of -1000 V during daytime. Later, in Section 5.5.2, we will simulate the performance of a string of several modules and the real instantaneous operating voltage of each module, V_{mpp}, will be used as PID stress factor.

The mini-module (sometimes we refer to it as "module", for the sake of brevity) is supposed to be mounted on a South/oriented and optimally tilted array for each location, with an open/rack mounting solution.

We now apply to the module nominal power the PID equations that we obtained empirically in Chapter 4 from indoors accelerated testing on our mini-modules:

- Equation (4.3) is applied during the daily degradation phase;
- Equation (4.8) is applied during the daytime regeneration phase;
- Equation (4.7) is applied for the nighttime regeneration.

The values of the parameters appearing in the above equations were determined from the accelerated tests matrices. Note that such values, resumed in Tables 4.2, 4.3, and 4.6, are specific of the materials and encapsulation configuration of the samples we tested (two-cell mini-modules, with a glass/backsheet encapsulation scheme and specific encapsulant and backsheet materials).

Using Equations (4.3), (4.7), and (4.8) to model PID in outdoors conditions is not straightforward. These empirical relations, and the corresponding parameters for our test devices were obtained from indoor laboratory testing. Modules were placed in climatic chambers and subjected to accelerated aging testing with specific stresses applied (*e.g.* temperature, RH, and voltage). We should stress, that during indoor testing the level of the stresses are kept constant throughout the whole duration of the test. Moreover, the value of the parameter we want to model (P_{max}) is described mathematically by a monotonously decreasing (or increasing) curve, starting at time $t = 0$ from a given nominal power (*i.e.* the module power at initial conditions, before the degradation). In contrast, when considering the performance of a module outdoors, there are two main differences with respect to indoor laboratory conditions, namely:

- The module nominal power (what corresponded to the initial point in the curve) is not fixed, but fluctuates continuously, depending on the instant irradiance, module temperature, and other environmental parameters (as discussed in Section 5.2).
- The stress levels that induce the PID (*e.g.* the temperature and the relative humidity, see Figure 5.8) also vary continuously in time.

The idea behind our approach consists in dividing a long temporal horizon (*i.e.* 25 years in our case, corresponding to the typical lifetime of a PV module) into smaller time intervals: 1 hour in our simulations. The advantage of this approach is that we can assume with a good approximation that in each one-hour interval the stress levels are constant. We can therefore model the degradation and the regeneration in each time interval using Equations (4.3), (4.7), and (4.8). A global simulation is then obtained by concatenating the local simulations with each other, using a mathematical method based on the concept of “equivalent time” (see Section 5.3.3).

The module power as consequence of PID is calculated with a time resolution of 1 hour and is thus a vector, P, of the same length as the nominal power vector, P_{nom}. This implies in particular that the time can be expressed in terms of (cumulative) hours. We thus define the time vector $t := (1, 2, ..., N)$, where N is the number of hours over 25 years as previously mentioned. In particular, the length of each time interval, $t(i) - t(i-1) = i - (i-1)$, is 1 hour and the general component $t(i)$ is the value of cumulative hours until time $t(i)$ and can be simply written as i.

Our model operates by applying the different equations and thresholds introduced earlier for the different parts of the day (night and day) and as a function of the input meteorological data. As already mentioned, we say that at time i it is nighttime if $P_{\mathrm{nom}}(i) = 0$ W. A simplified conceptual flowchart of the code used in Matlab is provided in Figure 5.9.

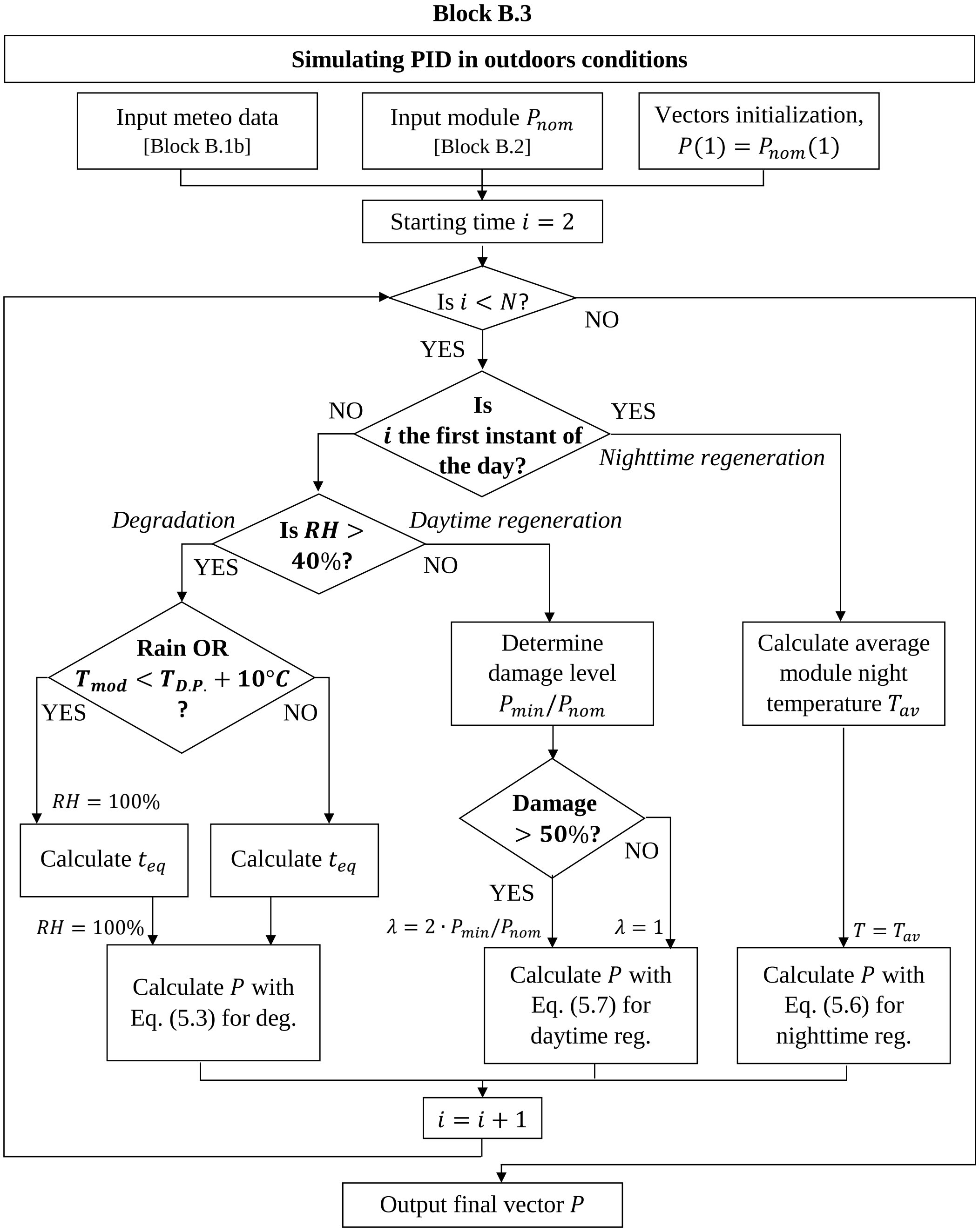

Figure 5.9: Flow chart for Block B.3 illustrating the code used to simulate the PID effect on modules in operation, using the meteorological data of the specific installation site and the PID equations and parameters derived in Chapter 4. Diamonds represent decision symbols, and the thresholds used in the PID model are highlighted in bold. In the first diamond, if $i < N$ and it is nighttime, then the algorithm sets $P(i) = P_{\text{nom}} = 0$ W and updates the index $i = i + 1$. If instead $i < N$ and it is daytime, the second decision diamond applies ("Is i the first instant of the day?") and the algorithm continues. Results of these simulations are shown in Figures 5.11 and 5.12.

5.3.3 Equivalent time

As mentioned, the concatenation of the local simulations with each other is realized by a method based on the idea of “equivalent time”, as follows. A similar approach has been previously applied by Braisaz in [15]. Here, we show in details how we use it and provide a mathematical proof of the consistency of such approach.

Consider two consecutive time intervals $[t_{i-2}, t_{i-1}]$ and $[t_{i-1}, t_i]$ and suppose the temperature is different in the two intervals, respectively T_{i-1} and T_i, with *e.g.* $T_{i-1} > T_i$. We want to model the power degradation over the two intervals. To simplify this example, let us suppose that the other stress parameters for power degradation (RH and V) are the same in the two time intervals. The power evolution is described in each interval by a continuous and monotonously decreasing function, P_{T_i} (corresponding to the power curve observed during indoor accelerated testing). At the end of the first interval the power has reached a a certain value $P_{T_{i-1}}(t_{i-1})$. In the next interval, the power degradation curve follows a different function, $P_{T_i}(t)$ (in blue in the plot). The equivalent time at time i, $t_{eq}(i)$, is defined as the time required at temperature T_i to reach the power value $P_{T_{i-1}}(t_{i-1})$, see Figure 5.10a. The two curves are then concatenated each other by considering as starting point in the curve $P_{T_i}(t)$ the value corresponding to $t_{eq}(i)$ (*i.e.* the curve $P_{T_i}(t)$ is shifted in the time-axis by $t_{eq}(i)$), see Figure 5.10b.

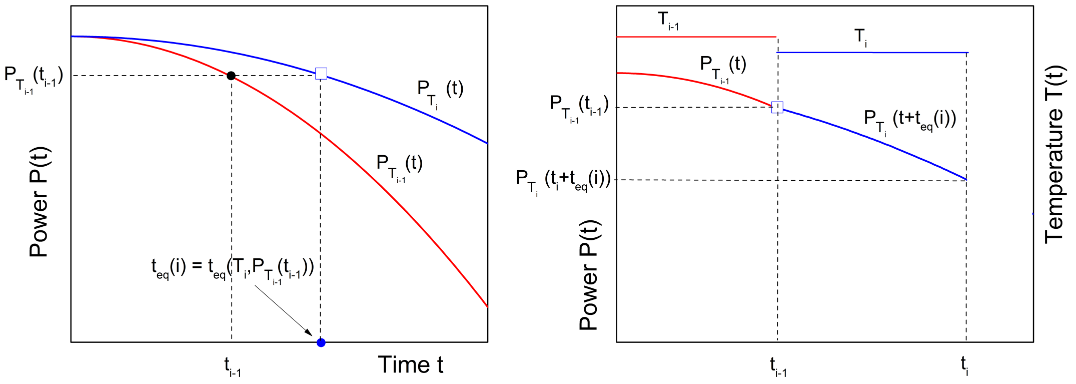

(a) (b)

Figure 5.10: (a): Schematic illustration of the definition of the equivalent time at time i, $t_{eq}(i)$. (b): Application of the equivalent time to concatenate two curves relative to two different temperatures, T_{i-1} and T_i.

In the case where the power function is given by the degradation equation found in Chapter 4

(Equation 5.3), it is possible to show that the equivalent time at time i is given by:

$$t_{eq}(i) = \sqrt{\frac{1 - \frac{P(i-1)}{P_{\text{nom}}(i-1)}}{A \cdot \exp\left(-\frac{E_a}{k \cdot T_{\text{mod}}(i)}\right) \cdot RH(i)^B}} \tag{5.3}$$

In Equation (5.3), k is the Boltzmann constant and A, E_a, and B are the parameters that appear in the equation for the power degradation found in Chapter 4 (Equation (4.3)).

This technique provides a "piece-wise" function that approximates the continuous one in that it tends to the continuous function for stress variations that tend to zero. Such method assures therefore a mathematically consistent implementation of an equation obtained at constant stress levels (Equation (4.3)) with time-varying stress levels as inputs. We provide a mathematical proof of this argument in Appendix A.

5.4 Bringing everything together: predicting PID in real outdoor conditions

Daytime

During daytime, when the module is exposed to a high negative voltage, the PID effect might take place. Depending on the ambient RH, either the module power degrades or it undergoes daytime regeneration.

- Degradation phase

  If $RH(i) > 40\%$ then we apply Equation (4.3) for power degradation, taking the instantaneous stresses, *i.e.* module temperature $T_{\text{mod}}(i)$ and air relative humidity $RH(i)$ values and supposing a constant voltage of -1000 V. The values of the parameters A, B and E_a appearing in the equation are those reported in Table 4.2.

  When it rains or $T_{\text{mod}} < T_{\text{D.P.}} + 10°\text{C}$ (*i.e.* the thresholds determined in Section 5.3.1 are satisfied) then the module surface is considered to be wet, and we set $RH = 100\%$ in Equations (4.3) and (5.3).

  Per each time interval $(i, i+1)$, the starting point on the degradation curve is calculated as the equivalent time $t_{eq}(i)$ using Equation 5.3.

- Daytime regeneration phase

  If $RH < 40\%$ we apply Equation 4.8 for daytime regeneration. As we found in Chapter 4, the maximum extent of power regeneration depends on the damage level $P_{\text{min}}/P_{\text{nom}}$ at the beginning of the regeneration period. Let us suppose that regeneration starts at time $\bar{i}$. We determine the power degradation level at time $\bar{i}$ and, for each $i > \bar{i}$ such that $RH(i) < 40\%$, we apply Equation 4.8, setting $\lambda = 1$ or $\lambda = 2 \cdot P_{\text{min}}/P_{\text{nom}} = 2 \cdot P(\bar{i})/P_{\text{nom}}(\bar{i})$ depending if $P(\bar{i})/P_{\text{nom}}(\bar{i})$ is, respectively, greater or lower than 50%.

In addition to the degradation level, there exists a second factor that can mitigate the capacity of the performance to fully regenerate and it is given by the number of "cycles" of PID. In [82], samples were successively degraded down to 40% of their initial shunt resistance R_{sh} and then left at null voltage for about 20 hours. It was observed that the maximum extent of R_{sh} regeneration decreases after each cycle, and that this was mainly due to a reduction in the slope of the R_{sh} regeneration curve. This dampening effect is not considered in the algorithm proposed here, as dedicated experimental tests would be required in order to quantify it. However, we suggest later a possible way to take this into account in our simulations, consisting in applying a dampening factor to the regeneration equations.

Nighttime

During the night, when no voltage affects the module, the module power regenerates. Regeneration at night is the result of a diffusion mechanism, therefore it is only driven by temperature. The model sets the instant module power to $P(i) = P_{\text{nom}}(i) = 0$ W. The power recovery is thus not directly translated into the instant module power but is rather reflected in the power value at the first instant of the next day. We say that time i is the first instant of a day if the module nominal power at time i is not null but P_{nom} at the previous time, $i-1$, is. For such i, the power $P(i)$ is calculated as a fraction of the nominal power $P_{\text{nom}}(i)$ that accounts for the level of degradation reached at the final instant (before night) of the previous day, and for the fraction of power regenerated over the night, according to Equation (4.7). The parameter $\tau(T)$ in Equation (4.7) is calculated at the average temperature during the night, $T = T_{av}$.

5.5 Results

After having run the algorithm explained above and represented in Figure 5.9, we obtain as output the vector of the module degraded power, that we denote by P. We then calculate at each hour i the normalized power $P(i)/P_{\text{nom}}(i)$.

5.5.1 Evolution of PID in different climatic conditions

The results of the simulations for the different climates are shown in Figure 5.11, where for the sake of clarity we plot the monthly average values of the normalized power vector P/P_{nom}.

As we can observe, the evolution of PID strongly depends on the weather conditions. In the hot and humid climate the module shows the maximum extent of power degradation. A certain extent of PID occurs in hot Mediterranean climates too, as indeed was extensively observed from field inspections in southern Europe [8]. In the desert climate the module power does not degrade at all thanks to the very low relative humidity (the yearly average in Riyadh is 26%).

Furthermore, the seasonal effect that was observed by some researchers in modules monitored outdoors is replicated by our simulations and reflects in the yearly cyclic behavior of the simulated power. To have a closer look on the effect of seasonality on power evolution, in Figure 5.12 we focus on the results for the first 3 years in Miami. The rainy season in Miami spans from May to September. This high humidity period corresponds well to the phase of power degradation obtained by our simulations. Afterward, the trend inverts and a regeneration phase occurs from October to April, months that correspond to the dry season in Miami.

We should mention that for Riyadh (and all other locations) we are not considering the effects of other contributions that could have a significant effect in triggering PID, such as the presence of soiling made of "conductive" particles, as the case of some typologies of sands (rich in metal-like particles) or of salt mist (close to coastal areas).

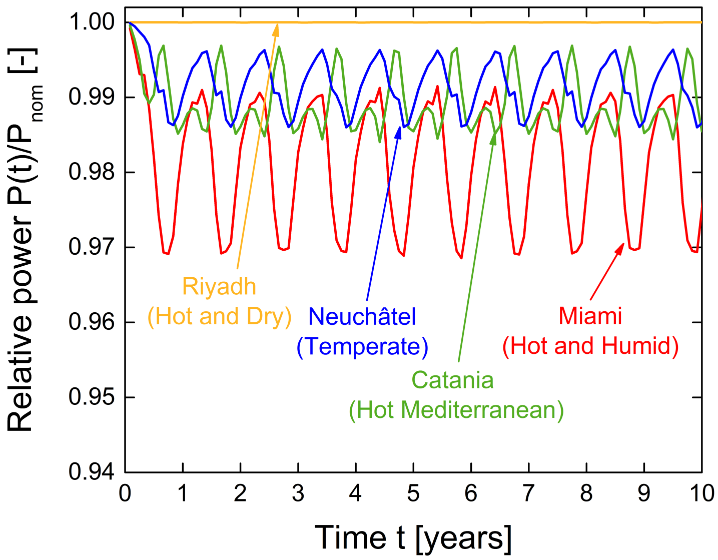

Figure 5.11: Time evolution of a c-Si two-cell mini-module power as consequence of PID for four locations representative of four different climates, as simulated with the algorithm shown in Figure 5.9. The values of the parameters for the power degradation and regeneration are those obtained experimentally for the same mini-modules in Chapter 4. The seasonal behavior that was observed *e.g.* in [36] is well reproduced. No dampening factor is considered thus the maximum level of recovery does not decrease in the long term and the time evolution repeats cyclically over the 25 years (here the first 10 years are shown).

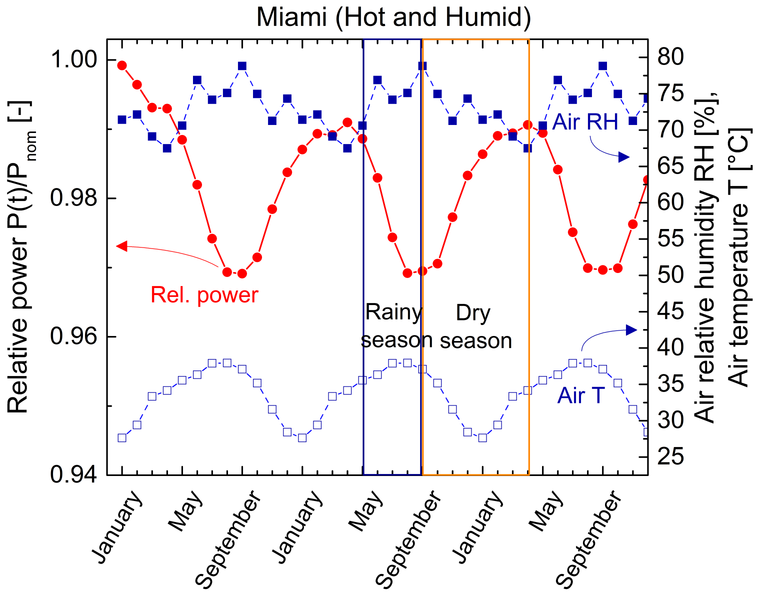

Figure 5.12: Focus on the first three years of Figure 5.11 for the climate of Miami. The power degradation occurs during the rainy season (May to September), also characterized by high temperatures (open squares) and higher humidity (solid squares).

In [36], Hacke *et al.* installed some modules all of the same type in Florida with -600 V applied during the hours of daylight, and they monitored their performance over 28 months. The results are shown in Figure 5.13 (adapted from [36] with the data generously shared for this work by Peter Hacke). A rapid degradation is observed during the hot and humid late summer months (from July to September), partially recovered subsequently during the winter months (the dry season in Florida typically spans from October to May).

Note that modules of the same type as those monitored in Florida were subjected in [36] to accelerated PID testing at standard conditions (60°C, 85% RH, -600 V) and showed a very pronounced degradation, with a power loss of 50% after less than 40 hours. Our samples, instead, degraded by only 1.5% after the accelerated test at 60°C, 85% RH, -1000 V. This difference in the performance during indoor accelerated testing is well reflected in our simulations, where our samples degrade by at most 3% (in the harshest climate of Miami), while a power loss of almost 50% was measured for the modules in Reference [36]. Our simulations indicate that a degradation of 1.5% after the standard PID test conditions assures a maximum power loss of only 3% even in the hot and humid climate. The power performance will therefore remain above the warranty limit of 80% after 25 years, if we consider PID to be the only degradation mechanism affecting the PV module. Results of the simulations are not shown over the 25 years in Figure 5.11 because the behavior repeats cyclically over the years.

A final comment on the results of our simulations in Figure 5.11 concerns the behavior of the power recovery, which cyclically reaches the same maximum level every year. As the module

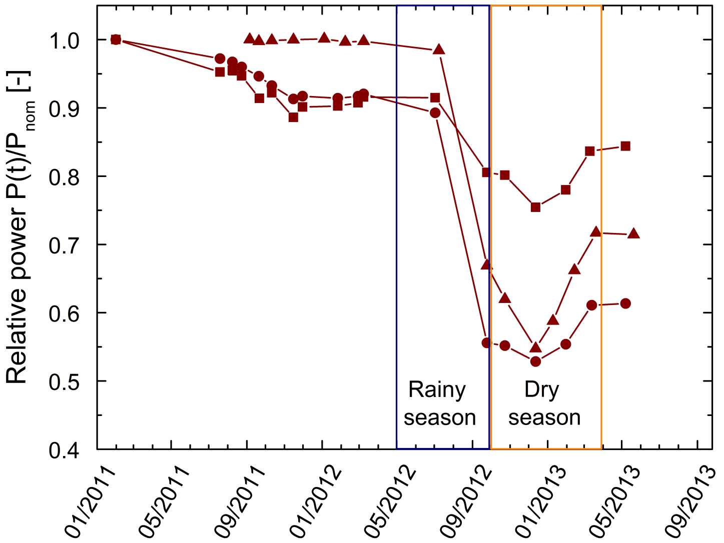

Figure 5.13: Power measured in [36] for c-Si modules installed in Florida with −600 V applied during the hours of daylight (figure adapted from [36]). The effect of seasonality is evident in the degradation and regeneration, especially in the second year of exposure. The much greater extent of power degradation of these modules compared to our mini-modules (Figure 5.12) is attributed to the very different susceptibility to PID of the two types of devices, which was observed during indoor accelerated testing.

power never decreases below 50%, our equation for daytime regeneration is always applied with $\lambda = 1$ and the effect of an incomplete recovery due to the damage level never applies (for these specific combinations of module PID parameters and climate conditions). The recovery being incomplete every year is thus exclusively attributed to the effect of the meteorological conditions.

As previously mentioned, we now show an example of the same simulation procedure where an additional dampening factor is applied to the equations for power regeneration, that accounts for the number of PID cycles (*e.g.* the number of days) experienced by the mini-modules. Figure 5.14 shows the simulated performance of our mini-modules in the climates of Neuchâtel and Miami where we apply dampening factors DF of hypothetical values of 1%/year and 5%/year as an illustrative example. The coefficient representing the dampening factor is included in parameter β in Equations (4.7) and (4.8), as we imagine that the quantity affected by the number of cycles will be the slope of the relative recovery function $RR(t)$ close to $t = 0$, which is mostly affected by the parameter β. This argument seems to provide more realistic performance simulations that predict a decreasing trend in the module power in the long-term. This point would require further investigation.

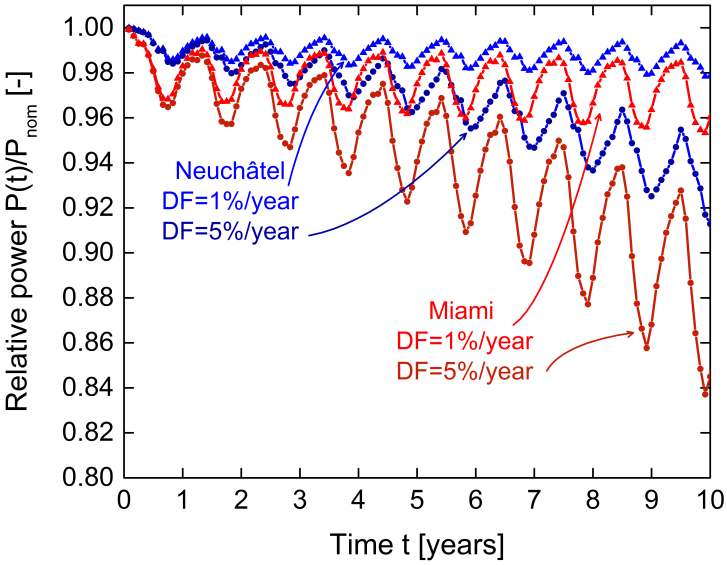

Figure 5.14: Simulated time evolution of a c-Si two-cell mini-module power as consequence of PID with a dampening factor (DF) applied to the regeneration equations, which accounts for the decreasing regeneration capacity of the performance as a consequence of the number of PID cycles. As an example we consider, for the climates of Neuchâtel and Miami, two hypothetical values of DF of 1%/year and 5%/year. However experimental work is required in order to correctly quantify the dampening effect.

5.5.2 Simulation of PID at the string level

The simulations presented above refer to a single module. As discussed in Chapter 3, the extent of PID depends on the position where the module is located in the string: as the modules are serially connected, the voltage that affects each of them depends on the voltages of the modules in the previous positions in the string. If m is the module position in the substring exposed to a negative voltage, the operating voltage of the module, at standard test conditions (STC), is $V_{\mathrm{mpp}}(m) = V_{\mathrm{mpp}} \cdot m$.

A second approximation we have done in the simulations for two-cell mini-modules is assuming that the module is constantly exposed to a negative voltage (-1000 V) during daytime. In fact, the operational voltage of a module varies in time depending on the meteorological conditions, particularly on the irradiance G and on the temperature T. We should stress that, because V_{oc} (and to a larger extent V_{mpp}) have a logarithmic dependence on the irradiance G ($V_{\mathrm{oc}} \sim \ln(G)$), a considerable voltage is applied to the internal module circuit even for low levels of irradiance. Therefore the PID phenomenon can progress even under these conditions.

In this section, we show an example of how our simulations can be applied to predict the performance of an entire string of commercial modules. The degradation of each module is taken into account as a function of its position in the string (thus, the voltage to which it is exposed) and exploiting the linear relationship between power loss and voltage found in

Section 4.1.6. We consider a string with the positive pole grounded and made of 34 serially connected modules with 60 cells. This example represents a realistic situation, as here the voltage that triggers the PID is actually given by the cumulative operating voltages of the modules in the string (up to ~-1000 V for the module at the extremity), rather than being artificially applied. The module electrical properties needed for the simulations are taken from the PV_LIB module database *SandiaModuleDatabase_20120925.xlsx*, where we select a standard 60-cells c-Si module with a V_{mpp} at STC of 29.52 V. As we do not have the parameters for the PID equations specific to such module type, we assume that the parameters of these modules have the same values as those of the two-cell mini-modules considered so far.

We then simulate the performance of the entire string of 34 modules in the climate of Miami. The algorithm used is analogous as that in Figure 5.9, but here the output is a matrix, with N lines (*i.e.* the number of hours in 25 years) and 34 columns. Each column $m = 1,\ldots,34$ is the vector representing the power output of the module in position m at each time instant i (also denoted by t_i). As mentioned, the PID is induced here at every time instant t_i for a module in position m by its actual operating voltage at that instant, *i.e.* $V_{\text{mpp}}(t_i)\cdot m$. In Figure 5.15 we show some results of power degradation of the string at two time instants (corresponding to two different seasons). The linear behavior obtained was also observed in some field inspections, such as shown in Figure 3.6 or reported in [8].

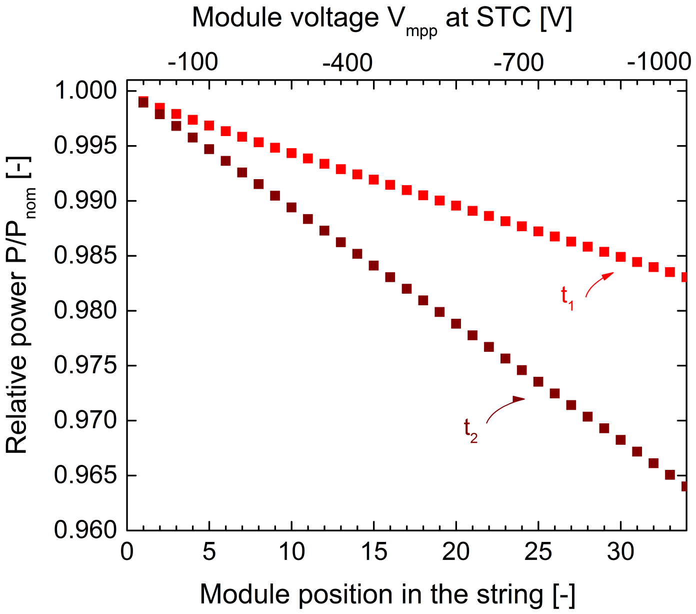

Figure 5.15: Simulated relative power of a string with positive pole grounded, installed in Miami. The string is assumed to be made of 34 commercial c-Si modules with 60-cells. As an example, the parameters of the PID equations for such module type are assumed to have the same values as those obtained for the two-cell mini-modules we subjected to the accelerated tests. The results are shown for two time instants t_1 and t_2, corresponding to two different phases in the seasonal PID evolution. The linear behavior reproduces what observed in some field inspections, such as shown in Figure 3.6 or in [8].

5.6 Test sequence for PID prediction

The aim of Chapter 4 was to extract a set of equations that allow to describe PID. Our experimental work and the simulations were performed on two-cell mini-modules. In general, however, our approach should be directly applicable on commercial modules, which would be subjected to the same matrix of accelerated tests performed in Chapter 4 and for which the set of parameters for the PID equations would be derived. Such parameters, specific to the module type under consideration, would then be used as inputs to simulate the PID effect on the given module type once installed in a specific climate.

The matrices highlighting the minimal set of tests required to characterize the devices, in order to simulate the evolution of PID as a function of specific climatic conditions, are shown in Table 5.1 and Table 5.2. Due to the variability in the PID susceptibility among modules, even if of the same model, each test condition should be ideally performed on *e.g.* 4 modules in order to obtain statistically representative results, even if testing such amount of modules might not always be possible due to costs constraints. We believe however that one module per conditions can potentially already provide the information needed for an estimation of the performance prediction. Such test sequence would require therefore the use of 12 modules.

The degradation tests we suggest last 192 h but an extended duration might be required for modules types in which the PID effect on the power appears later. For the regeneration tests, both in the dark and under irradiance, we provide indicative durations that should be sufficient to identify a trend in the power regeneration curve, however, the duration is likely to depend on the module type under consideration.

Table 5.1: Matrix of accelerated-aging tests proposed to model modules power degradation due to PID. For all conditions, a minimal duration of 192 h is recommended. Module performance characterization should be done initially, after 96 h, after 192 h (and further if applicable).

Degradation

T/RH	75%	85%	95%
60°C	−1000 V	−1000 V	−1000 V
85°C	/	−1000 V −500 V	/

In Chapter 3.3.3, we discussed the possibility that is available on the market to use “offset kits”, *i.e.* electrical devices that apply a high positive voltage to the modules during the night to regenerate their performance. Our predictive model does not consider this solution, since we were rather interested in modeling the natural evolution of PID on field modules. However, a possible way to simulate the performance of a module treated with this type of device is to perform the regeneration tests in the dark (in Table 5.2) with a high positive voltage applied to the modules (e.g. +1000 V) in place of keeping the modules in open-circuit conditions.

Table 5.2: Matrices of accelerated tests proposed to model power regeneration on modules pre-stressed in PID conditions at, *e.g.*, 85°C / 85% RH / −1000 V / 192 h. Modules characterization should be performed at the beginning of the regeneration test and throughout the test at intervals of ~100 h. On the left: For the tests in the dark, samples are left in open-circuit conditions with no voltage applied, for 1000 h (indicative duration). On the right: For the tests under irradiance and with bias voltage, a duration of 700 h is suggested for each condition (indicative duration). The different degradation levels suggested can be reached by performing the pre-degradation tests at different stress severities.

Nighttime (dark) regeneration
T [°C]
20
60
85

Daytime (light) regeneration			
T [°C]	Irradiance [W/m^2]	Voltage [V]	Degradation level $P_{\text{min}}/P_{\text{ini}}$ [%]
60	1000	−600	10
			30
			50
			70

5.7 Discussion and outlook

In this section, we comment on possible future improvements of our PID prediction model.

Model validation

In parallel with the development of the model we contacted several PV companies in order to collect field data that could be used to validate our simulations. Unfortunately, we encountered some difficulties: (i) companies are often reluctant in sharing their monitoring data due to confidential reasons; (ii) it is difficult to retrieve reliable field data (*e.g.* from regularly maintained irradiance and temperature sensors, time series with no gaps in data acquisition,...); (iii) in large plants, electricity production data are typically acquired at central inverter level thus including averages from several strings or subarrays. The performance of the single module (or string) is therefore difficult to assess and to compare to the simulated one.

We want to stress that so far none of the PID models presented in the literature have been validated against real field data. The only exception is the model by Taubitz that predicts the evolution of the module shunt resistance and has been compared to outdoor experiments with quite a good correlation [146]. However, the Taubitz model does not provide the impact on the real power degradation.

To have some preliminary and qualitative indications on the goodness of our model, we have referred to the data monitored in Florida in reference [36]. However, an appropriate validation of our model against real data is required. An extensive validation should comprehend:

1. performing the full matrix of accelerated tests (see Tables 5.1 and 5.2) on a set composed by a minimum number of 12 modules, thereby extracting the PID parameters specific to that module type;
2. installing some modules of the very same type and monitoring their performance over a minimum interval of 12 months. This should be carried out along with a reliable and accurate acquisition of the meteorological parameters (and of module temperature) at the installation site;
3. acquire meteorological data for the location under investigation not available from the measurements (*e.g.* precipitation data) and run the simulations according to the model/approach illustrated in this thesis and iteratively tune the parameters in the model (such as the damping factor).

An accurate way we foresee to achieve this goal is to perform this procedure on mini-modules (or large-area modules) manufactured in our laboratory with a known bill of materials. One option is to directly employ samples of the same type as the mini-modules considered so far in this work. If this was not feasible, for instance due to the relatively high resistance of our mini-modules against PID that might require long exposure times before detecting significant degradation, a second option is to perform the entire procedure on mini-modules manufactured with PID-prone materials (cells and encapsulant). This should allow one to detect, during outdoor operation, a significant effect of PID in a non-prohibitive time.

We also point out that a model validation was planned and has been attempted using two sets of reliable monitoring data, extending for over 3 years, from two large installations (one in Greece and one in Italy) severely affected by PID (courtesy of an independent power producer (IPP)). Unfortunately, it has not been possible to retrieve and subject to indoor accelerated testing the very same typologies of modules installed in the field. The set of modules delivered for indoor testing by the IPP (of the same brand, similar type, but very likely manufactured with a different bill of materials) has exhibited only a very moderate degradation under the harshest (95/85/-1000 V/192h) PID testing conditions. Therefore, it has not been possible to validate the model using these data sets and the modules delivered for the purpose.

Extending test results on mini-modules to full-size modules

Ideally, in order to extract the parameters needed to simulate the long-term performance of "full-size" (*i.e.* commercial modules with *e.g.* 60 cells) modules in a given climatic condition, the matrices of indoor tests proposed in Section 5.6 should be performed on the full-size modules. If this was not possible, for example due to space constraints in the climatic chamber, one option could be to test mini-modules (with *e.g.* 1 or 2 cells), manufactured with the same materials as the full-size modules.

An important remark is that the performance of mini-modules during PID accelerated tests is in general not the same as that of a 'full-size" module . In general, a full-size module will degrade less than a mini-module because the PID effect on each cell depends on the position of the cell within the module: the cells close to the perimeter experience a stronger electric field towards the glass, and a consequent stronger degradation, compared to the cells close to the center.

A way to extend the results of accelerated tests obtained on mini-modules to full-size modules includes simulating the distribution of the frame-to-cell voltage over the glass surface of the module. There exist methods to simulate the potential difference between a cell in a given position and the glass surface above the cell, proposed *e.g.* in [10] and [44]. Briefly, the module is represented as an electrical circuit, whose extremes are, respectively, the frame at 0 V and the cells circuit at negative potential towards ground (the applied voltage bias V_a, *e.g.* $V_a = -1000$ V), see Figure 5.16. The glass and the encapsulant are described as resistors against the leakage current flow: (i) an equivalent vertical resistor R_V is given by the vertical resistance of the glass and the vertical resistance of the encapsulant combined in series, and (ii) an equivalent lateral resistor R_L is given by the resistances in parallel of the glass surface (or if present, of the water film that covers it), of the glass, and of the encapsulant. By applying a simple voltage divider relation it is possible to calculate the voltage difference V between the glass surface and the cell as a function of the cell distance x to the frame:

$$V(x) = V_a \cdot \frac{R_V}{R_V + R_L(x)} \,. \tag{5.4}$$

In [10], voltage simulations based on this approach and using encapsulants with different volume resistivities were also validated experimentally.

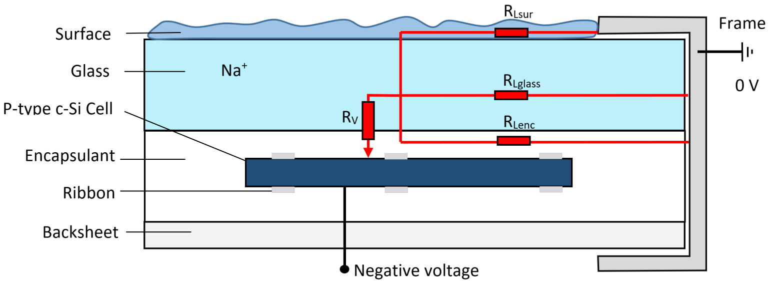

Figure 5.16: Schematic representation of a cross section of a module in PID conditions, with the possible paths for leakage current represented as resistors: a vertical resistor R_V and three parallel resistors: surface R_{Lsurf}, glass bulk R_{Lglass}, and encapsulant R_{Lenc}. Image reproduced from the Master thesis of Jarle Austbø at PV-Lab [5].

We propose now a method that leads from these simulations to finally estimating the power loss of the full module:

1. Simulate the voltage distribution over the one-cell mini-module surface using Equation 5.7 with the mini-module materials properties as inputs (sizes and resistivities).
2. Calculate an average voltage over the cell, $V_{\text{mini-mod}}$, by integrating the voltage curve over

the cell width and then multiplying the value by the cell width. As a first approximation, we consider a one-dimensional simulation over a vertical cross-section of the module along the shortest edge (supposing the longest infinite).

3. On the full-size module (suppose a 60-cell module), divide the cells into groups depending on their distance to the frame. In a 6x10 module, three groups would be identified: the cells on the perimeter, the central cells, and the intermediate ones.

4. For each group, consider a cell in that group (any cell equivalently) and calculate the average voltage over that cell as done for the one-cell mini-module.

5. Calculate the power loss of the cell by exploiting the linearity of the power loss on voltage found in Chapter 4: $\Delta P_i = V_i \cdot \Delta P_{\text{mini-mod}} / V_{\text{mini-mod}}$. The power loss of each single cell is now known.

6. Sum the power loss of each cell depending on the group it belongs to and divide by the number of cells to obtain an average power loss for the full module.

In Figure 5.17 we show an example. We suppose that the same materials as the two-cell mini-modules subjected to the accelerated testing are employed in a 60-cell module, and we use the results of the PID test at 85/85/-1000 V/96h for one of the mini-modules to estimate the power loss that the 60-cells module would experience if subjected at the same PID stress test. The resistivity properties of the encapsulant at 85/85 are derived from the measurements that we will describe in Chapter 6. The resistivity of the glass at 85°C was instead obtained by data provided by the manufacturer making some assumptions. With the aim of simulating the humid conditions on the module surface, we assume the presence of a water film on the glass, with a thicnkess of 5 μm, to provide a distributed grounding over the module surface, as it was done in [44]. However, the knowledge of the glass surface resistance as function of the relative humidity would be required.

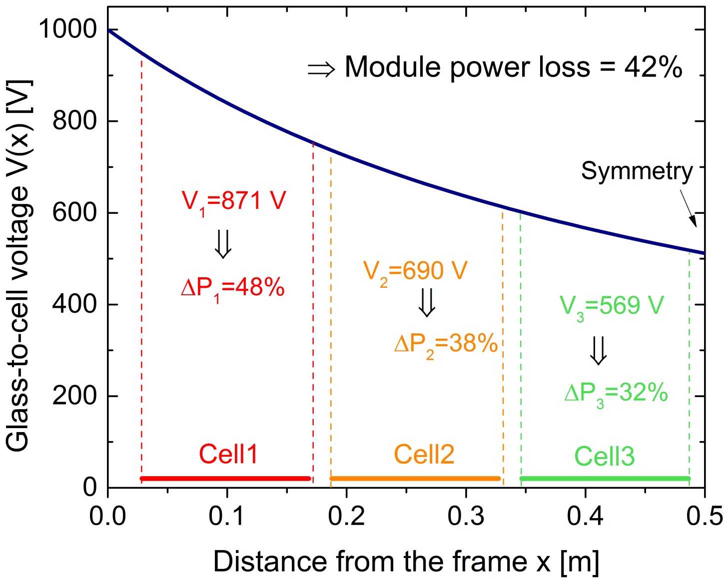

Figure 5.17: Local potential on the glass surface for a 60-cell module exposed to environmental conditions of 85°C/85%RH and with a bias voltage of -1000 V between the cells and the frame (grounded). Half module is considered out of symmetry. Cells are divided into 3 groups depending on their distance to the frame. The average voltage over each cell is used to calculate the power loss of the cell applying the linear relation found in Chapter 4. The two-cell mini-module showed a power loss of 50% after the same test conditions (results shown in Figure 4.8 in Chapter 4), which translates into a power loss of 42% for the 60-cell module.

By performing this procedure for each test condition in the matrix of degradation tests, the dependency of power loss on the stress factors (temperature, relative humidity, and time) could in principle be extracted and the parameters A, E_a, and B in Equation (4.3) for the full-size module calculated. We point out that same mathematical law that we found for our mini-modules also holds for full-size modules (a Peck model with a quadratic dependency on time). This was indeed the equation obtained by Hacke from tests on 60-cells modules, and was further confirmed by some tests we performed on commercial 60-cells modules (not shown in this thesis).

This method requires the knowledge of the volume resistivity of the encapsulant as function of the testing temperature (and relative humidity if the water diffusion into the module is also taken into account). As we will show in Chapter 6, we are able to perform such measurements on a given encapsulant. Modeling the effect of temperature and of relative humidity on the surface resistivity of the glass, instead, is an aspect that still requires further investigation. The daytime regeneration could then be treated in an analogous way, while the nighttime regeneration can be assumed to be independent on the module size as it is exclusively driven by temperature and not linked to the voltage.

Such an approach would provide a model for PID that takes into account intrinsic parameters of the module (resistivity of the encapsulant and the glass) and would thus constitute an interesting development for PID modeling, according to what pointed out in a report by the IEA of 2017 [52].

Finally, this method could find a more immediate but interesting application. Restricted to the standard PID test conditions (60°C, 85% RH, -1000 V), it would allow to estimate, starting from results on one-cell mini-modules, the power loss that a commercial module manufactured with the same materials would have if tested at the same conditions. The possibility to test mini-modules and extend the results to full-size modules would be strategic for manufacturers in the phase of identification of materials combinations that would result in a (commercially-labeled) PID-free module.

5.8 Conclusion

In this chapter, we attempt at simulating the evolution of PID for the very same devices that were subjected to indoor laboratory testing in Chapter 4, supposing that they are installed at a constant negative voltage (-1000 V) in sites representative of different climatic conditions. To do this, we employ the PID equations developed in Chapter 4 from indoors accelerated testing, together with the values of parameters extracted from the tests and which are characteristic of these devices.

The meteorological data we use as inputs in our simulations are typical meteorological year, TMY, data with hourly resolution. For a given climatic location, we first calculate the module nominal power P_{nom}, *i.e.* the maximum power the module would have if no degradation was present. We then simulate the PID effect on the module power at each hour by applying the equations derived in Chapter 4.

We set to 40% the relative humidity RH threshold above which degradation is assumed to prevail over daytime regeneration, based on the results of our degradation tests at different RH levels shown in Chapter 4.1.4. To estimate when the module surface is covered by dew, we exploit a relation, determined in [34], between the module temperature and the dew point. A feature of our model that is new respect to previous works is that it distinguishes when the module surface is dry or wet (dew or rain) based on an accurate threshold, the wet condition being particularly harsh because it makes the ground potential more uniformly distributed from the frame towards the center of the module.

We integrate for the first time in a PID prediction model a condition of wet module surface based on an accurate threshold that allows one to take into account not only rain hours but also the presence of a condensation layer. We find that a combination of King's model for daily hours (*i.e.* hours of sunshine) and of a model proposed by Myers/Kempe (for night or low-irradiance conditions) is more suitable than only the standard King's model, as it allows more accurate estimation of the module temperature especially during the hours when condensation typically occurs (even though the module temperature at night is still overestimated also by the Myers/Kempe's model).

The results of the simulations lead to the following main observations:

- The evolution of PID strongly depends on the weather conditions. In the hot and humid climate the module shows the maximum extent of power degradation. A certain extent of PID occurs in hot Mediterranean climates too, as was indeed extensively observed from field inspections in southern Europe. In the desert climate the module power does not degrade at all thanks to the very low relative humidity.
- The known effect of seasonality on PID is well reproduced by our simulations. For instance, in Miami degradation occurs in the hot and humid months, while a subsequent partial recovery takes place during the dry and cooler season. This trend is in agreement with the monitored performance of some modules installed in Florida PID stress conditions [36].
- The maximum extent of power loss in our samples modeled for the climate of Miami is 3%, much lower than the power loss of almost 50% of the modules exposed in Florida in [36]. This is consistent with the extremely different performance during indoor accelerated PID testing, where our samples degraded by only 1.5% after the standard test (96h) at 60°C, 85%, -1000 V while the modules in [36] lost 50% of their power after less than 40 hours at 60°C, 85% RH, -600 V.

We show, as an illustrative example, some simulations where a hypothetical dampening factor is applied that accounts for the number of PID cycles experienced by the mini-module. The resulting performance curve, though still reproducing the seasonal variations, shows a decreasing trend in the long-term, as it is probably a more realistic situation in the field, based on some recent results by [82]. Further experimental tests would however be required to assess the actual impact of the number of PID cycles on the regenerative capacity of the mini-modules and determine the value of such a dampening factor.

By exploiting the dependence of power loss on the voltage found in Chapter 4, we finally give an example of how our simulations can be applied to simulate the instantaneous performance of a string affected by PID constituted by any number of modules. Here the simulations realistically apply, at each time, the actual instant operating voltage V_{mpp} of the module as PID stress factor (such voltage being calculated for each module as function of its position in the string).

In conclusion, recalling the experimental work presented in Chapter 4, we propose a new sequence of accelerated tests to be performed in laboratory specifically dedicated to PID prediction. The general methodology we finally propose to achieve a prediction of the effect of PID on the electricity production of a PV module is: (i) subject a set of modules to the test sequence presented in Section 5.6, (ii) extract the values of the parameters of the PID equations, and (iii) perform the simulations described in this chapter with such parameters values as inputs, together with the set of meteorological data for the given location.

We conclude the chapter suggesting a possible procedure to estimate what the power performance of a full-size module would be after accelerated PID testing, starting from test results obtained on one-cell mini-modules. This method combines simulations of the voltage distribution over the module surface, as proposed by some authors, with the dependency of power loss on voltage that we established in Chapter 3.

Some points require further investigation. First, the simulations should be validated against data from the field. For example, mini-modules manufactured by us with a particularly PID-prone assembly could be tested according to the test matrices in Section 5.6 and in parallel a set of the same mini-modules could be installed and monitored outdoors. Second, additional experimental work could be foreseen to gain more insight on the daytime regeneration mechanism, especially on its dependence on temperature and voltage, its interplay with the mechanism of degradation, and its relationship with the number of PID "cycles".

If validated, this model could constitute a strategic tool for PV plants owners as it would allow the prediction of the long-term performance of a certain module type, thereby giving the possibility to select the appropriate type of module for a given location with respect to the possible occurrence of PID. For example, estimating the energy yield and the resulting levelized cost of electricity would allow to make a balance between the module cost and the actual risk of PID for the given module type for the specific PV plant location.

6 Preventing PID: the role of the Bill of Material

The factors leading to PID degradation are multiple and concern different aspects of a PV installation (electrical layout, mounting system,...), as described in Chapter 3. In this chapter, we concentrate on the module level, and investigate the relationship between PID and the bill of material (BOM), *i.e.* the list of materials, employed in the module. As in the rest of the thesis, we consider the mainstream technology of p-type c-Si solar cells.

We manufacture one-cell mini-modules using different combinations of the following materials: two different types of cell (PID-free cells and standard cells), two types of EVA materials (with, respectively, low and high electrical resistivity, ρ), and two types of backsheets (BS) with, respectively, low and high water breathability. We then compare their performance under accelerated PID testing. Some tests are performed at 60°C, 85% RH, conditions prescribed in the IEC TS 62804-1 [59] as the minimum severities to detect PID, and other tests are performed at 85°C when harsher degradation is sought or when samples are expected to be particularly PID-resistant. With reference to Table 1.2 in Chapter 1, the work presented in this chapter is an example of employing accelerated aging tests based on an international standard (or, in this case, technical specification) as *comparative* accelerated tests.

First, by testing samples laminated with the same (standard, polymer-based) backsheet, we observe that to have a "PID-free" module the combination of PID-free cells and an EVA encapsulant with high electric resistivity is the most recommendable choice. The choice of the encapsulant plays a very important role in contrasting the PID effect. For example, with the materials we tested, combining a PID-free cell with a low resistivity EVA proves less effective than using a standard cell with a high resistivity EVA.

We measure the electrical resistivity of the two encapsulant films at different temperatures and relative humidity levels. As ρ is reduced by increased water concentration in the film, we are initially surprised to observe that the breathability properties of the backsheet have apparently no influence on PID degradation. An observation that we are later able to explain by running some simulations of water diffusion in the encapsulant for different sandwich structures.

We then run a second set of experiments on some encapsulation schemes with an improved resistance to water ingress (*i.e.* glass and backsheet with barrier layers as rear covers and an edge sealant). Results show that, in fact, preventing or reducing the diffusion of moisture in the front encapsulant layer also contributes to further mitigate the impact of PID.

Finally, we observe that, for the cell type used in our tests, *i.e.* p-type c-Si with an aluminum back surface field (Al-BSF), having a glass layer at the rear of the cell does not add to the PID effect compared to having a rear sheet as well impermeable but not containing Na (*i.e.* the BS with Al layer). On the contrary, our tests indicate that a glass/glass construction is more PID-resistant than a glass/backsheet one, result that we attribute to the higher barrier against water diffusion provided by the double glass configuration and the consequent higher encapsulant resistivity as shown by our simulations.

The findings obtained in this chapter are the subject of a paper that has been submitted to *Progress in Photovoltaics*, see [152].

6.1 Introduction

When coming to module assembly, several strategies related to the choice of the materials are offered to manufacturers, and their customers, to suppress or minimize the negative impact of PID on framed modules. In particular, the use of:

i Specific PID-free cells. As discussed in Chapter 3.2.4, one strategy to suppress PID is to deposit dielectric anti-reflective coatings (ARC) with increased conductivity on the solar cells, in a way that the electric field in the SiN_x responsible for the drift of Na ions towards the bulk silicon is reduced (see [112] and [114]). However, a trade-off exists between cell efficiency and PID sensitivity when modifying the composition of this layer. Other strategies at the cell level focus on increased doping profiles, surface treatments (such as growing an intermediate SiO2 layer between the Si and the AR coating) or ion implantation in the cell's emitter [14], [41].

ii Encapsulating polymers with higher electrical resistivity (ρ) to prevent the diffusion of alkali metal ions from the glass cover into the cell. Several materials such as thermoplastic polyolefin (TPO), ionomer or high-quality EVA have been shown to prevent or strongly moderate the occurrence of PID [70], [9], [14], [2].

iii Special cover glasses with increased resistivity, such as glass with reduced Na content or quartz glass [33], or different processing, such as chemically strengthened glasses [14], [69].

However, the efficacy and the cost-effectiveness of the single strategies (or their combination) is frequently unknown. Here, we investigate how PID degradation of encapsulated (and framed) solar cells is affected by the choice of the solar cell and of the encapsulating polymer.

In view of the industrial application of the results and considering the constant market pressure to significantly reduce module-manufacturing costs, we focus on what we believe to be the most cost-effective solutions only, and do not investigate for example the use of special cover glasses. For the same reason, as EVA is currently used in > 90% of the modules manufactured today, we focus on this encapsulant only.

As the properties of the backsheet (BS) may have a strong impact on the physical properties of the encapsulant material (water content and resistivity), in our study we consider as well backsheets with different breathability properties, *i.e.* with different Water Vapor Transmission Rates (WVTR). To interpret some of the experimental results, we then run a second set of experiments, and in parallel perform some simulations, focused at investigating the influence on PID degradation of moisture ingress in the module sandwich.

6.2 Experimental work and modeling

6.2.1 Influence of solar cell, encapsulant, and backsheet properties on PID

The materials we use for assembling our test devices are all commercially available. These include two types of c-Si solar cells (conventional *vs* PID-free c-Si solar cells, both p-type), two types of EVA films from the same supplier with, respectively, low and high electrical resistivity, and two types of backsheets (BS) from the same supplier with, respectively, low and high breathability, *i.e.* BS with different Water Vapor Transmission Rates (WVTRs). We then investigate all possible combinations (*i.e.* $2^3 = 8$) of this bill of material (BOM) list and assemble our one-cell mini-modules according to the matrix shown in Table 6.1, by means of a conventional lamination process. In order to simulate the presence of a frame, the edges of the mini-modules are covered with a conductive aluminum (Al) tape.

Additionally, we measure the volume resistivity of our encapsulants as a function of humidity and temperature. Before each measurements, the cured samples were pre-conditioned in a climatic chamber. Measurements are performed according to the IEC 62788-1-2 standard (Method B) [58] using a Keithley electrometer and a 8009 resistivity test fixture.

Table 6.1: Overview of the different materials (cells, encapsulants, backsheets) used in the first part our study.

Bill of Material	* from datasheet	
Cells	Standard c-Si (std-cell)	PID-free cell (PID-free)
Encapsulants	EVA high resistivity (EVA-high-ρ) $^*\rho > 1 \cdot 10^{15}\ \Omega \cdot \mathrm{cm}$	EVA low resistivity (EVA-low-ρ) $^*\rho > 6 \cdot 10^{14}\ \Omega \cdot \mathrm{cm}$
Backsheets	BS high WVTR (BS-high-B) *WVTR ~ 1.8 $\mathrm{g/m^2/d}$	BS low WVTR (BS-low-B) *WVTR ~ 0.7 $\mathrm{g/m^2/d}$

In a second set of experiments, we further investigate the role of the backsheet and of encapsulation schemes with improved resistance against water ingress. To do this, we manufacture mini-modules using conventional (std-cell) cells only and EVA with high volume resistivity (EVA-high-ρ) and make use of structures with increased resistance properties to water ingress: (1) glass/glass (G/G), and (2) glass/glass with edge sealant (G/G-seal). The rear glass and the edge sealant are used to prevent moisture ingress in the module sandwich. In order to verify that the rear cover glass is not contributing in worsening the PID effect, we manufacture an additional sample (3) using a fully impermeable backsheet that includes a laminated Al foil barrier (G/BS-bar). All samples use a solar-grade front cover glass. An overview of the rear covers used in this study is given in Table 6.2.

Table 6.2: Overview of the rear covers used in this study. All modules use a solar-grade front cover glass sheet. Values from datasheet.

Rear cover	WVTR (g/m2/d)	Edge sealant	Acronym
BS with high breathability	~ 1.8	No	BS-high-B
BS with low breathability	~ 0.7	No	BS-low-B
BS with Al foil barrier (no breathability)	$\leq 5 \cdot 10^{-3}$	No	BS-bar
Glass (no breathability)	0	No	G/G
Glass with edge sealant (no breathability)	0	Yes	G/G-seal

6.2.2 PID stress tests

The samples are subjected to a PID stress test as prescribed by the relevant IEC Technical Specification for c-Si modules (IEC TS 62804-1:2015 [59]), using a climatic chamber (see Chapter 2.5). Besides the conventional stress level (*i.e.* 60°C, 85% RH, -1000 V, or 60/85), we increase in a set of samples the stress level to 85°C, 85% RH (85/85) to accelerate the degradation. The test is run beyond the conventional 96 h up to 192 h, and for a much longer time in the second round of experiments. Before and after the degradation, the modules are characterized by means of IV measurements at standard test conditions and EL imaging.

6.2.3 Modeling water ingress in the sandwich structure

To interpret some experimental findings and investigate further the role of the backsheet and of water ingress on the evolution of PID, we finally run some simulations of moisture diffusion in the sandwhich structure using the two different configurations shown in Figure 6.1 (b): a glass/backsheet structure and a glass/glass one.

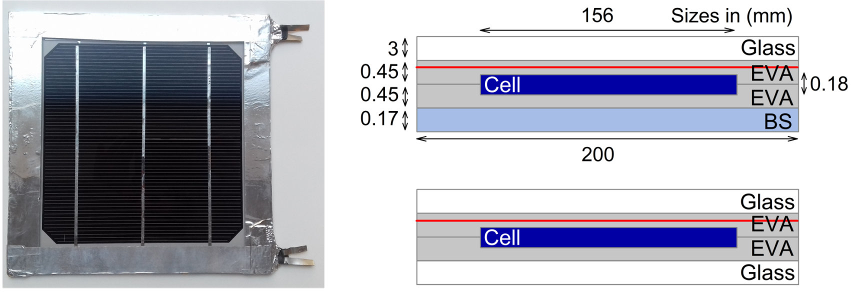

(a) (b)

Figure 6.1: (a) Top view of the one-cell mini-modules used in this work, with an Al tape applied to the edges simulating the presence of a frame. (b) Cross-sections of the two encapsulation configurations considered for simulating the water diffusion into the sandwich. Top: 2D geometry employed in the FEM simulations for the G/BS construction. Bottom: G/G structure. In this last case, a simple 2D geometry of 200×200 mm^2 given by the only encapsulant is in fact considered in the simulations, thanks to vertical symmetry (impermeable front and rear cover).

The general procedure that we employ to determine the diffusivity properties of the materials and to perform the simulations was described in Chapter 2.4.

In a G/G sample, water is able to penetrate from the open sides of the encapsulant. We solve the diffusion equation in a 2D domain of length L_x and width L_y equal to 0.2 m (the size of a one-cell mini-module) using Fourier series (Equation (6.1)) an approach previously used by authors in [74] and [63]. The resulting value is the water concentration c in a certain point (x, y) of the domain at time t. In the equation, c_{init} and c_{surf} are, respectively, the initial and the surface concentration of the encapsulant, and D its diffusion coefficient.

$$\begin{aligned} c(x,y,t) = c_{surf} + \left(c_{init} - c_{surf}\right) \cdot \frac{16}{\pi^2} \cdot \sum_{n=0}^{\infty} \frac{1}{2n+1} \sin\left(\frac{(2n+1)\pi x}{L_x}\right) \exp\left(-\frac{(2n+1)^2 \pi^2}{L_x^2} D t\right) \cdot \\ \cdot \sum_{m=0}^{\infty} \frac{1}{2m+1} \sin\left(-\frac{(2m+1)\pi y}{L_y}\right) \exp\left(-\frac{(2m+1)^2 \pi^2}{L_y^2} D t\right) \end{aligned} \tag{6.1}$$

The relative humidity (%) in the encapsulant is finally calculated as the relative saturation (Equation (6.2)), as also done in [19]. The saturation concentration, c_{sat}, is the product of the EVA solubility and the water vapor partial pressure in the air at the testing conditions, according to Henry's law.

$$RH(x,y,t) = \frac{c(x,y,t)}{c_{sat}} \cdot 100 \tag{6.2}$$

With respect to the G/BS configuration, the lack of vertical symmetry and the fact that we are interested in the RH in the front encapsulant make it necessary to employ Finite Elements Method (FEM) simulations. An analytical 1D equation like the one proposed in [73] would, indeed, not be applicable here as it is rather suitable to estimate the RH in the encapsulant below the cell. The FEM simulation are run with the software Comsol Multiphysics (version 4.4), with a 2D geometry as depicted in Figure 6.1 (b) at the top.

6.3 Results

6.3.1 Resistivity measurements

Figure 6.2 shows the volume resistivity measurements performed on the EVA-high-ρ and EVA-low-ρ encapsulants as a function of relative humidity. At room temperature (25°C) and RH 40% the two encapsulants have a measured volume resistivity of $5 \cdot 10^{15}\Omega\cdot$ cm and $8.5 \cdot 10^{14}\Omega\cdot$ cm respectively, slightly higher than datasheet values. The volume resistivity is moderately reduced by increasing humidity. The effect of temperature on ρ is much more pronounced than that of humidity, with ρ decreasing by approximately one order of magnitude over a 30°C interval (see Figure 6.2). A similar behavior has been observed in other works (see *e.g.* [131] and [9]).

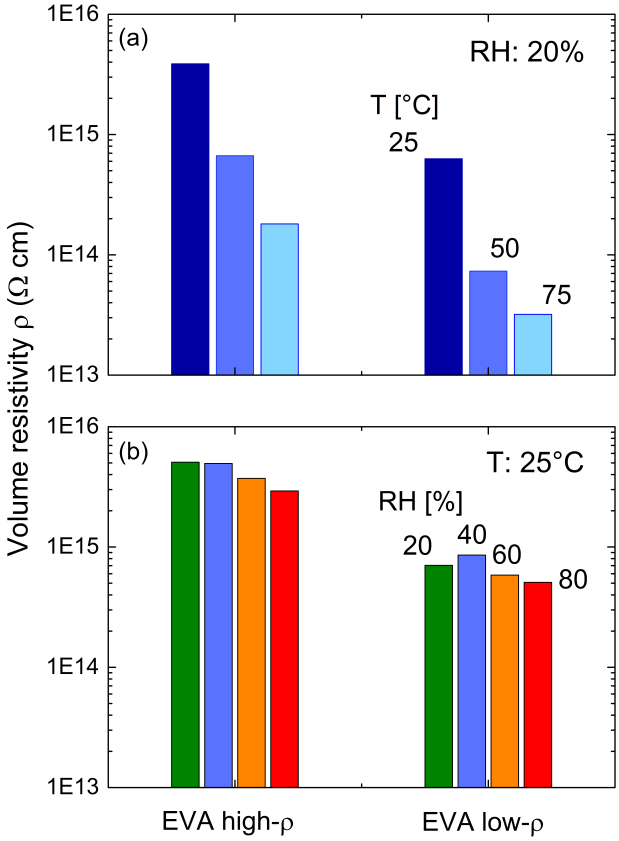

Figure 6.2: Volume resistivity for the EVA-high-ρ and EVA-low-ρ encapsulants as a function of (a) temperature at fixed RH (20%), and (b) of relative humidity at fixed temperature (25°C).

6.3.2 PID testing at 60°C / 85% RH

Table 6.3 shows the extent of power degradation of our samples after PID testing at 60°C / 85% RH. For standard cells, the choice of the EVA polymer has a drastic impact on PID degradation. Whereas the cells processed with a low resistivity polymer show a huge degradation ($\sim -80\%$ after 96 and 192 h), those processed with high-ρ EVA show nearly no degradation. This is true irrespective of the BS used in sample processing. Conversely, for the PID-free cells, the choice of the EVA, as well as of the BS, at 60°C / 85% RH seems negligible, and for all the possible combinations of materials, the degradation after 96 and 192 h is limited to $\leq 1\%$.

Table 6.3: Power degradation of the different test samples after 92 and 192 h of PID testing (60 °C, 85% RH, −1 kV).

Cells	EVA	BS-high-B (96 / 192 h) [%]	BS-low-B (96 / 192 h) [%]
Std cells	High ρ	−0.7 / −0.1	−0.8 / −0.4
	Low ρ	−85 / −83.5	−77.9 / −76
PID-free cells	High ρ	−2.7 / 0	−0.3 / 0
	Low ρ	−0.7 / −1	−1.7 / −1

6.3.3 PID testing at 85°C / 85% RH

The picture changes when applying more severe test conditions (85°C / 85% RH) and accelerating the degradation. In Figures 6.3 (a) and (b) and Table 6.4, we show the results of extended 85/85 PID testing on our samples manufactured, respectively, with standard and PID-free c-Si cells.

For standard c-Si cells, the choice of the EVA polymer has a drastic impact on PID degradation. Whereas the cells encapsulated with a low resistivity polymer show a huge degradation (∼ −90% after 96 h), the ones processed with high-ρ EVA degrade by only −6.9% and −11.7% after, respectively, 96 and 192 h (for the BS-high-B samples). Surprisingly, in the extended testing (85/85) too, the effect of using BS with different WVTRs is nearly negligible. This aspect will be further investigated in Section 6.3.4.

Table 6.4: Power degradation of the different test samples after 92 and 192 h of PID testing (85 °C, 85% RH, −1 kV).

Cells	EVA	BS-high-B (96 / 192 h) [%]	BS-low-B (96 / 192 h) [%]
Std cells	High ρ	−6.9 / −11.7	−9.2 / −10.9
	Low ρ	−89.1 / −88.2	−96.6 / −96
PID-free cells	High ρ	−1.6 / 1.3	−1.8 / −1.2
	Low ρ	−12.1 / −18.1	−11.7 / −15.4

For the PID-free cells (see Figure 6.3 (b)), the choice of the EVA polymer still has a significant impact on PID degradation. Whereas the cells encapsulated with a high resistivity polymer show nearly no degradation (∼ −1.5% after 96 and 192 h), the ones with low-ρ EVA degrade by −12.1% and −18.1% after, respectively, 96 and 192 h (for the BS-high-B samples). It is remarkable to observe that this degradation is larger than that experienced by the conventional c-Si cells encapsulated with the high-ρ EVA polymer. For this set of samples too, the progression of PID degradation is not affected by the breathability properties of the BS (see as well Section 6.3.4).

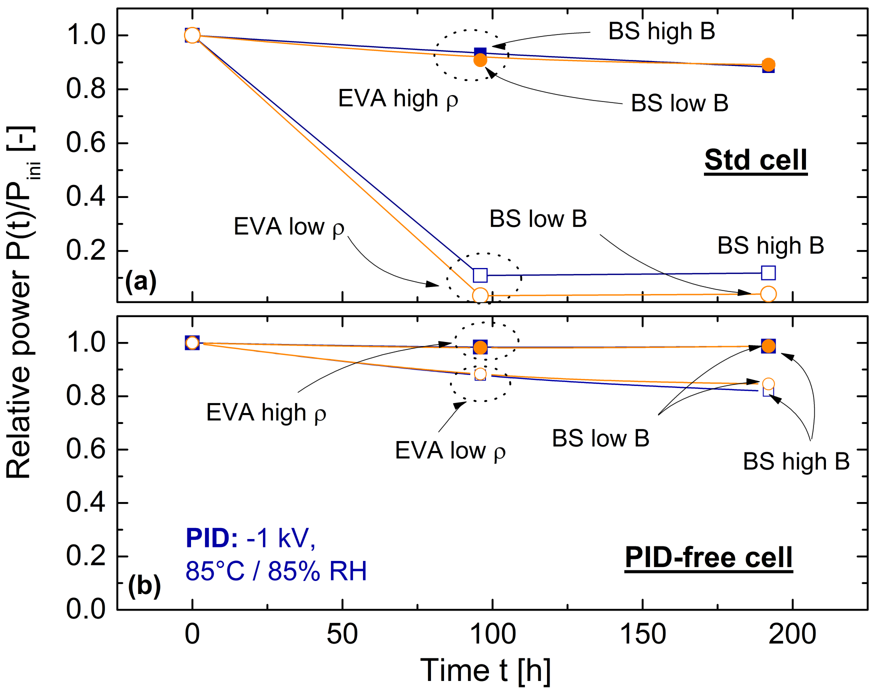

Figure 6.3: Degradation after PID test (85°C/ 85% RH, -1 kV) of (a) standard (std) c-Si solar cells, and (b) PID-free solar cells. For both set of samples, two different EVA encapsulants with respectively a low and high resistivity ρ, and two types of backsheets (BS), with a high and low breathability (B), are used.

As the choice of the BS has apparently a negligible effect on PID degradation, to summarize we bring together in Figure 6.4, for the BS-low-B samples only, the results obtained for the samples with the conventional cell using high-ρ EVA and for those including a PID-free cell (with high-ρ and low-ρ EVA).

The results of extended testing at 85/85 conditions indicate that the use of PID-free cells is by far the best option to prevent the occurrence of PID, but only if the sandwich is laminated with a highly resistive EVA polymer.

The use of a standard cell in combination with a high-resistivity EVA encapsulant still needs to be favored to the use of PID-free cells in combination with a low-quality EVA encapsulant.

Nevertheless, note that these results were obtained on one-cell mini-modules, so that, by considering the evolution of the PID phenomenon from the module edges (as is frequently reported for the different climatic conditions), they should represent a sort of worst-case situation, exhibiting a particularly pronounced degradation. The application of these results to 60- or 72-cell large-area modules is not straightforward, nevertheless the results give already a clear indication on the possibilities that are offered to mitigate the PID phenomenon at the module level.

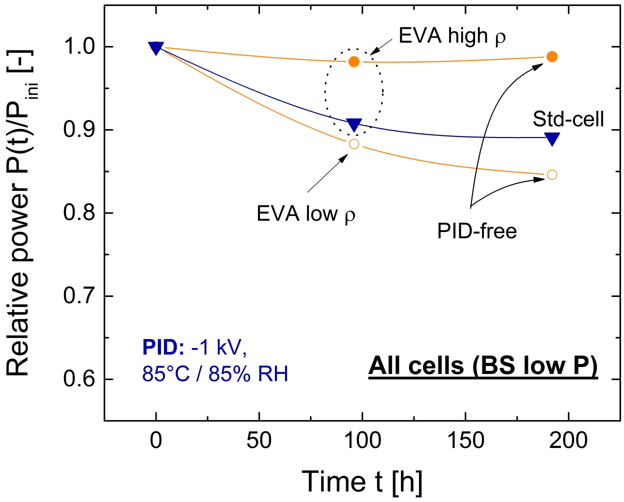

Figure 6.4: Degradation after PID test (85°C/ 85% RH, −1 kV) of a standard cell encapsulated with a high-ρ EVA, and of two PID-free cells with a low- and a high-ρ EVA encapsulant. All samples have a low breathability BS.

Another result worth highlighting is that, apparently, the breathability properties of the backsheet have no significant influence on PID degradation at least in constant and harsh accelerated-aging testing conditions. As Figure 6.2 (b) shows, the volume resistivity of EVA is reduced by increased water content in the film, so that the latter finding is a bit counter-intuitive (see [140]), but is clarified with the water ingress simulations results presented in Section 6.4. We show therein that, with the high levels of humidity used in the PID test (*i.e.* 85% RH), the water diffusion dynamics experiences a moderate delay only of ~10 h for the mini-modules encapsulated with, respectively, backsheets with high and low WVTR.

6.3.4 Influence on PID degradation of moisture ingress in the module sandwich

To better understand the effect on the evolution of PID of the backsheet and of moisture ingress in the module sandwich, we run a second set of experiments manufacturing module structures with increased resistance properties against water ingress: (1) glass/glass (G/G), and (2) glass/glass with edge sealant (G/G-seal). The rear glass is used to prevent water ingress from the back, and the edge sealant (desiccant-filled polyisobutylene- (PIB-)based) to perfectly seal the module edges. In this respect, the latter sample can be considered as a reference sample fully impermeable to water ingress, at least for the first several hundreds of hours of exposure in a climatic chamber, before the edge seal is completely saturated with water [74], [76].

In order to verify that the rear glass is not contributing in worsening the PID effect as an additional source of Na, we manufactured an additional sample (3) using a backsheet impermeable to water that includes a laminated Al foil barrier (G/BS-bar). The full set of mini-modules used in this second run of experiments is made using standard cells only, and (in order to avoid the risk of an accelerated degradation, which would not allow us to distinguish the contributions of the different rear covers) the EVA with high volume resistivity (EVA-high-ρ). All these samples are tested at 85/85 test conditions (*i.e.* 85°C, 85% RH, −1 kV) with a duration extending up to 576 h. The results are shown in Figure 6.5.

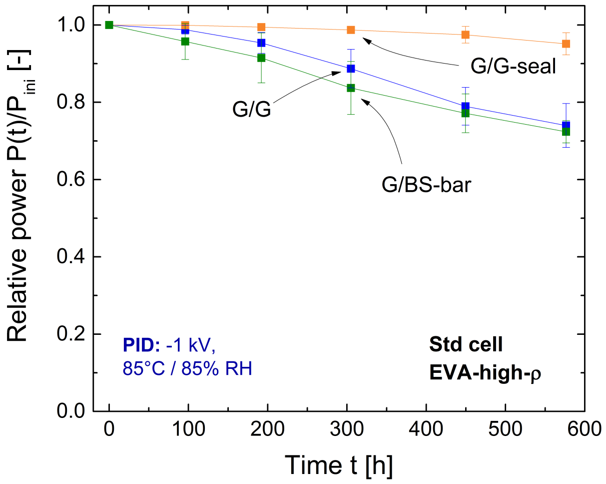

Figure 6.5: Degradation after exposure to PID test (85°C, 85% RH, −1 kV) of the mini-modules built with structures with different water-resistance properties: a glass/glass (G/G), glass/glass with edge sealant (G/G-seal) and a glass/backsheet that includes a laminated Al barrier foil (G/BS-bar). All samples are manufactured with standard solar cells and a highly resistive EVA.

A clear difference is observed between sealed and non-sealed samples: with a power loss limited to −4.9%, the edge-sealed glass/glass experiences only a minor degradation after 576 h of test. In the absence of an edge sealant, the power loss of the glass-glass sample is already −4.6% after 192 h, and reaches −26%, at 576 h (*i.e.* more than 5 times the degradation of the edge-sealed samples). We attribute this difference to moisture penetration from the edges and diffusion over time into the front EVA encapsulant of the unsealed G/G sample. This is consistent with the observations of Figure 6.2 (b) that the resistivity of EVA is affected to some extent by the inclusion of water in the encapsulant layer.

In addition, we want to stress that by preparing a mini-module with conventional c-Si cells and EVA with high volume resistivity in a G/G configuration, in combination with the use of an edge-sealant, we are able to realize a device that withstands the harsher 85/85 PID stress test conditions without nearly any observable degradation during the first 300 h of test, and reaching -5% only after 576 h. Because the time required for water to penetrate beyond a desiccant-filled PIB-based edge sealant at 85/85 conditions is typically around 5000 h [74], [76], we attribute this power degradation to (i) an ingress of water due to a possible loss of adhesion between the edge sealant and the glass or (ii) a late activation of the PID process in presence of a very high resistivity encapsulant, or a combination of the two options.

Further, by comparing the impact of PID testing on the G/G and the G/BS-Al samples, we highlight as well that the samples with a rear glass sheet do not suffer from increased degradation. In fact, the degradation is slightly lower. The p-type Si Al-BSF solar cells exposed to a negative voltage with respect to ground will still drive a migration of Na ions from the rear glass pane to the cell. Nevertheless, these Na+ target the rear Al metalization of the cell, with no impact on PID, and not the anti-reflective coating (ARC) of the cell's front side nor the p-n junction. In this type of cells, it is in fact the drift of Na ions from the ARC layer that can lead to the creation and decoration of stacking faults by the alkali metal ions. This will in turn induce a severe shunting of the p-n junction with a consequent degradation of overall cell performance as we described in Chapter 3 [43], [115], [111], [113]. This physical model, for which consensus exists in describing PID degradation in mainstream Al-BSF p-type solar cells, does evidently not apply when the positively charged ions target the rear side metalization of the solar cells.

Finally, to summarize these last findings we plot in Figure 6.6 the results for the first 192 h of PID testing, highlighting the strong impact that the rear cover and the use of an edge sealant have on the evolution of the PID phenomenon.

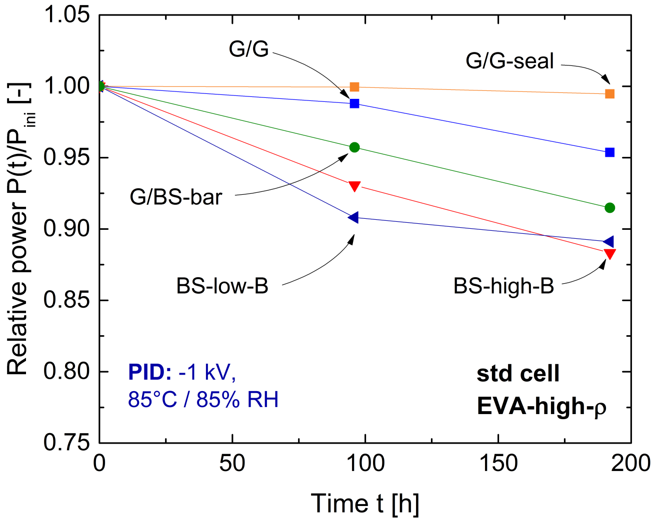

Figure 6.6: Evolution of the PID degradation during the first 192 h (85°C/ 85% RH, −1 kV) for all the mini-modules manufactured with conventional p-type c-Si solar cells and a highly resistive EVA. The different sandwich structures are: glass/glass (G/G), glass/glass with edge sealant (G/G-seal), glass/backsheet including a laminated Al barrier foil (G/BS-bar), and the two samples with a conventional polymeric backsheet (with, respectively, a high and a low breathability B).

On the long run (~580 h of PID testing), nearly no difference could be observed in the degradation of the samples with an impermeable rear cover without the edge sealant (G/G and

G/BS-bar, see Figure 5). For shorter stress times (192 h), however, for these same samples, we observe a discrepancy that we cannot fully explain (see Figure 6.6).

6.4 Modeling water ingress in the sandwich structure

In order to better understand the role of the backsheet and the results of Figure 6.5 and 6.6, we run simulations of water ingress into the module sandwhich as described in Section 6.2.3. For both the G/G and G/BS configurations, we remark that the simulated water concentration is overestimated as the samples are framed by an aluminum tape.

For the G/G sample (cross-section displayed in Figure 6.1 (b) at the bottom), we simulate the water diffusion from the edges through the encapsulant during the PID test, where the samples are exposed to environmental conditions of 85°C, 85% RH for 591 h (*i.e.* 576 h+15 h of preconditioning). To do this, we apply Equation (6.1) on a 2-dimensional domain of width and length equal to 0.2 m (the size of a one-cell mini-module). As the high-resistivity EVA used in this work was not characterized in terms of diffusivity properties, we consider the diffusion coefficient D and the solubility S of an EVA polymer of which we measured the WVTR with a Mocon Permatran twin 3/33, as described in Chapter 2. We obtain a value of $D = 8.13 \cdot 10^{-10}$ m^2/s at 85°C, in the range of what found by other authors for standard EVA materials [73], [85]. The encapsulant is assumed to be initially dry (c_{init}=0 g/m^3). As boundary conditions, we set the four exposed surfaces in equilibrium with the chamber environmental conditions obtaining $c_{surf} = c_{sat}$ = 4192 g/m^3 (Henry law at 85°C, 85%).

These data are used to model the water concentration, and the relative humidity with Equation (6.2), in the EVA layer of the G/G sample as a function of the distance from the edges. The results are shown in Figure 6.7. The corresponding resistivity ρ of the encapsulant is then obtained as function of the internal RH according to the relation displayed in Figure 6.2, and is presented in Figure 6.7, showing a considerable gradient from the edges (~6x10^{13} Ω·cm) to the center (~1.3x10^{14} Ω·cm) of the mini-modules. For the G/G-seal sample (with edge sealant), we assume no water ingress throughout the whole duration of the test. The resistivity ρ of the encapsulant is therefore assumed to be constant all over the sample during time and equal to ~1.62x10^{14}Ω·cm (*i.e.* ρ(85°C, 0%RH)).

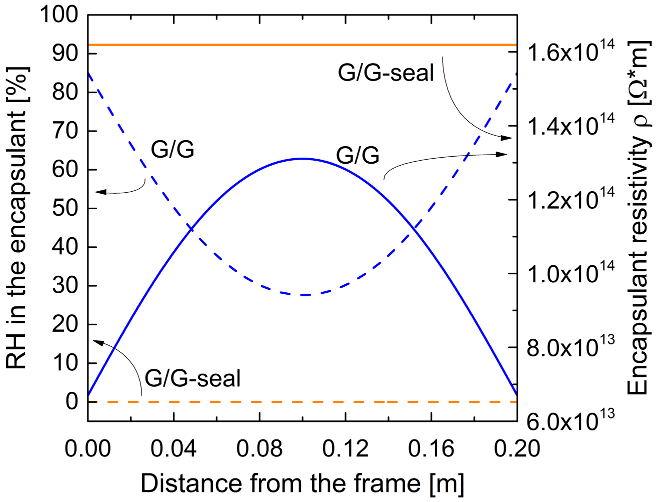

Figure 6.7: Simulated water concentration (expressed as RH) in the encapsulant as a function of the distance x from the edge in our one-cell mini-modules (G/G and G/G-seal samples) after 576 h of PID testing, and the corresponding EVA volume resistivity ρ.

For the case of a G/BS sample (BS-high-B), we simulate the water diffusion into the sandwich during the first 192 h of PID testing by means of FEM, as described in Section 6.2.3. The backsheet diffusion coefficient and solubility were determined by means of WVTR measurements with a 7001 Water Vapor Permeation Analyser. The backsheet and encapsulant are assumed initially dry, and their exposed surfaces in equilibrium with the chamber environmental conditions.

We then calculate the corresponding resistivity of the encapsulant along a line in the front EVA, at half distance between the EVA and the glass (see the red line in the cross-section presented in Figure 6.1 (b)). As shown in Figure 6.8, the mismatch in the distribution of ρ along the encapsulant layers for the two samples explains why the PID dynamics in the G/BS sample is faster than for the G/G samples.

Similarly, for the same geometry of the G/BS sample we simulate the case of two backsheets with respectively low and high breathability. The results (not shown here) show that at the stress conditions used in the PID test (85°C/ 85% RH), the water diffusion dynamics experiences only a moderate delay of approximately 10 h for the mini-modules encapsulated with a BS with lower WVTR, compared to those with a higher WVTR BS. This observation explains why, during the execution of test at 60/85 and 85/85 stress conditions for 96 h and longer, no difference can be noticed for the samples having a BS with a high or low breathability.

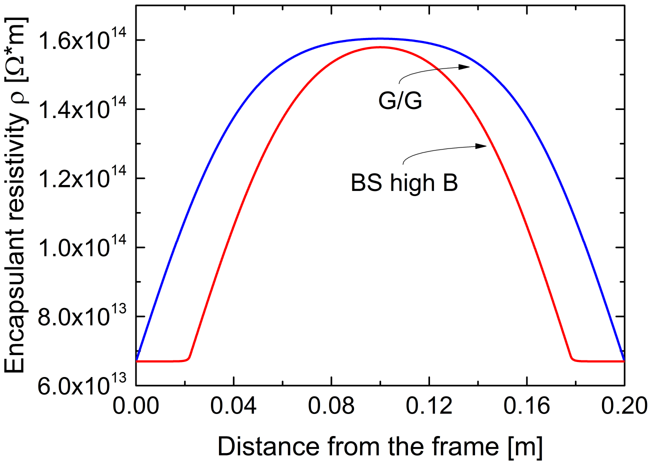

Figure 6.8: Encapsulant volume resistivity ρ as function of the distance x from the frame after 192 h of PID testing (85°C, 85% RH). The red and the blue curve refer, respectively, to the G/BS and the G/G configuration.

6.5 Discussion

We briefly highlight some cost considerations that might enable to select the best strategy to minimize PID, especially considering the industry downward pressure on costs. These include:

1. The potentially high cost for modified module glass, which makes this option difficult to be adopted;
2. The great commercial advantage for module manufacturers to offer solutions independent on the inverter choice and the electrical layout and, therefore, suitable for all systems. A sort of *one-type-fits-all* module;
3. At today's prices, the relatively low cost for using EVA encapsulants with higher volume resistivity (approximately, a +1-5% cost at module level), which, independently from the cell selection, has a considerable impact in preventing PID;
4. Even if alternative encapsulant materials known to prevent PID due to their high volume resistivity (such as PO, ionomer, etc.) are considerably gaining momentum, EVA is still the encapsulant with the longest track-record and the widest market share in the industry (≥90%), which makes it difficult to compete with in terms of prices;
5. At the cell level, the cost to manufacture *in-house* PID-free cells or to buy such cells might vary, even considerably, from one manufacturer to the other;
6. The additional potential advantage that the selection of materials/components less prone to favor water ingress in the sandwich structure (*e.g.* glass/glass vs glass/backsheet, the use or not of edge seals) have on delaying PID dynamics.

6.6 Conclusion

When using breathable backsheets based on polymeric materials, our results clearly indicate that to have a “PID-free” module the combination of PID-free cells and a high-resistive EVA encapsulants is the most recommendable choice. Remarkably, the use of a conventional c-Si cell in combination with a high-resistive EVA encapsulant is more effective (and possibly constitutes a cheaper solution) than the use of PID-free cells in combination with low-quality EVA.

The strong acceleration in PID degradation promoted by 85/85 rather than 60/85 stress conditions can be easily explained by the considerable dependency on temperature of the volume resistivity ρ of the EVA encapsulant, which drops by approximately one order of magnitude over a 30°C interval.

As our resistivity measurements on EVA films indicate that ρ is reduced as well by increasing the water concentration in the film, we are initially surprised to observe that the breathability properties of the backsheet have apparently no influence on PID degradation. An observation that we are later able to explain by running some simulations of water diffusion in the encapsulant for different sandwich structures.

A second set of experiments using sandwich structures with increased resistance to water ingress (*i.e.* glass and backsheet with barrier layers as rear covers and an edge sealant) indicates, in fact, that preventing or reducing the diffusion of moisture in the front encapsulant layer plays a role in further mitigating the impact of PID. We highlight, for example, that by preparing a mini-module with conventional cells and high resistivity EVA in a glass/glass configuration, in combination with an edge-sealant, we are able to realize a device that withstands the harsh 85/85 PID stress test conditions without nearly any observable degradation during the first 300 h of test, and reaching −5% only after 576 h.

For the cell types used in our tests, p-type c-Si Al-BSF, having a glass layer at the rear of the cell does not add to the PID effect compared to having an impermeable rear sheet but not containing Na (*i.e.* the BS with Al layer). The results of our tests indicate on the contrary that a glass/glass configuration is more PID-resistant than a glass/backsheet one, at least during the first 192 h testing hours. We attribute this difference to the higher barrier against water ingress provided by the double glass construction, and the consequent higher front encapsulant resistivity as shown by our simulations.

7 Module interconnection failures

As discussed in Chapter 1, we identified two degradation modes that are of high concern for PV modules reliability: PID and failures in the electric interconnections. In this chapter we address the second topic. We quantify experimentally for the first time the effect of broken interconnection ribbons on the power performance of a PV module, and propose an electrical model able to reproduce the experimental results. For the terminology used, the reader may refer to Chapter 1.2, where the different metalizations and electrical interconnections of a PV module are introduced.

The results shown in this chapter are presented in a paper that has been submitted to *Progress in Photovoltaics*. The complete list of coauthors is reported in Ref. [3].

To perform the experimental work, we manufacture two strings of six cells each and analyze different configurations of disconnected ribbons. The cells have three busbars and are serially connected. We observe that the power loss strongly depends on the ribbon's position with respect to the cell (external *versus* central ribbon). For example, if one of the two external ribbons is disconnected from every cell in the string, the power variation for the string with respect to the initial condition (*i.e.* all ribbons connected) is -10.24%. If, alternatively, we disconnect the central ribbon from all the cells the power loss is limited to -5.91%.

Then, we present a model in LT-SPICE to simulate the performance of a string with disconnected ribbons, and utilize the results presented in the first part of the chapter to validate it. This model was developed by Jacques Levrat from CSEM (Centre suisse d'électronique et de microtechnique). Each three-busbar cell is described as a network of three parallel sub-cells, each sub-cell being modeled with a two-diode equation. The series resistance is accurately represented by the full set of front and rear cell metalization, front and rear interconnect ribbons, and string interconnects.

The simulation results agree with the measured values, for the different configurations of disconnected ribbons. The relative variation in the electrical parameters (maximum power P_{max}, fill-factor FF, and series resistance R_s) after each cut is reproduced with good accuracy.

In addition, simulated current-voltage (IV) curves show a round shape at the maximum power point, which is typical of a R_s affecting only one part of the cell, and closely follow the measured IV curves.

We then use the model to demonstrate that these results are scalable irrespective of the number of cells connected in a string, and show that the results are directly transferable to the case of large-area modules composed of 60 or 72 cells. Finally, we analyze the case when the disconnections are distributed randomly in the module. As a first approximation, we conclude that a module with 10% of disconnections has a power variation between -1.34% and -2.75% in average, while 20% of disconnections lead to a power variation in the range of -2.83% and -5.64%.

7.1 Introduction and motivation

As discussed in Chapter 1.2, failures in the internal circuitry of a PV module have a major effect on its performance [51]. A R_s increase is often observed in field modules (see, *e.g.*, [71] and [22]) and can originate from different degradation mechanisms.

Interconnection failures are generally caused by thermo-mechanical fatigue. Because of the different coefficients of thermal expansion of the materials in the module sandwich (*e.g.*, cells, encapsulant, glass, backsheet), thermal variations result in a displacement of solar cells in the module. The same effect can occur when the module is exposed to mechanical stresses, *e.g.*, due to wind or snow loads.

The stress induced by thermo-mechanical loads induces fatigue on the contact (solder bond, also called solder joint) at the interface between the cell interconnect ribbons and the cell busbars. In the long term, the solder joints can develop micro cracks and ultimately fail (*i.e.* partially or completely detach). In extreme cases, fatigue can cause a complete rupture of the ribbons with a consequent complete disconnection from the circuit. Resistive solder bonds can also lead to the formation of hot spots ([107] and [67]).

Besides thermo-mechanical stresses, the performance of the interconnections can also be affected by the presence of moisture or acids in the encapsulant, such as the acetic acid generated by the photo-thermal degradation of ethylene vinyl acetate (EVA). Such stress factors can cause corrosion of the copper core and the tin coating of the ribbons, as well as of the solder bonds or the cell fingers (see *e.g.* [68] and [52]). In [24] the authors show that, in hot & humid climates, the loss in P_{max} is directly correlated to the loss in FF (whereas this is not the case for other climates). As mentioned in Chapter 1, browning of internal circuitry due to corrosion was directly correlated with significant power losses in [68].

The reliability of ribbons has gained increasing attention in the last few years. In [102], the authors investigate the fatigue behavior of copper ribbons resulting from temperature cycles and obtain a relationship between a temperature cycle's amplitude and the number of cycles to failure (*i.e.* to a ribbon's breakage). Finite Elements Method (FEM) simulations are employed in [26] to reproduce the cell displacement and stress distribution within module materials resulting from thermal variations. In [12], Bosco *et al.* propose a climate-dependent number of thermal cycles (according to the IEC 61215 standard [56]) as a stress test for modules in order to obtain an equivalent amount of solder fatigue damage as simulated by FEM. In [121], the authors simulate with FEM models the plastic strain energy accumulated by the ribbons during cyclic mechanical loading due to wind.

However, to our knowledge, there is no experimental study directly assessing the actual impact of broken cell interconnect ribbons on the electrical output of the module. In this chapter, we investigate how the module performance is affected when one or more ribbons are broken. We quantify by experimental measurements the actual impact on the electric performance when one or more ribbons connecting adjacent cells are disconnected. We propose a simplified electrical model in LT-SPICE that is able to reproduce experimentally measured IV characteristics, and the variation in the module's electrical parameters induced by the breakage of the cell interconnect ribbons.

7.2 Experimental work

To perform the experimental work, we manufactured two equal strings (String A and B), each with six solar cells connected in series with commercially available 1.70 × 0.17 mm copper ribbons coated with $Sn_{62}Pb_{36}Ag_2$. The cells are monocrystalline silicon (c-Si), p-type, with three busbars. The encapsulation is done with a glass/backsheet construction with EVA as the encapsulant. For the backsheet we employed a 50- µm-thick ethylene tetrafluoroethylene (ETFE) sheet, a thin layer that can be easily removed allowing us to cut the selected ribbon without the risk of damaging adjacent cells.

Each string is employed to analyze a specific configuration of disconnected ribbons. We characterize initially the single strings by means of IV measurements using a LED-halogen-based sun simulator that replicates the AM1.5 spectrum. We also take electroluminescence (EL) images, for which a DC current (corresponding to the module's short-circuit current) is supplied in order to stimulate radiative recombination of carriers and consequent light emission. EL images allow us to observe the path that the light-generated carriers follow in presence of disconnected cells.

After the initial characterization of the module, we cut the interconnect ribbons from one or more cells using an iterative process. When needed, disconnected ribbons can be repaired by soldering before proceeding with the following step. For each cell, we distinguish between the central ribbon and one of the two external ribbons, for which the side is irrelevant due to their symmetry. The change in the string performance is measured after each step by means of IV and EL measurements.

7.2.1 One disconnected ribbon per cell

We compare here the impact on the module's electrical performance of a broken external *versus* the central ribbon. String A, for which we cut the central ribbon, is illustrated in Figure 7.1. The positions where the ribbons are cut are labeled by progressive numbers (1,...,7). After initial electrical characterization of the strings we cut the external or the central ribbon, starting from position 1 and progressing through position 7. Because the front and the rear contributions to the cell series resistance have different values (see Section 7.3), it is important to note that the ribbon is disconnected starting from the front of the cell. In Figure 7.2 we plot the change in FF and P_{max} of the full string after progressively removing one ribbon at a time. The loss in P_{max} (circles) follows, as expected, the same trend as the loss in FF (triangles). With a power loss per cut of, respectively, −1.51% and −0.85%, we observe a more pronounced degradation when the external ribbon is disconnected.

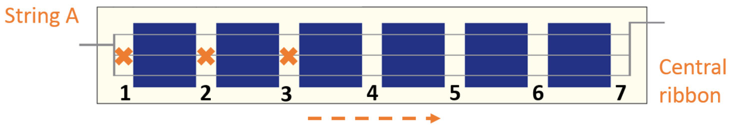

Figure 7.1: Scheme of one of the six-cells strings. In this case, the central ribbon is sequentially cut between consecutive cells (from position 1 to position 7). The same type of string is manufactured to analyze the case where one of the two externals ribbons is removed (String B, shown in Figure 7.4).

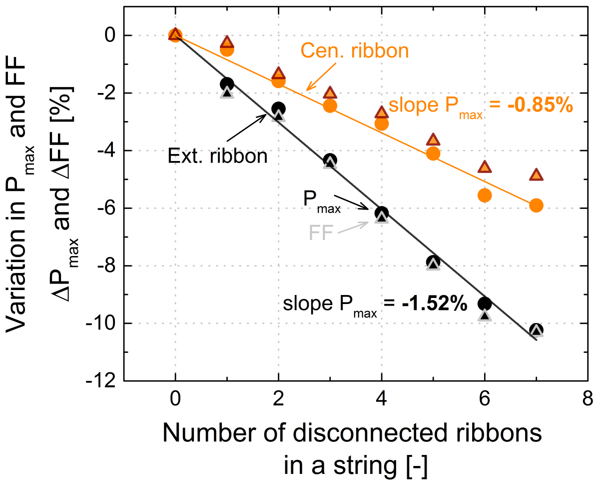

Figure 7.2: Change in P_{max} (circles) and in FF (triangles) with respect to the initial values (all ribbons connected) as function of the number of cumulative cuts. For instance, two disconnected points means that the ribbon was cut in both positions 1 and 2 (see Figure 7.1). Dotted lines are linear fits of P_{max}.

The difference is reflected in the EL images in Figure 7.3. When we cut the central ribbon (top image), a smaller part of the cell is dark, *i.e.* contributing less to carrier collection, than when we cut an external ribbon (bottom image). As a general observation, denoting by ℓ the distance between the central ribbon and an external one, in the first case the maximum distance that light-generated carriers have to travel through the metallic fingers from the center of the cell to the closest connected ribbon is ℓ. In the second case, instead, the maximum distance that carriers have to travel from the external part of the cell to the closest connected ribbon increases to $\ell + \ell/2$.

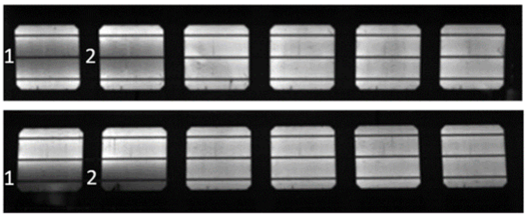

Figure 7.3: EL images of the six-cell strings: (top) The central ribbon is cut at positions 1 and 2, and (bottom) an external ribbon is cut at positions 1 and 2. The dark area indicates where less carriers are being collected. The string is supplied by a current of the value of the string's short circuit current, I_{sc}.

7.2.2 Two disconnected ribbons per cell

After having completely disconnected the external ribbon for all cells in String B (positions 1 to 7), we continue removing iteratively a second ribbon (the central one), as shown in Figure 7.4. Figure 7.5a shows the corresponding P_{max} variation. Here, the cuts in the central ribbon are plotted as consecutive to the previous cuts in the external ribbon (*i.e.* a cut in position n of the central ribbon corresponds to the x-coordinate $7 + n$). In this case, each cut in the central ribbon reduces the power by 3.76%, whereas with the external ribbon still connected the power reduction was only 0.85%/cut (Figure 7.2).

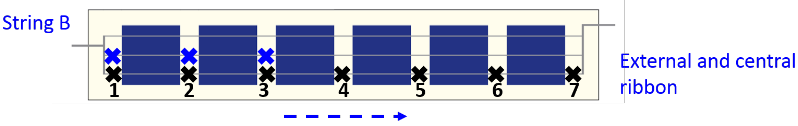

Figure 7.4: Scheme of String B. First an external ribbon is cut sequentially from position 1 to position 7, and then the central ribbon is cut sequentially from position 1 to position 7.

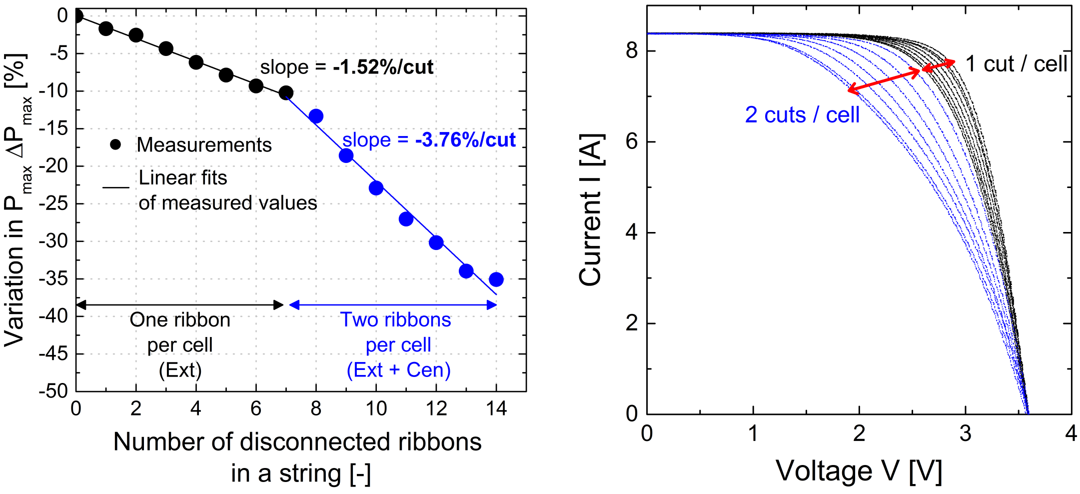

(a) (b)

Figure 7.5: (a): Change in P_{max} with respect to the initial values (*i.e.* all ribbons connected) of the P_{max} of String B as a function of the number of cumulative cuts. First the external ribbon is cut sequentially from position 1 to position 7, and then the central ribbon is cut sequentially from position 1 to position 7. (b): Measured IV curves for configurations from 0 to 14 disconnected points, corresponding to the P_{max} values in (a).

The corresponding variation of the R_s for the discussed configurations is shown in Figure 7.6. These values refer to the R_s of the full string in consideration (and not the R_s of a single solar cell). They were obtained from the one-sun IV curve by means of a linear fit in proximity of the open-circuit voltage (V_{oc}), which provides the slope $1/R$. We use this value (R_{oc}), which is generally higher than the true R_s of the device, as an approximation for R_s. Fitting the IV curve with the one-diode equation, indeed, resulted to be an inaccurate method to extract the R_s. This can be related to what was observed by Bowden and Rohatgi in [13]: when only part of the cell is affected by a high R_s (inhomogeneous distribution of the series resistance) the effects of this high R_s on the IV curve may be erroneously attributed to other electrical parameters of the curve instead, for instance to a low shunt resistance. As can clearly be observed by the peculiar shape of the IV curves displayed in Figure 7.5b, our case, with the disconnections affecting only a limited portion of the cells, falls within the cases described in [13] and would therefore require specific measuring procedures and a dedicated R_s extraction method. Nonetheless, here we are mainly interested in observing a trend for the variation of R_s, rather than measuring absolute values, and a linear fit in proximity of V_{oc} provides us with more robust and reproducible results.

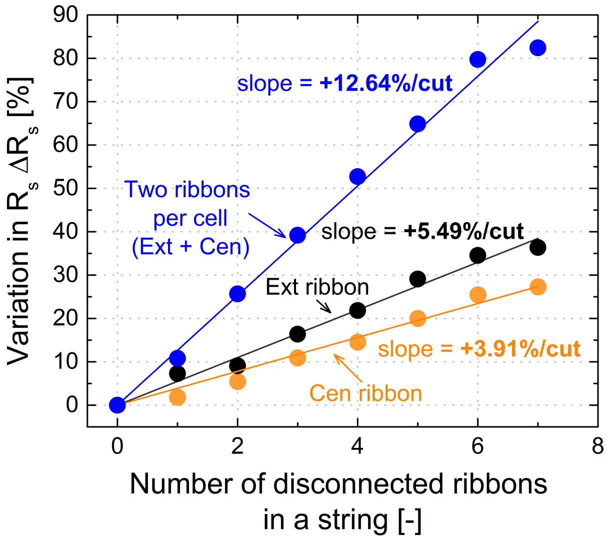

Figure 7.6: Change in series resistance, R_s, as a function of the number of cumulative cuts. Black and blue circles refer to String B. For the blue circles, n disconnected ribbons means that the external ribbon was cut in positions 1 to 7, and the central ribbon was cut from position 1 to n. Lines are linear fits.

As Figure 7.6 shows, the increase in R_s is higher when disconnections are in the external ribbon rather than in the central ribbon. This justifies the corresponding trend for the loss in FF and the P_{max} seen in Figure 7.2. When the external ribbon is already completely disconnected for all cells in a string, each cut in the central ribbon increases the R_s by around 13%, with an impact on R_s approximately three times higher compared to when the external ribbon is disconnected.

7.3 Modeling the performance of cells/strings with an inhomogeneous distribution of the series resistance

In the following, we present a simplified model that was implemented in LT-SPICE (version 4.23I) to simulate the electrical performance of a string with disconnected ribbons. The experimental results presented in Section 7.2 are utilized here to validate the model. This model was set up by Jacques Levrat from CSEM [3].

7.3.1 The electrical model

In the previously described experiments, ribbons are cut sequentially forcing the electrical current to be collected through the neighboring ribbon(s). The symmetry of the three-busbar H-pattern invites us to consider the cell as three sub-cells connected in parallel, each being represented by a two-diode model featuring one internal R_s, one shunt resistance R_{sh} and two saturation currents (I_{01} and I_{02}) with ideality factors $n_1 = 1$ and $n_2 = 2$, respectively. To reproduce the current redistribution within the cell when one ribbon has been severed, the internal series resistor has been removed from the grid resistance terms, *i.e.* $R_{G,f}$ and $R_{G,b}$, for the front and the rear side, respectively. The reason is that these terms relate to lateral transport and should be considered separately as they are involved differently when one ribbon path is missing. The exact scheme considered is depicted in Figure 7.7.

To extract the diode parameters experimentally, one of the cells was measured in the four-terminal configuration within the module environment. A nonlinear fit of the IV curve provides the following diode parameters: $J_{01} = 5.2 \cdot 10^{-10}$ A/cm^2, $J_{02} = 1.1 \cdot 10^{-5}$ A/cm^2, $R_{sh} = 40\ \Omega$ cm^2. The internal series resistance (free of the grid contribution) is derived from the fitting of the full module measurement yielding $R_s = 4$ mΩ cm^2. As the cell is monofacial, $R_{G,f}$ corresponds to the resistance between two front busbar and $R_{G,b}$ to the rear metal blanket resistance value between two backside ribbons. A four-terminal measurement yields $R_{G,f} = 25$ mΩ and $R_{G,b} = 1$ mΩ . As all ribbons are the same size, they are modeled by a single-value contribution $R_{ribbon} = 3$ mΩ. The only adjustable parameter of the model is the parasitic resistance $R_{connector}$ induced by the crocodile connectors used during the IV measurement. Experimental data were accurately fitted with $R_{connector} = 3$ mΩ.

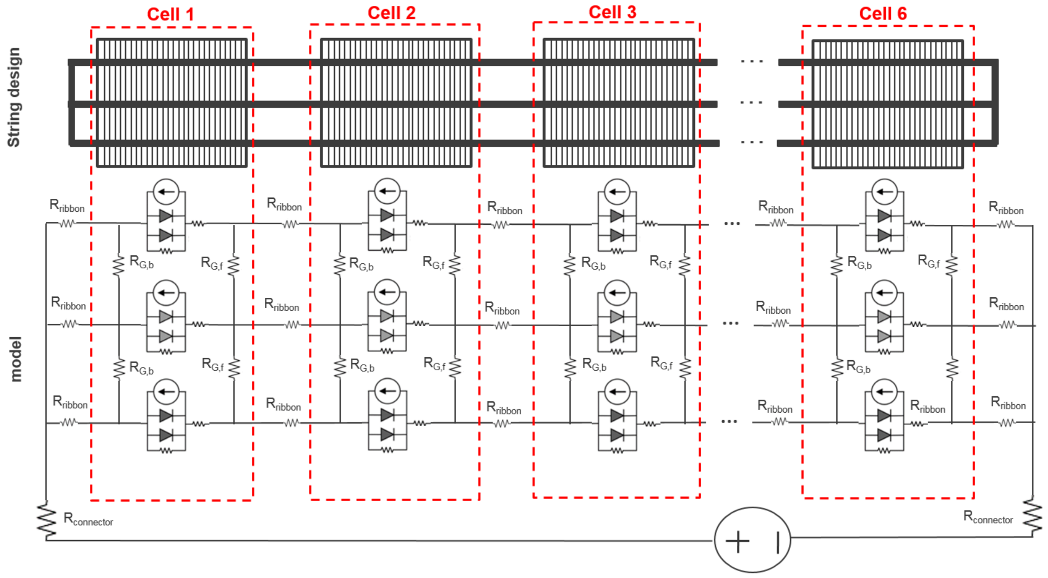

Figure 7.7: Schematic representation of the LT-SPICE model considered to simulate the 6 × 1 cell string.

7.3.2 Comparison of experimental and simulation results

When only the central ribbon is disconnected (String A), the simulated IV curves fit the measured ones with good accuracy for the different steps, as can be seen in Figure 7.8. The variation of the P_{max} and of the FF obtained from the simulations also closely reproduce the measurements, with a relative error always less (in absolute value) than 1% for the P_{max} and 0.50% for the FF. For the R_s the relative error is around −10% in the extreme cases of 6 and 7 cuts, where the simulated curves are slightly above the measured ones, whereas for the other cases it is on average −7.22%. This discrepancy can be attributed to the fact that, as mentioned, the value of series resistance estimated from the measurements is the R_{oc} , which is generally higher than the true value of R_s determined by fitting the IV curve with the two-diode equation and obtained from the simulations.

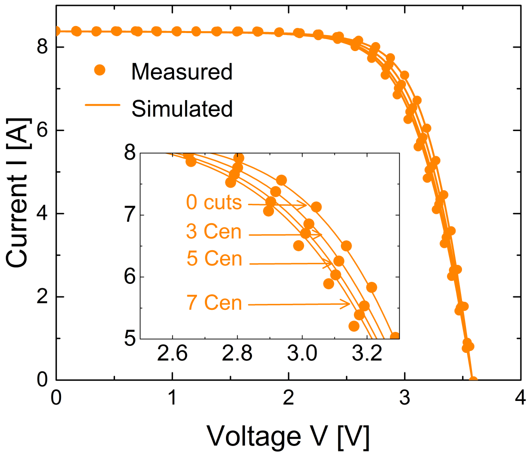

Figure 7.8: IV curves of String A: measured (dots) and simulated (lines). The central ribbon is sequentially cut between consecutive cells.

In the configuration in which both an external and the central ribbons are disconnected (String B), our model also predicts the variation of the electrical parameters with a good accuracy. Figure 7.9 illustrates the relative change of P_{max} and R_s with respect to initial values at each step. As we proceed in cutting the external ribbon, the trend of the simulated values closely follows the measured one. Further, the model is able to reproduce with a good approximation the change in the slope observed experimentally as soon as the central ribbon starts to be disconnected too (corresponding to points 8 to 14 in the x-axis). In this case as well, the overlap of simulated and measured IV curves is very good (see Figure 7.10). It is worth noticing that our model is able not only to reproduce the variation in the curve slope close to the open-circuit point (correlated with R_s), but also the peculiar shape of the IV curve of a cell in which part of the cell is affected by a high series resistance as discussed in Section 7.2.2. Table 7.1 summarizes the P_{max} and R_s values obtained from simulations and measurements, and their differences normalized by the measured values.

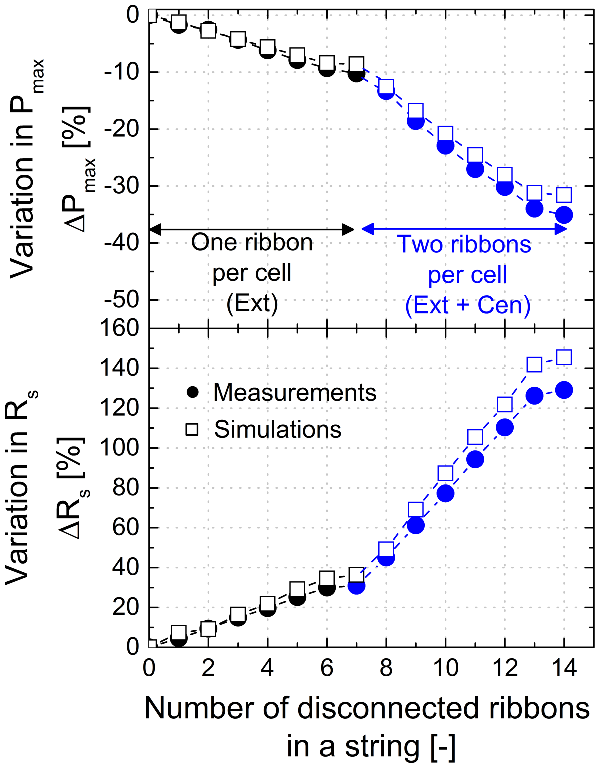

Figure 7.9: Relative variation of P_{max} (top) and of R_s (bottom) for String B with respect to initial values as a function of the number of disconnected points. The values from 0 to 7 cuts are the same as in Figure 7.2 (Ext) and Figure 7.6 (Ext).

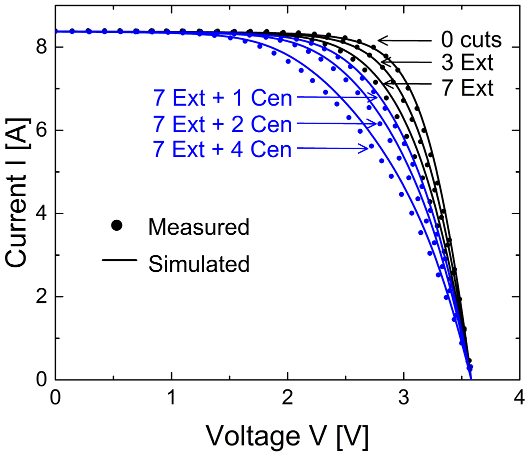

Figure 7.10: IV curves of String B: measured (dots) and simulated (lines). First the external ribbon is cut sequentially between adjacent cells (black) until all seven positions are disconnected, then the central ribbon is also cut sequentially from each cell (blue). A good agreement is observed.

Table 7.1: Summary of the maximum power P_{max} and series resistance R_s values of String B as simulated and measured, and their relative differences (Diff.). The differences in the FF are not reported as they are similar to those in the P_{max}, in both the value and the trend. The measured and simulated values of the short-circuit current and of the V_{oc} remain unvaried after the disconnections of the ribbons (as can also be seen in the IV curves, Figure 7.10).

		P_{max} [W]			R_s [Ω]		
Number of cuts	Config.	Simul.	Meas.	Diff. [%]	Simul.	Meas. [Ω]	Diff. [%]
0	Initial	22.13	22.17	−0.18%	0.050	0.055	−9.09%
1	1 Ext cut	21.85	21.80	0.23%	0.053	0.059	−10.17%
3	3 Ext cuts	21.20	21.21	−0.05%	0.058	0.064	−9.38%
5	5 Ext cuts	20.57	20.42	0.73%	0.063	0.071	−11.27%
7	7 Ext cuts	20.22	19.90	1.61%	0.066	0.075	−12.00%
8	7 Ext + 1 Cen cuts	19.35	19.21	0.73%	0.073	0.082	−10.98%
10	7 Ext + 3 Cen cuts	17.52	17.09	2.52%	0.089	0.103	−13.59%
12	7 Ext + 5 Cen cuts	15.93	15.48	2.91%	0.106	0.122	−13.11%
14	7 Ext + 7 Cen cuts	15.14	14.39	5.21%	0.115	0.135	−14.81%

7.4 Extension of the results to large-area modules

In this last section, we comment about the extension of these results and of the model to large-area modules, such as devices made up of 60 or 72 cells (*i.e.* typical commercially-available modules). The results previously presented, where the cuts are induced progressively in the same ribbon (external or central), are scalable irrespectively of the number of cells connected in a string. From the simulations we see, for example, that if an external ribbon is disconnected from all cells with three busbars in a string of say 6, 12, 18, ..., 60 or 72 cells, the overall power variation will always be approximately −10%. Similarly the overall power variation will be ∼ −5.9% if the disconnected ribbon is the central one.

We finally analyze the case where disconnections are randomly distributed in the module. In view of the considerations above, we consider a module of six three-busbar cells connected in series. The number of disconnections is expressed as a percentage of the maximum number of possible disconnections, so that the results presented can be also interpreted in terms of large-area modules. The maximum number of disconnections, corresponding to the configuration with 100% of cuts, depends on: (i) the number of cells in the module, and (ii) the number of busbars in the cells. For our mini-module made of six cells with three busbars, the configuration corresponding to 100% of disconnected ribbons corresponds to 21 cuts (*i.e.* $7 \times 3 = 21$). For 60 or 72 cells module, with six strings made of respectively 10 and 12 cells with three busbars, 100% of disconnection would correspond to 198 and 234 cuts (*i.e.* $(n+1) \times b \times m$, where n, b, and m are, respectively, the number of cells, the number of busbars, and the number of strings). For the sake of brevity, we present two particular cases with10% and 20% of overall disconnections (*i.e.* respectively 2 and 4 randomly distributed cuts in our mini-module) and asses the overall power reduction. For each case, we analyze 10 random configurations, some of which are represented in Figure 7.11.

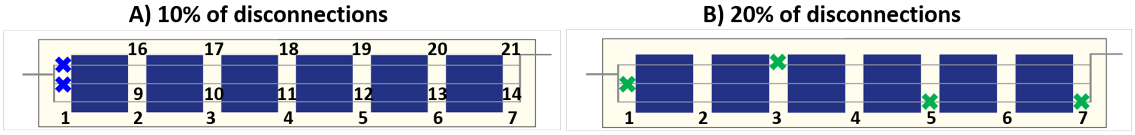

1A) 2 ribbons per cell

1B) 1 ribbon per cell

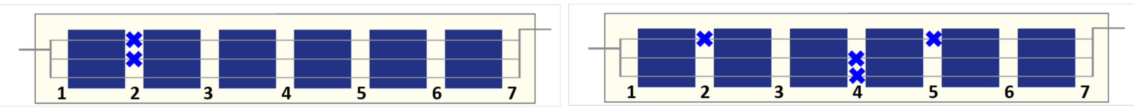

2A) 2 ribbons per cell

2B) 2 ribbons per cell

Figure 7.11: Some of the 20 configurations employed to analyze the impact on power loss of disconnections in random points. We consider a string of six cells with three busbars having 2 or 4 disconnected points. The results can then be applied to the general case of a large-area module having 10% and 20% of disconnected points. As the effect on power variation is strongly linked to the number of disconnections per cell, we denote with different colors the configurations where a cell is affected at most by one disconnection (in green) or can present two disconnections (in blue).

The resulting power loss is shown in Figure 7.12 (10 values for the 10% case and 10 values for 20%) where, as in the string images (Figure 7.11), we additionally distinguish the cases where the cuts concern one or two ribbons per cell (green and blue dots, respectively). The two cases considered in the sections above, where the disconnections are induced sequentially in the central or in an external ribbon, are also reported as reference. For the configurations considered here, the averages of the power loss lie within the band comprised between the lines for the central and Ext ribbon disconnections (orange and black), *i.e.* between −1.34% and −2.75% for 10% of cuts, and between −2.83% and −5.64% for 20% of cuts. We can thus conclude as a first approximation that the lines corresponding to disconnections in the central and external ribbon identify a sort of upper and lower boundary (or oscillation band) for the power loss of random configurations. We also observe that when two disconnections concern the same cell two possibilities occur. If the cuts are at the string end (*e.g.* configuration 1A in

Figure 7.11) the power loss is contained and generally lies inside the band or even above. Big deviations below the band are observed instead if the cuts are internal in the string (such as in configurations 2A and 2B). We should point out that ruptures at the extremity of the string are likely to be the most frequent the field, due to the fact that the thermal variations induce larger displacements on the cells close to the module edges and thus higher strain amplitudes on the ribbons.

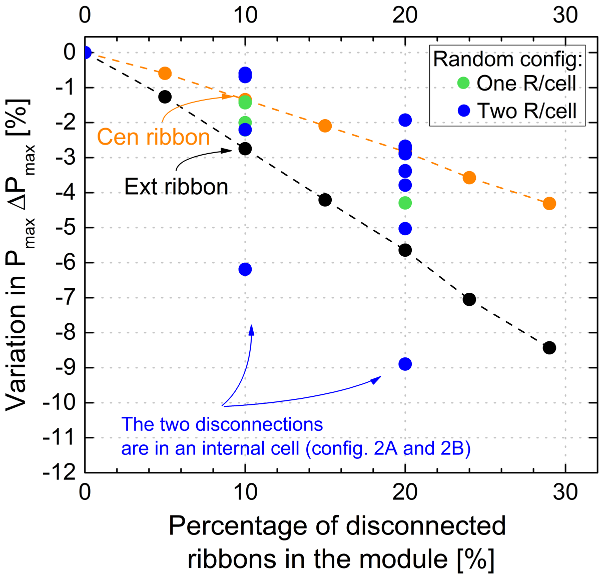

Figure 7.12: Relative variation of P_{max} as a function of the percentage of overall disconnected ribbons in the module. All the results are obtained from simulations, and the values for the external ribbon with the dashed fitting line are the same as in Figure 7.5. For the cases of 10% and 20% of overall disconnections, results for configurations with random distributions of cuts are shown. For a 60 or 72 cells module, with six strings made of respectively 10 and 12 cells with three busbars, 10%/ 20% of disconnection would correspond to, respectively, 19/39 cuts and 23/46 cuts. Green dots denote configurations where a cell is affected by at most one cut ribbon, blue dots the cases where two ribbons can be disconnected for the same cell. The configurations where an external ribbon and the central one are progressively cut identify a band within which most of the random cases fall. Big deviation below this band are observed when two cuts affect a single cell and are not at the string extremity (configurations 2A and 2B).

7.5 Summary

As Table 7.1 clearly shows, our model shows its limits when the induced series resistance becomes very high, in particular when two ribbons per cell are disconnected. Our approximation using three sub-cells connected in parallel and connected by the lateral grid resistance is not able to fully reproduce the voltage distribution between terminals. The current generation is assumed to be point-like and not distributed spatially between the ribbons. A more accurate description would distribute a continuum of sub-cells with a discretized current generation. Moreover, alternative paths to lateral conduction, like transport through the wafer are not envisaged and might play a role in the high resistance-limit.

Still, the good agreement between our approach and the experimental results, even for two missing ribbons, is encouraging and provides an indication that the main physical mechanisms have been accounted for.

Finally, we use the model to demonstrate that these results are scalable irrespective of the number of cells connected in a string. These results are not shown here, but, as an example, if an external ribbon is disconnected from all cells with three busbars in a string of say 6, 12, or 18 cells, the overall power loss will be approximately -10%. Similarly the overall power loss will be -5.9% if the disconnected ribbon is the central one.

A complete rupture of interconnect ribbons is a relatively extreme event not frequently observed in field modules, although it could still be triggered by heavy or non-homogeneous loads and by consistent and repeated temperature variations over time. More often, problems with interconnections may involve a partial de-soldering and consequent loss of adhesion of the ribbon from the busbar or from the string interconnect, or corrosion of the metal contacts. All events that lead to an increase of R_s with a consequent loss in FF and P_{max}. The experimental work performed here, with a complete disconnection of the cell's ribbons, should therefore be considered a sort of "worst-case" scenario in assessing the impact of damage to cells' interconnect ribbons to the overall module performance.

Regarding this matter, this model could be adapted to reproduce the impact on device performance of less severe damages such as resistive solder bonds, thereby providing an assessment or prediction of the module performance in more realistic conditions.

Furthermore, considering the industry shift towards high-efficiency cells and the quest for extended module lifetime, one current trend is to increase the number of busbars to *e.g.* four or five busbars (see [17] for example). The main advantages are in enhancing the carrier collection, and reducing the power loss in case of cracks appearing beyond the external busbar and the edge of the cell. An increased number of busbars in fact corresponds to a smaller area at the edge of the cell that would be disconnected from the circuit in case of the appearance of a crack [31]. In addition, advanced busbar-free technologies are getting a foothold in the PV industry. An example is Meyer Burger's SmartWire Connection Technology SWCT®, [142], [28]. Here, multiple wires are bonded to the cell bringing several advantages such as minimization of cell-to-module losses and cost reduction (by avoiding the need for silver for the busbars). Prospectively, our model, validated experimentally with three-busbar cells, should be easily adaptable to the use of more busbars or multi-wire configurations.

7.6 Conclusion

In Section 7.2, we assessed experimentally for the first time the impact of one or more disconnected ribbons on the electrical performance of strings with six cells serially connected. We considered mono c-Si cells with three busbars. If one of the two external ribbons is removed between all the cells, we measured a power variation for the string of −10.24% with respect to the initial condition (*i.e.* all ribbons connected). A reduced power variation, −5.91%, was instead found if the central ribbon is disconnected from all cells in the string. Finally, we measure performance losses of up to −35.08% when two ribbons per cell are disconnected from all cells in the string.

In Section 7.3 we used these experimental results to validate a model developed in LT-SPICE that simulates the performance of a string with disconnected ribbons. Good agreement was found between the simulations and the measurements. The relative variation in the electrical parameters (P_{max}, FF, and R_s) after each cut is well reproduced. Moreover, the simulated IV curves closely follow the measured ones, also replicating the round shape at the maximum power point typical of inhomogeneous distribution of R_s in the cells.

We then used the model to demonstrate that these results are scalable irrespectively of the number of cells connected in a string, and showed that the results are directly transferable to large-area modules composed of 60 or 72 cells. Finally, we analyzed the case in which the disconnections are distributed randomly in the module. As a first approximation, we concluded that a module with 10% of disconnections has a power variation between −1.34% and −2.75% in average, while 20% of disconnections lead to a power variation in the range of −2.83% and −5.64%.

8 General conclusions and perspectives

8.1 General conclusions

- Based on the findings of the work carried out in Chapter 4, we propose a lifetime accelerated test sequence for PID. During the design phase of a PV plant, a certain number of modules should be subjected to such test sequence (at least 12 modules). The parameters of the PID equations characteristic of the specific module type would then be extracted, and used as inputs in the proposed simulation model to predict the long-term performance of the modules in the climate conditions of the planned installation site.
- From our accelerated PID tests, we found the module power degradation to be linearly dependent on the level of applied voltage bias. This was also indicated by some inspections of string performance in PV plants.
- The regeneration curve for samples exposed to illumination depends on the load condition of the sample. Particularly relevant is our observation that regeneration takes place as well for samples exposed to a high negative bias voltage (-1000 V), in conditions of low humidity and high temperature. This effect, for which little evidence existed from field monitoring, is clearly proven by our experimental tests. These results indicate that, besides power degradation during the day and thermally-driven regeneration during the night, daytime regeneration is an additional phase of the PID mechanism that should be included in PID predictive modeling. Regeneration tests under irradiance and voltage should therefore be included in a test sequence aimed at predicting PID. We then found that the degradation level previously reached by the sample plays a major role in the power recovery. For our devices, a threshold of 50% of power degradation is found beyond which the samples do not regenerate completely.
- In Chapter 5, we present simulations of outdoor PID in different climatic conditions based on the proposed model and on the indoor-determined coefficients for the devices tested. Using typical meteorological year (TMY) data for four different locations as inputs, we calculated the nominal power of the mini-modules over 25 years, employing

the Matlab PV_LIB Toolbox developed by the Sandia National Laboratories. We then applied to the nominal power the set of equations determined in Chapter 4 with a time resolution of 1 h, obtaining a prediction of the performance as consequence of PID.

- The prediction of PID cannot be addressed by a single relationship between power loss and climatic data. It is indeed a complex mechanism, which manifests as different phases (power degradation and power regeneration), where for each the initial power conditions depend on the final condition of the previous phase. Therefore, it is not trivial to apply a model developed from accelerated tests (at constant stress conditions), and composed by a set of equations each describing a different phase of the degradation mechanism, to real outdoor conditions where the stresses vary continuously in time. This goal is achieved by making a mathematical adaptation that uses the idea of equivalent time. This method allows us to concatenate equations referred to consecutive time intervals, where the stress conditions may be different, in a consistent way.

- In our simulations, particular attention was paid to the treatment of the meteorological data. Specifically, we introduced some thresholds that distinguish between the different phases of the PID mechanism. By setting a threshold on relative humidity being lower or higher than 40% (based on the results of our accelerated tests), we were able to differentiate the phases of regeneration and degradation occurring during daytime. Furthermore, the integration of a threshold that determines whether the module surface is wet or dry, found by Hacke *et al.* in [34] also constitutes an improvement for the modeling of PID, as a harsh degradation was detected in the field when modules are covered by a film of water.

- The simulation results show a clear impact of relative humidity on the different degradation levels reached in the four climates. Moreover, due to the interaction between temperature and humidity, a similar extent of power loss can occur in a hot climate such as Sicily's and in a temperate climate as in Switzerland. An interesting results is that our simulations are able to reproduce the effect of seasonality that was observed in some modules in operation. Even if further improvements would be needed to our model, such as adding the contribution of irradiance on power degradation, these results are encouraging as they indicate that the general trend of PID on weather conditions is caught by our simulations.

- The work presented in Chapter 6 contributes to a further understanding of PID at the material level. The strategies to prevent PID at the module level are investigated. By testing one-cell mini-modules manufactured with different combinations materials sold as "PID-free" (cells and encapsulant) we assessed the effectiveness of the solutions available on the market and identified some cost-effective possibilities that are offered to module manufacturers to obtain modules with good resistance against PID. We also investigated how the encapsulation structure of a module could be reinforced to mitigate the occurrence of PID, finding for instance that module architectures with increased resistance against water diffusion into the sandwich are less prone to PID.

- In Chapter 7, we focused on the problem of failures in the module electrical interconnections. We assessed experimentally for the first time the impact of one or more disconnected ribbons on the electrical performance of mini-modules made of six serially connected cells. The results of the measurements were used to validate a model implemented in LT-SPICE, finding a very good agreement between the simulations and the measurements.

8.2 Perspectives

- The research conducted to develop a model for PID set the basis for realizing predictions of the effect of PID on the long-term performance of modules in operation in different climates. A crucial point that has to be targeted is the validation of the model with outdoor performance data.

- Even though several aspects related to the meteorological conditions are taken into account in our predictive model for PID, further improvements should include other elements that trigger PID, such as the presence of soiling made of "conductive" particles, as is the case with some types of sand (rich in metallic particles) or of salty mist (close to coastal areas).

- A further improvement of our predictive model would be to investigate the effectiveness of the solutions to recover the performance of PID-affected PV modules in the field (such as "offset kits" that apply a high positive voltage to the full string during the night). For example, the accelerated test sequence that we proposed in Chapter 5 should be easily adapted to include regeneration tests in the dark at different temperatures and with the mini-modules subjected to a high positive voltage.

- The approach presented in Chapter 5 to simulate the effect of PID on modules in operation in different climates can be employed to simulate other degradation mechanisms. The PV_LIB Toolbox by Sandia National Laboratories is a useful tool to calculate the performance of PV modules or systems of given properties (*e.g.* module electrical parameters and cell technology, module mounting configuration) in a given installation site. Meteorological data inputs can be of the typical meteorological year (TMY), useful *e.g.* for making performance predictions, as well as real data series from a certain time period, particularly useful to validate predictive models. Once the nominal module power over the time period of interest is calculated, one may apply the empirical equations previously extracted for the considered degradation mode from suitable accelerated test matrices and concatenating them in the different time intervals with the method shown. We stress, however, that each degradation mode requires a dedicated study.

- For the case of PID, we have considered the module $P_{\max}$ as the parameter to model. An advantage of our approach is that the performance prediction could be based also on the time evolution of other parameters. For example, if a degradation mode requires modeling the R_s, instead, then the equation relating the R_s to the stress factors (*e.g.* temperature or number of thermal cycles) would be applied in the PV_LIB Toolbox simulations, thus providing directly the link with the power loss.

- In order to study in detail the complex mechanism of PID, we have restricted our modeling to PID only. However we recognize that PID might also interact with other effects, for instance water diffusion into the module sandwich. A first relationship between humidity inside the encapsulant and the occurrence of PID has been investigated in Chapter 6 for the case of indoor accelerated testing. Moreover, in Chapter 5 we discussed a possible method to calculate power loss, starting from simulations of the voltage distribution over the module surface, where humidity inside the encapsulant is taken into account through the parameter of the encapsulant resistivity. However, these are only preliminary ideas and more work is required to develop a model for outdoor prediction that combines PID and water ingress.

- The prediction model presented in this work considers only the single degradation mode of PID. Clearly the power degradation of a PV module over time is affected by multiple interacting degradation modes. In general, developing predictive models that take into account the interplay between two or more degradation modes is complex and constitutes a critical task to be accomplished in order to quantify PV module lifetime.

- For a degradation mode independent of PID, instead, our model could be applied as it is and the effect of the other model simply added to the effect of PID. For example, degradation of the electrical interconnections is independent of PID. As mentioned in Chapter 3, a recent study by Nick Bosco *et al.* [12] proposed how to adapt the thermal cycling (TC) test, based on the standard test proposed in IEC 61215, to be climate specific by varying the number and the temperature range of the cycles. If a set of modules is subjected to a combination of TC tests as proposed in [12] specific to the climate of the site chosen for the installation, and in parallel other modules of the same type are subjected to the PID test sequence proposed in this thesis, an estimation of the modules' lifetime that considers these two degradation modes is achieved.

- We observe that, even if some strategies to prevent or mitigate PID in modules using conventional aluminum back surface field (Al-BSF) p-type c-Si solar cells are now well known, given the strong and constant market dynamics to reduce module manufacturing costs, we cannot guarantee that PID is not going to be observed in future field-deployed solar modules or systems. For this, we stress the importance that consistent and reproducible module manufacturing practices, which start with a strict control of the bill of materials, have in preventing the occurrence of PID in the field.

- With regard to new cell technologies, we expect that in PERC cells (passivated emitter and rear cell), where the only differences with respect to standard p-type cells lay in the rear surface, the mechanism of PID is in general the same as for the standard p-type cells considered in this dissertation. We expect therefore that our study of PID mitigation strategies is applicable to PERC cells as well. The mechanism of PID in silicon heterojunction (SHJ) cells is instead very different in that it does not consist of cell shunting but corrosion of the transparent conductive oxide (TCO) layer (similar to thin-film modules) and requires a different study.

- The work carried out in Chapter 7 on interconnection failures focused on the complete rupture of the cell interconnect ribbon. However, more often the increase in module series resistance is caused by defects such as the loss of adhesion between a ribbon and the cell busbar or by resistive solder bonds. The experimental validation of our model is promising and we foresee as a continuation of this work an adaptation of our model to simulate series resistance increase due to these less extreme defects. A further implementation of our model may concern cells with four or five busbars and multiwire interconnection solutions, which are a current trend in the PV industry.

- The continuous evolution in cell technologies and the implementation of new encapsulation materials will lead to the appearance of new degradation modes, which might require years before being detected in the field. The case of the so-called LeTID (light- and elevated temperature-induced degradation) effect that was observed in PERC cells only in 2015 [78] is an example. Also new applications of PV such as building-integrated photovoltaics (BIPV) lead modules to operate in new conditions (resulting *e.g.* in higher module temperature excursions) and employ new materials, which may result in a different evolution of the typical degradation modes as well as in the appearance of new degradation modes.

- PV is increasingly being deployed in regions with extreme climatic conditions: PV plants were installed in the last few years in desert zones in Africa and at high altitudes in South America. In such environments, modules are exposed to harsher stresses, *e.g.* higher doses of ultraviolet radiation or stronger thermal excursions. If modules will continue to be certified by the current qualification standard IEC 61215, which was developed mainly for temperate climates, a good performance in the warranty period is not guaranteed. To conclude, PV module reliability remains a crucial topic in the industry of photovoltaics, and the efforts of the international community towards an improvement of the understanding of module reliability is fundamental to provide meaningful estimations of power performance and to continue to improve module lifetime.

A A mathematical justification of the equivalent time

In the simulations of PID in outdoor conditions in Chapter 5, we apply a method based on the concept of “equivalent time” to overcome the difficulty of applying the empirical equations for PID obtained at indoor (constant) stress conditions to simulate the effect of PID on a PV module installed outdoors (stress conditions that vary in time). Here, we show with a mathematical argument that this method provides indeed a consistent way to describe a phenomenon on a discrete time-interval.

Following the introduction to equivalent time given in Chapter 5.3.3, let us consider a module subjected to accelerated PID test in the laboratory. The stress levels (temperature T, relative humidity RH, and voltage V) are constant in time during the test. In Chapter 4 we observed that the effect of PID on the degradation of the module power at time t in these conditions can be described by Equation (4.3), which we recall:

$$P(t) = P_{\text{ini}} \cdot \left(1 - A \cdot V \cdot RH^B \cdot \exp\left(-\frac{E_a}{\kappa T}\right) \cdot t^2\right) \tag{A.1}$$

In particular, the power evolution is described by a monotonous function defined over a continuous time interval. This equation is then applied in Chapter 5 to simulate the effect of PID in real outdoor conditions. The time interval $[0, t]$ in this case is discrete, divided into n subintervals all of the same length Δt (for our TMY meteorological dataset, $\Delta t = 1$ h):

$$[0, t] = [t_0, t_1, \ldots, t_n] \, .$$

To simplify the discussion, let us assume that the only stress factor that varies in time is temperature, T_i, for $i = 1, ..., n$. For a clearer notation, let us group in Equation (A.1) all the terms that contain the PID stress parameters in one term, $C(T_i)$, which depends on time only through the parameter T_i:

$$C(T_i) := A \cdot V \cdot RH^B \cdot e^{-\frac{Ea}{\kappa \cdot T_i}}$$

A natural choice would be to implement Equation (A.1) in each subinterval in a piecewise manner, *i.e.* applying the equation over a time duration of Δt. However, this type of implementation is not mathematically consistent, whereas the use of the equivalent time provides a solution to the problem. In order to prove this, let us consider the following two situations. (1) The stress levels are constant over the time interval, *i.e.* we are in the case described by Equation (A.1). (2) The stress levels vary infinitesimally at each interval $[t_{i-1}, t_i]$. We expect that the power values at the final time t_n obtained in case (2) are very close to the values obtained in case (1).

1. Constant stress conditions
   Let us suppose $T_i = T_{i-1} =: T$ for each $i = 2, ..., n$, in particular one has $C(T_i) = C(T_1) \forall i = 2, ..., n$. The module power at the time t_i is given by:

   $$\begin{aligned} P(t_i) &= P(t_0) \cdot \left(1 - C(T_1) \cdot t_i^2\right) \\ &= P(t_0) \cdot \left(1 - C(T_1) \cdot (i \cdot \Delta t)^2\right) \end{aligned} \tag{A.2}$$

2. Infinitesimal variations of the stress conditions
   We assume that at every time interval the stress conditions vary infinitesimally with respect to the previous one:

   $$T_i = T_{i-1} + \epsilon \quad \text{for each } i = 1, ..., n \,.$$

   In the following we compare the two types of implementations.

   - **Piecewise approach**
     The power at time t_i is calculated with a piecewise approach as follows.

     $$\begin{aligned} P(t_i) &= P(t_{i-1}) \cdot \left(1 - C(T_i) \cdot (t_i - t_{i-1})^2\right) \\ &= P(t_{i-1}) \cdot \left(1 - C(T_{i-1} + \epsilon) \cdot \Delta t^2\right) \\ &= P(t_{i-2}) \cdot \left(1 - C(T_{i-2} + \epsilon) \cdot \Delta t^2\right) \cdot \left(1 - C(T_{i-1} + \epsilon) \cdot \Delta t^2\right) \\ &= \dots \end{aligned}$$

     For $\epsilon \to 0$ we obtain:

     $$\lim_{\epsilon \to 0} P(t_i) = P(t_0) \cdot \left(1 - C(T_1) \Delta t^2\right)^i \,. \tag{A.3}$$

     We observe that Equation (A.3) represents a different mathematical law respect to the one that describes the power evolution at constant conditions (Equation (A.2)).

This is a contradiction, as we are assuming that the stress conditions tend to be constant.

- **Equivalent time**

  As mentioned in Chapter 5, the equivalent time at time i, denoted by $t_{eq}(i)$, is defined as the time required at temperature T_i to reach the power value $P_{T_{i-1}}(t_{i-1})$.

  We use now this concept to calculate the power at the time t_i, as follows.

  $$\begin{aligned} P(t_i) &= P(t_0)\cdot\left(1-C(T_i)\cdot\left(t_i-t_{i-1}+t_{eq}(T_i,P(t_{i-1}))\right)^2\right) \\ &= P(t_0)\cdot\left(1-C\left(T_{i-1}+\epsilon\right)\cdot\left(t_i-t_{i-1}+t_{eq}(T_{i-1}+\epsilon,P(t_{i-1}))\right)^2\right) \end{aligned} \tag{A.4}$$

  Let us now suppose that $\epsilon \to 0$, i.e. the stress conditions tend to be constant (in particular, $T_i \to T_1$ for each $i = 2, \dots, n$).

  $$\lim_{\epsilon\to 0} t_{eq}(T_{i-1}+\epsilon, P(t_{i-1})) = t_{eq}(T_1, P(t_{i-1})) \tag{A.5}$$

  By definition of equivalent time it follows that:

  $$t_{eq}(T_1, P(t_{i-1})) = t_{i-1}\ .$$

  Therefore Equation (A.4) becomes:

  $$\begin{aligned} \lim_{\epsilon\to 0} P(t_i) &= P(t_0)\cdot\left(1-C(T_1)\,(t_i-t_{i-1}+t_{i-1})^2\right) \\ &= P(t_0)\cdot\left(1-C(T_1)\,(t_i)^2\right) \\ &= P(t_0)\cdot\left(1-C(T_1)\,(i\cdot\Delta t)^2\right) \end{aligned} \tag{A.6}$$

  In this case, when temperature values tend to be constant the power function $P(t)$ (Equation (A.6)) tends to the same mathematical law as in Equation (A.2), as one would expect. We have thus shown that the equivalent time allows thus to “concatenate” equations at different time-steps (having different stress levels) in a consistent way alongside the time line, obtaining a “piece-wise” model that approximates the continuous one.

We can conclude that the equivalent time approach gives a consistent way of implementing an equation obtained at constant stress conditions in a case where the stress conditions vary in time.

As a general remark, we observe that a general definition of the equivalent time for a given degradation mechanism can be given as follows.

Definition A.1. Consider a physical system subjected to a certain time-varying stress $\mathscr{S}(t)$. We want to study a specific property of the system, say $\mathscr{P}$, that changes according to time and to the applied stress. The property $\mathscr{P}$ is then modeled as a function of the form

$$t \mapsto \mathscr{P}(t, \mathscr{S}(t)).$$

Suppose that for every stress $\mathscr{S}$ the functions have the same value in $t = 0$. Suppose that, whenever $\mathscr{S}(t) = \bar{\mathscr{S}}$ is constant in time, the function $t \mapsto \mathscr{P}(t, \bar{\mathscr{S}})$ is continuous and bijective (*i.e.*, injective and surjective). Now fix values $\bar{\mathscr{P}}$ and $\bar{\mathscr{S}}$ for the property $\mathscr{P}$ and the stress level $\mathscr{S}$, respectively. The **equivalent time** associated with $\bar{\mathscr{P}}$ and $\bar{\mathscr{S}}$, denoted by t_{eq}, is the time instant such that:

$$\mathscr{P}(\bar{\mathscr{S}}, t_{\text{eq}}) = \bar{\mathscr{P}}.$$

In other words, t_{eq} is the time instant at which the property $\mathscr{P}$ reaches the value $\bar{\mathscr{P}}$ at constant stress conditions $\bar{\mathscr{S}}$.

Observe that the continuity and the surjectivity of the functions are needed to guarantee the existence of t_{eq}; the injectivity to assure its uniqueness.

Bibliography

[1] L. Adelard, F. Pignolet-Tardan, T. Mara, P. Lauret, F. Garde, and H. Boyer, *Sky temperature modelisation and applications in building simulation*, Renewable Energy, 15 (1998), pp. 418–430.

[2] E. Annigoni, M. Jankovec, F. Galliano, H. Y. Li, L.-E. Perret-Aebi, M. Topič, F. Sculati-Meillaud, A. Virtuani, and C. Ballif, *Modeling potential-induced degradation (PID) in crystalline silicon solar cells: from accelerated-aging laboratory testing to outdoor prediction*, Proc. 32nd EUPVSEC, (2016), pp. 1558–1563.

[3] E. Annigoni, A. Virtuani, J. Levrat, A. Faes, F. Sculati-Meillaud, M. Despeisse, and C. Ballif, *Quantifying and modeling the impact of interconnection failures on the electrical performance of crystalline silicon photovoltaic modules, Submitted to Progress in Photovoltaics: Research and Applications.*

[4] E. Annigoni, A. Virtuani, F. Sculati-Meillaud, and C. Ballif, *Modeling potential-induced degradation (PID) of field-exposed crystalline silicon solar PV modules: Focus on a regeneration term*, in Photovoltaic Specialists Conference (PVSC), 2017 44th IEEE, IEEE, 2017.

[5] J. L. Austbø, *Preventing and modelling of potential-induced degradation in crystalline silicon PV modules*, Master thesis, Hanze University of Applied Sciences jointly with Ecole Polytechnique Fédérale de Lausanne.

[6] J. Bauer, V. Naumann, S. Grosser, C. Hagendorf, M. Schütze, and O. Breitenstein, *On the mechanism of potential-induced degradation in crystalline silicon solar cells*, Physica Status Solidi (RRL) Rapid Research Letters, 6 (2012), pp. 331–333.

[7] J. Belmont, K. Olakonu, J. Kuitche, and G. TamizhMani, *Degradation rate evaluation of 26-year-old 200 kw power plant in a hot-dry desert climate*, in Photovoltaic Specialist Conference (PVSC), 2014 IEEE 40th, IEEE, 2014, pp. 3162–3166.

[8] J. Berghold, S. Koch, A. Böttcher, A. Ukar, M. Leers, and P. Grunow, *Potential-induced degradation (PID) and its correlation with experience in the field*, Photovoltaics International, 19 (2013), pp. 85–92.

[9] J. BERGHOLD, S. KOCH, B. FROHMANN, P. HACKE, AND P. GRUNOW, *Properties of encapsulation materials and their relevance for recent field failures*, in Photovoltaic Specialist Conference (PVSC), 2014 IEEE 40th, IEEE, 2014, pp. 1987–1992.

[10] J. BERGHOLD, S. KOCHA, S. PINGELB, S. JANKEB, A. UKARA, P. GRUNOWA, AND T. SHIODAC, *PID: From material properties to outdoor performance and quality control counter measures*, in Proc. of SPIE Vol, vol. 9563, 2015, pp. 95630A–1.

[11] Z. BOKSAY, M. VARGA, AND A. WIKBY, *Surface conductivity of leached glass*, Journal of Non-Crystalline Solids, 17 (1975), pp. 349–358.

[12] N. BOSCO, T. J. SILVERMAN, AND S. KURTZ, *Climate specific thermomechanical fatigue of flat plate photovoltaic module solder joints*, Microelectronics Reliability, 62 (2016), pp. 124–129.

[13] S. BOWDEN AND A. ROHATGI, *Rapid and accurate determination of series resistance and fill factor losses in industrial silicon solar cells*, Georgia Institute of Technology, 2001.

[14] B. BRAISAZ, B. COMMAULT, N. LE QUANG, E. GERRISTEN, M. JOANNY, D. BINESTI, G. GOAER, AND K. RADOUANE, *Improved 1500V PID resistance: encapsulant, cover glass and ion implanted cells*, in Proceedings of the 32nd European PVSEC, 2016, pp. 1874–1878.

[15] B. BRAISAZ, C. DUCHAYNE, M. VAN ISEGHEM, AND K. RADOUANE, *PV aging model applied to several meteorological conditions*, in Proceedings of the 29th European PVSEC, 2014, pp. 2303–2309.

[16] T. CARLSSON, J. HALME, P. LUND, AND P. KONTTINEN, *Moisture sensor at glass/polymer interface for monitoring of photovoltaic module encapsulants*, Sensors and Actuators A, 125 (2006), pp. 281–287.

[17] N. CHEN AND A. EBONG, *Towards 20% efficient industrial al-bsf silicon solar cell with multiple busbars and fine gridlines*, Solar Energy Materials and Solar Cells, 146 (2016), pp. 107–113.

[18] E. COLLINS, M. DVORACK, J. MAHN, M. MUNDT, AND M. QUINTANA, *Reliability and availability analysis of a fielded photovoltaic system*, in Proceedings of the 34th IEEE Photovoltaic Specialists Conference, 2009.

[19] D. J. COYLE, *Life prediction for cigs solar modules part 1: modeling moisture ingress and degradation*, Progress in Photovoltaics: Research and Applications, 21 (2013), pp. 156–172.

[20] J. CRANK, *The Mathematics of Diffusion: 2d Ed*, Clarendon Press, 1975.

[21] A. CZANDERNA AND F. PERN, *Encapsulation of PV modules using ethylene vinyl acetate copolymer as a pottant: A critical review*, Solar energy materials and solar cells, 43 (1996), pp. 101–181.

[22] D. DeGraaff, R. Lacerda, and Z. Campeau, *Degradation mechanisms in si module technologies observed in the field; their analysis and statistics*, in NREL 2011 Photovoltaic Module Reliability Workshop, 2011.

[23] J. A. Del Cueto and T. J. McMahon, *Analysis of leakage currents in photovoltaic modules under high-voltage bias in the field*, Progress in Photovoltaics: Research and Applications, 10 (2002), pp. 15–28.

[24] R. Dubey, S. Chattopadhyay, V. Kuthanazhi, J. J. John, B. Arora, A. Kottantharayil, K. Narasimhan, C. Solanki, V. Kuber, J. Vasi, et al., *All india survey of photovoltaic module degradation 2013*, National Centre for Photovoltaic Research and Education, Mumbai, India, (2014).

[25] O. Dupré, R. Vaillon, and M. A. Green, *Thermal behavior of photovoltaic devices: physics and engineering*, Springer, 2016.

[26] U. Eitner, *Thermomechanics of photovoltaic modules*, PhD thesis, Halle (Saale), Martin-Luther-Universität Halle-Wittenberg, Diss., 2011, 2011.

[27] L. A. Escobar and W. Q. Meeker, *A review of accelerated test models*, Statistical science, (2006), pp. 552–577.

[28] A. Faes, M. Despeisse, J. Levrat, J. Champliaud, N. Badel, M. Kiaee, T. Söderström, Y. Yao, R. Grischke, M. Gragert, et al., *Smartwire solar cell interconnection technology*, in Proc. 29th Eur. Photovoltaic Sol. Energy Conf, 2014, pp. 2555–2561.

[29] T. Friesen, D. Chianese, A. Realini, G. Friesen, E. Burà, A. Virtuani, D. Strepparava, and R. Meoli, *TISO 10 kw: 30 years experience with a PV plant*, in Proceedings of the 27th European Photovoltaic Solar Energy Conference, 2012, pp. 3125–3131.

[30] A. Gabor, R. Janoch, A. Anselmo, and H. Field, *Solar panel design factors to reduce the impact of cracked cells and the tendency for crack propagation*, in NREL PV Module Reliability Workshop, Denver, USA, 2015.

[31] A. Gabor, R. Janoch, A. Anselmo, and H. Field, *Solar panel design factors to reduce the impact of cracked cells and the tendency for crack propagation*, in NREL PV Module Reliability Workshop, Denver, CO (USA), 2015.

[32] A. Geraci, F. Katki, L. McMonegal, B. Meyer, J. Lane, P. Wilson, J. Radatz, M. Yee, H. Porteous, and F. Springsteel, *IEEE standard computer dictionary: Compilation of IEEE standard computer glossaries*, IEEE Press, 1991.

[33] P. Hacke, M. Kempe, K. Terwilliger, S. Glick, N. Call, S. Johnston, and S. Kurtz, *Characterization of multicrystalline silicon modules with system bias voltage applied in damp heat*, in Proceedings of the 25th European PVSEC, 2010, pp. 3760–3765.

[34] P. Hacke, R. Smith, S. Kurtz, D. Jordan, and J. Wohlgemuth, *Modeling current transfer from PV modules based on meteorological data*, in Photovoltaic Specialists Conference (PVSC), 2016 IEEE 43rd, IEEE, 2016, pp. 1083–1089.

[35] P. Hacke, R. Smith, K. Terwilliger, S. Glick, D. Jordan, S. Johnston, M. Kempe, and S. Kurtz, *Testing and analysis for lifetime prediction of crystalline silicon PV modules undergoing degradation by system voltage stress*, in Photovoltaic Specialists Conference (PVSC), Volume 2, 2012 IEEE 38th, IEEE, 2012, pp. 1–8.

[36] P. Hacke, R. Smith, K. Terwilliger, G. Perrin, B. Sekulic, and S. Kurtz, *Development of an IEC test for crystalline silicon modules to qualify their resistance to system voltage stress*, Progress in Photovoltaics: Research and Applications, 22 (2014), pp. 775–783.

[37] P. Hacke, S. Spataru, K. Terwilliger, G. Perrin, S. Glick, S. Kurtz, and J. Wohlgemuth, *Accelerated testing and modeling of potential-induced degradation as a function of temperature and relative humidity*, IEEE Journal of Photovoltaics, 5 (2015), pp. 1549–1553.

[38] P. Hacke, K. Terwilliger, S. Glick, R. Smith, G. Perrin, S. Kurtz, N. Bosco, and J. Wohlgemuth, *Application of the terrestrial photovoltaic module accelerated test-to-failure protocol*, in Photovoltaic Specialist Conference (PVSC), 2014 IEEE 40th, IEEE, 2014, pp. 0930–0936.

[39] P. Hacke, K. Terwilliger, S. Glick, D. Trudell, N. Bosco, S. Johnston, and S. Kurtz, *Test-to-failure of crystalline silicon modules*, in Photovoltaic Specialists Conference (PVSC), 2010 35th IEEE, IEEE, 2010, pp. 000244–000250.

[40] P. Hacke, K. Terwilliger, R. Smith, S. Glick, J. Pankow, M. Kempe, S. K. I. Bennett, and M. Kloos, *System voltage potential-induced degradation mechanisms in PV modules and methods for test*, in 37th IEEE Photovoltaic Specialists Conference, 2011, pp. 000814–000820.

[41] W. Han, W. Shan, S. Liu, W. Li, X. Niu, J. Jin, C. Li, and Q. Zhai, *Ion implantation-an effective solution to prevent c-si PV module PID*, in Proc. 28th Eur. Photovoltaic Sol. Energy Conf. Exhib, 2013, pp. 3309–3312.

[42] A. L. Hartzell, M. G. Da Silva, and H. R. Shea, *MEMS reliability*, Springer Science & Business Media, 2010.

[43] S. P. Harvey, J. A. Aguiar, P. Hacke, H. Guthrey, S. Johnston, and M. Al-Jassim, *Sodium accumulation at potential-induced degradation shunted areas in polycrystalline silicon modules*, IEEE Journal of Photovoltaics, 6 (2016), pp. 1440–1445.

[44] J. Hattendorf, W. M. Gnehr, R. Löw, R. Roth, D. Kosnisharov, and M. Zentgraf, *Potential-induced degradation and temperature-driven regeneration: a realistic simulation*, in Proceedings of the 28th European PVSEC, 2013, pp. 3303–3308.

[45] J. Hattendorf, R. Loew, W. M. Gnehr, L. Wulff, M. C. Koekten, D. Koshnicharov, A. Blauaermel, and J. A. Esquivel, *Potential induced degradation in mono-crystalline silicon based modules: an acceleration model*, in Proceedings of the 27th European PVSEC, 2012, pp. 3405–3410.

[46] W. Herrmann and N. Bogdanski, *Outdoor weathering of PV modules—effects of various climates and comparison with accelerated laboratory testing*, in Photovoltaic Specialists Conference (PVSC), 2011 37th IEEE, IEEE, 2011, pp. 002305–002311.

[47] C. Hinz, S. Koch, T. Weber, and J. Berghold, *Regeneration of potential-induced degradation affected modules*, in Proceedings of 32nd European Photovoltaic Solar Energy Conference and Exhibition, Munich, Germany, 2016, pp. 1552–1557.

[48] C. Hirschl, M. Biebl-Rydlo, M. DeBiasio, W. Mühleisen, L. Neumaier, W. Scherf, G. Oreski, G. Eder, B. Chernev, W. Schwab, and M. Kraft, *Determining the degree of crosslinking of ethylene vinyl acetate photovoltaic module encapsulants – a comparative study*, Solar Energy Materials and Solar Cells, 116 (2013), pp. 203–218.

[49] P. Hülsmann, M. Heck, and M. Köhl, *Simulation of water vapor ingress into PV-modules under different climatic conditions*, Journal of Materials, 2013 (2013).

[50] S. Hoffmann and M. Koehl, *Effect of humidity and temperature on the potential-induced degradation*, Progress in Photovoltaics: Research and Applications, 22 (2014), pp. 173–179.

[51] IEA, *Review of failures of photovoltaic modules*, Tech. Report IEA-PVPS T13-01:2014, IEA International Energy Agency, 2014.

[52] IEA, *Assessment of photovoltaic module failures in the field*, Tech. Report IEA-PVPS T13-09:2017, IEA International Energy Agency, 2017.

[53] IEA, *Trends 2017 in photovoltaic applications – Survey report of selected IEA countries between 1992 and 2016*, Tech. Report IEA-PVPS T13-09:2017, IEA International Energy Agency, 2017.

[54] IEC 60050 (191), *International Electrotechnical Vocabulary, Chapter 191: Dependability and quality of service*, International Electrotechnical Commission, (1990).

[55] IEC 60904-3:2016, *Photovoltaic devices – Part 3: Measurement principles for terrestrial photovoltaic (PV) solar devices with reference spectral irradiance data*, International Electrotechnical Commission, (2016).

[56] IEC 61215, *Terrestrial photovoltaic (PV) modules – Design qualification and type approval*, International Electrotechnical Commission, (2016).

[57] IEC 62788-1-2, *Measurement procedures for materials used in photovoltaic modules – part 1-2: Encapsulants – measurement of volume resistivity of photovoltaic encapsulants and other polymeric materials*, International Electrotechnical Commission, (2016).

[58] IEC 62788-1-2:2016, *Measurement procedures for materials used in photovoltaic modules - Part 1-2: Encapsulants - Measurement of volume resistivity of photovoltaic encapsulants and other polymeric materials*, International Electrotechnical Commission, (2016).

[59] IEC 62804-1:2015, *Photovoltaic (PV) modules - Test methods for the detection of potential-induced degradation - Part 1: Crystalline silicon*, International Electrotechnical Commission, (2015).

[60] ILUMEN, *https://www.ilumen.be/en/all-products/pidbox/*, 2018. [Online; accessed 10-May-2018].

[61] IW GROUP AND OTHERS, *International Technology Roadmap for Photovoltaic (ITRPV) 2017 Results*, SEMI, Berlin, Germany, (2017).

[62] H. J., R. LOEW, W.-M. GNEHR, L. WULFF, M. C. KOEKTEN, D. KOSHNICHAROV, A. BLAUAERMEL, AND A. ESQUIVEL, *Potential induced degradation in mono-crystalline silicon based modules: an acceleration model*, in Proceedings of the 27th European PVSEC, 2012.

[63] M. JANKOVEC, F. GALLIANO, E. ANNIGONI, H. Y. LI, F. SCULATI-MEILLAUD, L.-E. PERRET-AEBI, C. BALLIF, AND M. TOPIČ, *In-situ monitoring of moisture ingress in PV modules using digital humidity sensors*, IEEE Journal of Photovoltaics, 6 (2016), pp. 1152–1159.

[64] A. JONES AND C. UNDERWOOD, *A thermal model for photovoltaic systems*, Solar energy, 70 (2001), pp. 349–359.

[65] D. C. JORDAN AND S. R. KURTZ, *Photovoltaic degradation rates – an analytical review*, Progress in photovoltaics: Research and Applications, 21 (2013), pp. 12–29.

[66] D. C. JORDAN, S. R. KURTZ, K. VANSANT, AND J. NEWMILLER, *Compendium of photovoltaic degradation rates*, Progress in Photovoltaics: Research and Applications, 24 (2016), pp. 978–989.

[67] D. C. JORDAN, T. J. SILVERMAN, B. SEKULIC, AND S. R. KURTZ, *PV degradation curves: non-linearities and failure modes*, Progress in Photovoltaics: Research and Applications, 25 (2017), pp. 583–591.

[68] D. C. JORDAN, T. J. SILVERMAN, J. H. WOHLGEMUTH, S. R. KURTZ, AND K. T. VANSANT, *Photovoltaic failure and degradation modes*, Progress in Photovoltaics: Research and Applications, 25 (2017), pp. 318–326.

[69] M. KAMBE, K. HARA, K. MITARAI, S. TAKEDA, M. FUKAWA, N. ISHIMARU, AND M. KONDO, *Chemically strengthened cover glass for preventing potential induced degradation of crystalline silicon solar cells*, in Photovoltaic Specialists Conference (PVSC), 2013 IEEE 39th, IEEE, 2013, pp. 3500–3503.

[70] J. Kapur, A. Bennett, J. Norwood, B. Hamzavytehrany, and I. Kueppenbender, *Tailoring ionomer encapsulants as a low cost solution to potential induced degradation*, in Proc. 28th Eur. Photovoltaic Solar Energy Conf., 2013, pp. 476–479.

[71] K. Kato, *Pvressq!: a research activity on reliability of PV systems from an user's viewpoint in japan*, in Reliability of Photovoltaic Cells, Modules, Components, and Systems IV, vol. 8112, International Society for Optics and Photonics, 2011, p. 81120K.

[72] D. Kececioglu, *Reliability engineering handbook*, vol. 1, DEStech Publications, Inc, 2002.

[73] M. D. Kempe, *Modeling of rates of moisture ingress into photovoltaic modules*, Solar Energy Materials and Solar Cells, 90 (2006), pp. 2720–2738.

[74] M. D. Kempe, A. A. Dameron, and M. O. Reese, *Evaluation of moisture ingress from the perimeter of photovoltaic modules*, Progress in Photovoltaics: Research and Applications, 22 (2014), pp. 1159–1171.

[75] M. D. Kempe, D. C. Millera, D. L. Noblesa, K. Sakuraib, J. Tuckerc, J. G. Bokriad, T. Shiodae, K. Nanjundiahf, T. Yoshiharag, J. Birchmierg, O. Zubillagah, and J. H. Wohlgemuth, *Development of a resistivity standard for polymeric materials used in photovoltaic modules*, in Proceedings of SPIE, vol. 9563, 956302, 2015.

[76] M. D. Kempe, D. Panchagade, M. O. Reese, and A. A. Dameron, *Modeling moisture ingress through polyisobutylene-based edge-seals*, Progress in Photovoltaics: Research and Applications, 23 (2015), pp. 570–581.

[77] M. D. Kempe and J. H. Wohlgemuth, *Evaluation of temperature and humidity on PV module component degradation*, in Photovoltaic Specialists Conference (PVSC), 2013 IEEE 39th, IEEE, 2013, pp. 0120–0125.

[78] F. Kersten, P. Engelhart, H.-C. Ploigt, A. Stekolnikov, T. Lindner, F. Stenzel, M. Bartzsch, A. Szpeth, K. Petter, J. Heitmann, et al., *Degradation of multicrystalline silicon solar cells and modules after illumination at elevated temperature*, Solar Energy Materials and Solar Cells, 142 (2015), pp. 83–86.

[79] N. Kim and C. Han, *Experimental characterization and simulation of water vapor diffusion through various encapsulants used in PV modules*, Solar Energy Materials and Solar Cells, 116 (2013), pp. 68–75.

[80] G.-A. Klutke, P. C. Kiessler, and M. A. Wortman, *A critical look at the bathtub curve*, IEEE Transactions on Reliability, 52 (2003), pp. 125–129.

[81] S. Koch, J. Berghold, B. Abdullah, C. Hinz, and P. Grunow, *Prediction model for potential induced degradation effects on crystalline silicon cells*, in Proceedings of the 29th European PVSEC, 2014.

[82] S. Koch, J. Berghold, C. Hinz, S. Krauter, and P. Grunow, *Improvement of a prediction model for potential induced degradation by better understanding the regeneration mechanism*, in Proceedings of the 31st European PVSEC, 2015.

[83] S. Koch, D. Nieschalk, J. Berghold, S. Wendlandt, S. Krauter, and P. Grunow, *Potential induced degradation effects on crystalline silicon cells with various antireflective coatings*, Proceedings of 27th EUPVSEC, Frankfurt, Germany, (2012), pp. 1985–1990.

[84] S. Koch, C. Seidel, P. Grunow, S. Krauter, and M. Schoppa, *Polarization effects and tests for crystalline silicon cells*, in 26th European photovoltaic solar energy conference and exhibition, Hamburg, Germany, 2011, pp. 1726–1731.

[85] M. Koehl, M. Heck, and S. Wiesmeier, *Modelling of conditions for accelerated lifetime testing of humidity impact on PV-modules based on monitoring of climatic data*, Solar energy materials and solar cells, 99 (2012), pp. 282–291.

[86] J. A. Kratochvil, W. E. Boyson, and D. L. King, *Photovoltaic array performance model*, tech. report, Sandia National Laboratories, 2004.

[87] S. Kurtz, I. L. Repins, P. L. Hacke, D. Jordan, and M. D. Kempe, *Qualification testing versus quantitative reliability testing of PV-gaining confidence in a rapidly changing technology*, tech. report, 2017.

[88] S. Kurtz, J. Wohlgemuth, M. Yamamichi, T. Sample, D. Miller, D. Meakin, C. Monokroussos, M. TamizhMani, M. Kempe, D. Jordan, N. Bosco, P. Hacke, V. Bermudez, and M. Kondo, *A framework for a comparative accelerated testing standard for PV modules*, in Proceedings of the 39th IEEE Photovoltaic Specialists Conference, 2013.

[89] B. Lalaguna, P. Sánchez-Friera, F. Ropero, J. F. Gil, and J. Alonso, *Comparison of moisture ingress in PV modules with different backsheets using humidity sensors*, in Proceedings of the 23th European PVSEC, 2008.

[90] D. Lausch, V. Naumann, O. Breitenstein, J. Bauer, A. Graff, J. Bagdahn, and C. Hagendorf, *Potential-induced degradation (PID): Introduction of a novel test approach and explanation of increased depletion region recombination*, IEEE Journal of Photovoltaics, 4 (2014), pp. 834–840.

[91] D. Lausch, V. Naumann, A. Graff, A. Hähnel, O. Breitenstein, C. Hagendorf, and J. Bagdahn, *Sodium outdiffusion from stacking faults as root cause for the recovery process of potential-induced degradation (PID)*, Energy Procedia, 55 (2014), pp. 486–493.

[92] D. Lausch, K. Petter, R. Bakowskie, J. Bauer, O. Breitenstein, and C. Hagendorf, *Classification and investigation of recombination-active defect structures in multicrystalline silicon solar cells*, in Proceedings of the 27th European PVSEC, 2012.

[93] P. Lechner, S. Hummel, and J. Schnepf, *Evaluation of recovery methods after potential induced degradation of PV modules*, in Proceedings of the 31st European PVSEC, 2015.

[94] Y. Lee, M. Tsai, K. Lu, W. Yang, S. Chen, M. Lin, H. Sung, and H. Wu, *Potential induced degradation experiments on different encapsulated silicon mini solar modules*, in Proc. 29th Eur. Photovolt. Sol. Energy Conf. Exhib, 2014.

[95] H. Li, *Open the Black Box: Understanding the Encapsulation Process of Photovoltaic Modules*, PhD thesis, Ecole Polytechnique Fédérale de Lausanne, 2013.

[96] M. López-Escalante, L. J. Caballero, F. Martín, M. Gabás, A. Cuevas, and J. Ramos-Barrado, *Polyolefin as PID-resistant encapsulant material in PV modules*, Solar Energy Materials and Solar Cells, 144 (2016), pp. 691–699.

[97] W. Luo, Y. S. Khoo, P. Hacke, V. Naumann, D. Lausch, S. P. Harvey, J. P. Singh, J. Chai, Y. Wang, A. G. Aberle, and S. Ramakrishna, *Potential-induced degradation in photovoltaic modules: a critical review*, Energy & Environmental Science, 10 (2017), pp. 43–68.

[98] A. Luque and S. Hegedus, *Handbook of photovoltaic science and engineering*, John Wiley & Sons, 2011.

[99] Z. Ma and A. W. Krings, *Competing risks analysis of reliability, survivability, and prognostics and health management (phm)*, in Aerospace Conference, 2008 IEEE, IEEE, 2008, pp. 1–21.

[100] R. Malachi, S. Schœnberger, J. Mayer, and M. Kasemann, *Techno-economic analysis of utility scale PV power plants with up to +/-1500VDC*, in 29th European photovoltaic solar energy conference and exhibition, Amsterdam, The Netherlands, 2014, pp. 2323–2326.

[101] W. Q. Meeker and L. A. Escobar, *Pitfalls of accelerated testing*, IEEE Transactions on Reliability, 47 (1998), pp. 114–118.

[102] R. Meier, F. Kraemer, S. Wiese, K.-J. Wolter, and J. Bagdahn, *Reliability of copper-ribbons in photovoltaic modules under thermo-mechanical loading*, in Photovoltaic Specialists Conference (PVSC), 2010 35th IEEE, IEEE, 2010, pp. 001283–001288.

[103] R. Meitzner and S.-H. Schulze, *Method for determination of parameters for moisture simulations in photovoltaic modules and laminated glass*, Solar Energy Materials and Solar Cells, 144 (2016), pp. 23–28.

[104] D. C. Miller, E. Annigoni, A. Ballion, J. G. Bokria, L. S. Bruckman, D. M. Burns, X. Chen, J. Feng, R. H. French, S. Fowler, et al., *Degradation in PV encapsulant strength of attachment: An interlaboratory study towards a climate-specific test*, in Photovoltaic Specialists Conference (PVSC), 2016 IEEE 43rd, IEEE, 2016, pp. 0095–0100.

[105] G. MON, L. WEN, R. ROSS, AND D. ADENT, *Effects of temperature and moisture on module leakage currents*, in 18th IEEE PVSC, 1985, pp. 1179–1185.

[106] H. MÜLLEJANS, W. ZAAIMAN, AND R. GALLEANO, *Analysis and mitigation of measurement uncertainties in the traceability chain for the calibration of photovoltaic devices*, Measurement Science and Technology, 20 (2009), p. 075101.

[107] J. MUÑOZ, E. LORENZO, F. MARTÍNEZ-MORENO, L. MARROYO, AND M. GARCÍA, *An investigation into hot-spots in two large grid-connected PV plants*, Progress in Photovoltaics: Research and applications, 16 (2008), pp. 693–701.

[108] D. R. MYERS, *Predicting temperatures of exposure panels: models and empirical data*, ACS Publications, 1999.

[109] H. NAGEL, R. PFEIFFER, A. RAYKOV, AND K. WANGEMANN, *Lifetime warranty testing of crystalline silicon modules for potential-induced degradation*, 27th EUPVSEC, (2012), pp. 3163–3166.

[110] V. NAUMANN, C. BRZUSKA, M. WERNER, S. GROSSER, AND C. HAGENDORF, *Investigations on the formation of stacking fault-like PID-shunts*, (2016).

[111] V. NAUMANN, C. HAGENDORF, S. GROSSER, M. WERNER, AND J. BAGDAHN, *Micro structural root cause analysis of potential induced degradation in c-si solar cells*, Energy Procedia, 27 (2012), pp. 1–6.

[112] V. NAUMANN, K. ILSE, AND C. HAGENDORF, *On the discrepancy between leakage currents and potential-induced degradation of crystalline silicon modules*, in Proceedings of 28th European Photovoltaic Solar Energy Conference and Exhibition, Paris, France, 2013, pp. 2994–2997.

[113] V. NAUMANN, D. LAUSCH, A. GRAFF, M. WERNER, S. SWATEK, J. BAUER, A. HÄHNEL, O. BREITENSTEIN, S. GROSSER, J. BAGDAHN, AND C. HAGENDORF, *The role of stacking faults for the formation of shunts during potential-induced degradation of crystalline si solar cells*, Physica Status Solidi RRL, 7 (2013), pp. 315–318.

[114] V. NAUMANN, D. LAUSCH, AND C. HAGENDORF, *Sodium decoration of pid-s crystal defects after corona induced degradation of bare silicon solar cells*, Energy procedia, 77 (2015), pp. 397–401.

[115] V. NAUMANN, D. LAUSCH, A. HÄHNEL, J. BAUER, O. BREITENSTEIN, A. GRAFF, M. WERNER, S. SWATEK, S. GROSSER, J. BAGDAHN, ET AL., *Explanation of potential-induced degradation of the shunting type by na decoration of stacking faults in si solar cells*, Solar Energy Materials and Solar Cells, 120 (2014), pp. 383–389.

[116] W. B. NELSON, *Accelerated testing: statistical models, test plans, and data analysis*, vol. 344, John Wiley & Sons, 2009.

[117] P. O'CONNOR AND A. KLEYNER, *Practical reliability engineering*, John Wiley & Sons, 2012.

[118] J. OH, S. BOWDEN, AND G. TAMIZHMANI, *Potential-induced degradation (PID): Incomplete recovery of shunt resistance and quantum efficiency losses*, IEEE Journal of Photovoltaics, 5 (2015), pp. 1540–1548.

[119] G. ORESKI, A. MIHALJEVIC, Y. VORONKO, AND G. C. EDER, *Acetic acid permeation through photovoltaic backsheets: Influence of the composition on the permeation rate*, Polymer Testing, 60 (2017), pp. 374–380.

[120] C. OSTERWALD, J. PRUETT, S. RUMMEL, A. ANDERBERG, AND L. OTTOSON, *Forward-biased thermal cycling: a new module qualification test*, tech. report, National Renewable Energy Laboratory (NREL), Golden, CO, USA, 2000.

[121] M. PANDER, S. DIETRICH, R. MEIER, AND M. EBERT, *Fatigue analysis of solar cell interconnectors due to cyclic mechanical loading*, in Proceedings of 32nd European photovoltaic solar energy conference and exhibition, Munich, Germany, 2016, pp. 1589–1597.

[122] M. PANDER, R. MEIER, M. SANDER, S. DIETRICH, AND M. EBERT, *Lifetime estimation for solar cell interconnectors*, in Proceedings of 28th European photovoltaic solar energy conference and exhibition, 2013, pp. 2851–2857.

[123] O. O. PARISH AND T. W. PUTNAM, *Equations for the determination of humidity from dewpoint and psychrometric data*, (1977).

[124] D. S. PECK, *Comprehensive model for humidity testing correlation*, in Reliability Physics Symposium, 1986. 24th Annual, IEEE, 1986, pp. 44–50.

[125] F. J. PERN, *Factors that affect the EVA encapsulant discoloration rate upon accelerated exposure*, Solar energy materials and solar cells, 41 (1996), pp. 587–615.

[126] ———, *Ethylene-vinyl acetate (EVA) encapsulants for photovoltaic modules: Degradation and discoloration mechanisms and formulation modifications for improved photostability*, Macromolecular Materials and Engineering, 252 (1997), pp. 195–216.

[127] F. J. PERN AND A. W. CZANDERNA, *EVA degradation mechanisms simulating those in PV modules*, in AIP Conference Proceedings, vol. 268, 1992, pp. 445–452.

[128] PIDBULL, *http://pidbull.com/product/*, 2018. [Online; accessed 10-May-2018].

[129] S. PINGEL, O. FRANK, M. WINKLER, S. DARYAN, T. GEIPEL, H. HOEHNE, AND J. BERGHOLD, *Potential induced degradation of solar cells and panels*, in Proceedings of the 35th IEEE Photovoltaic Specialists Conference, 2010.

[130] S. PINGEL, S. JANKE, AND O. FRANK, *Recovery methods for modules affected by potential induced degradation (PID)*, in 27th European Photovoltaic Solar Energy Conference and Exhibition (Frankfurt), 2012, pp. 3379–3383.

[131] S. PINGEL, S. JANKE, J. SEYDEWITZ, R. ALAM, S. KOCH, J. KUPKE, AND J. BERGHOLD, *The local potential distribution as driver of PID & "Live PID Monitoring" method*, in Proceedings of the 29th European PVSEC, 2014.

[132] S. PINGEL, D. KOSHNICHAROV, O. FRANK, T. GEIPEL, Y. ZEMEN, B. STRINER, AND J. BERGHOLD, *Initial degradation of industrial silicon solar cells in solar panels*, in Proceedings of the 25th European PVSEC, 2010.

[133] J. L. PLAWSKY, *Transport Phenomena Fundamentals, Third Edition*, CRC Press, 2014.

[134] M. POLISKIE, *Solar Module Packaging: Polymeric Requirements and Selection*, CRC Press, 2016.

[135] S. C. POP, R. SCHULZE, X. WANG, B. YUAN, J. KAPUR, K. STIKA, C. WESTPHAL, H. ANTONIADIS, AND A. MEISEL, *Ionomer-based PID-resistant encapsulant for PV modules*, in Proceedings of the 29th European PVSEC, 2014.

[136] A. RAYKOV, H. NAGEL, D. AMANKWAH, AND W. BERGHOLZ, *Climate model for potential-induced degradation of crystalline silicon photovoltaic modules*, in Proceedings of the 27th European PVSEC, 2012.

[137] A. REALINI, E. BURA, N. CEREGHETTI, D. CHIANESE, S. REZZONICO, T. SAMPLE, AND H. OSSENBRINK, *Study of a 20-year old PV plant (MTBF project)*, in Proc. 17th European Photovoltaic Solar Energy Conference, 2001, pp. 447–450.

[138] REN21, *Renewables 2017 global status report*, (2017).

[139] B. RIMEZ, H. RAHIER, G. VAN ASSCHE, T. ARTOOS, M. BIESEMANS, AND B. VAN MELE, *The thermal degradation of poly (vinyl acetate) and poly (ethylene-co-vinyl acetate), part i: Experimental study of the degradation mechanism*, Polymer Degradation and Stability, 93 (2008), pp. 800–810.

[140] S.-H. SCHULZE, A. APEL, R. MEITZNER, M. SCHAK, C. EHRICH, AND J. SCHNEIDER, *Influence of polymer properties on potential induced degradation of PV-modules*, in 28th European Photovoltaic Solar Energy Conference, 2013.

[141] A. SKOCZEK, T. SAMPLE, AND E. D. DUNLOP, *The results of performance measurements of field-aged crystalline silicon photovoltaic modules*, Progress in Photovoltaics: Research and Applications, 17 (2009), pp. 227–240.

[142] T. SÖDERSTRÖM, P. PAPET, AND J. UFHEIL, *Smart wire connection technology*, in the 28th European Photovoltaic Solar Energy Conference, 2013, pp. 495–499.

[143] G. STOLLWERCK, W. SCHOEPPEL, A. GRAICHEN, AND C. JAEGER, *Polyolefin backsheet and new encapsulant supress cell degradation in the module*, in Proc. 28th Eur. Photovoltaic Solar Energy Conf. Exhib., 2013, pp. 3318–3320.

[144] R. Swanson, M. Cudzinovic, D. DeCeuster, V. Desai, J. Jürgens, N. Kaminar, W. Mulligan, L. Rodrigues-Barbarosa, D. Rose, D. Smith, et al., *The surface polarization effect in high-efficiency silicon solar cells*, in 15th PVSEC, Shanghai, China, 2005.

[145] D. M. Tanner, N. F. Smith, L. W. Irwin, W. P. Eaton, K. S. Helgesen, J. J. Clement, W. M. Miller, J. A. Walraven, K. A. Peterson, P. Tangyunyong, M. T. Dugger, and S. L. Miller, *Mems reliability: infrastructure, test structures, experiments, and failure modes*, tech. report, Sandia National Labs., Albuquerque, NM (US); Sandia National Labs., Livermore, CA (US), 2000.

[146] C. Taubitz, M. Schütze, M. Kröber, and M. B. Koentopp, *Potential induced degradation: Model calculations and correlation between laboratory tests and outdoor occurrence*, in Proc. 29th Eur. Photovoltaic Sol. Energy Conf. Exhib., 2014, pp. 2490–2494.

[147] M. Tencer, *Moisture ingress into nonhermetic enclosures and packages. a quasi-steady state model for diffusion and attenuation of ambient humidity variations*, in Proceedings of the 44th IEEE Electronic Components and Technology Conference, 1994, pp. 196–209.

[148] A. R. Tenner and I. J. Detoro, *Total Quality Management: Three Steps to Continuous Improvement*, Addison-Wesley, 1994.

[149] H. Tian, F. Mancilla-David, K. Ellis, E. Muljadi, and P. Jenkins, *A cell-to-module-to-array detailed model for photovoltaic panels*, Solar energy, 86 (2012), pp. 2695–2706.

[150] C. Tjengdrawira and M. Richter, *Review and gap analyses of technical assumptions in PV electricity cost–report on current practices in how technical assumptions are accounted in PV investment cost calculation*, No. Solar Bankability WP3 Deliverable D, 3.

[151] M. Vázquez and I. Rey-Stolle, *Photovoltaic module reliability model based on field degradation studies*, Progress in photovoltaics: Research and Applications, 16 (2008), pp. 419–433.

[152] A. Virtuani, E. Annigoni, and C. Ballif, *One-type-fits-all-systems: Strategies for preventing potential-induced degradation in crystalline silicon solar photovoltaic modules, Submitted to Progress in Photovoltaics: Research and Applications.*

[153] U. Weber, R. Eiden, C. Strubel, T. Soegding, M. Heiss, P. Zachmann, K. Nattermann, H. Engelmann, A. Dethlefsen, and N. Lenck, *Acetic acid production, migration and corrosion effects in ethylene-vinyl-acetate-(EVA-) based PV modules*, in Proceedings of the 27th European PVSEC, 2012.

[154] S. Wilcox and W. Marion, *Users manual for tmy3 data sets (revised)*, tech. report, National Renewable Energy Lab.(NREL), Golden, CO (United States), 2008.

[155] J. Wohlgemuth, D. Cunningham, D. Amin, J. Shaner, Z. Xia, and J. Miller, *Using accelerated tests and field data to predict module reliability and lifetime*, in 23rd European Photovoltaic Solar Energy Conference and Exhibition, 2008, pp. 1–5.

[156] J. WOHLGEMUTH AND S. KURTZ, *International PV QA Task Force's proposed comparative rating system for PV modules*, in Reliability of Photovoltaic Cells, Modules, Components, and Systems VII, vol. 9179, International Society for Optics and Photonics, 2014, p. 917902.

[157] J. H. WOHLGEMUTH AND M. D. KEMPE, *Equating damp heat testing with field failures of PV modules*, in 39th IEEE Photovoltaic Specialists Conference, 2013.

[158] J. H. WOHLGEMUTH AND S. KURTZ, *Using accelerated testing to predict module reliability*, in Photovoltaic Specialists Conference (PVSC), 2011 37th IEEE, IEEE, 2011, pp. 003601–003605.

[159] WOHLGEMUTH, JOHN AND KURTZ, SARAH, *Photovoltaic module qualification plus testing*, in Photovoltaic Specialist Conference (PVSC), 2014 IEEE 40th, 2014, pp. 3589–3594.

[160] S. YAMAGUCHI, S. JONAI, K. HARA, H. KOMAKI, Y. SHIMIZU-KAMIKAWA, H. SHIBATA, S. NIKI, Y. KAWAKAMI, AND A. MASUDA, *Potential-induced degradation of cu (in, ga) se2 photovoltaic modules*, Japanese Journal of Applied Physics, 54 (2015), p. 08KC13.

[161] A. ZIELNIK, *Validating photovoltaic module durability tests*, Solar America Board for Codes and Standards, (2013).

Acknowledgements

First of all, I would like to express my gratitude to my advisor, Prof. Christophe Ballif, for having given me the opportunity to pursue a PhD at PVLab. The trust you showed in me has always been very important and of great encouragement to me. Your incredible knowledge of photovoltaics, the passion and enthusiasm that you always put in your work have been a great source of inspiration.

I am very grateful to my co-advisor, Dr. Alessandro Virtuani, for having taken care of my scientific and professional development in the best possible way. You have always been available to discuss about my research. Thank you for everything you taught me about experimental physics and for sharing with me your broad knowledge of the PV industry. During these years you have taken any situation as an opportunity to teach me something new. I also thank you for having always found the time to talk about professional and personal issues, even if you were very busy. I have been very lucky to have had Dr. Fanny Sculati-Meillaud as co-advisor at the beginning of my PhD. Fanny, I really admire your approach to work and science. You have been an extraordinary example for me to follow.

I wish to thank the president of the jury, Prof. Jürg Schiffmann, and the members of the jury, Prof. Herbert Shea, Dr. Tony Sample, and Dr. Volker Naumann for accepting to be part of my thesis committee, and for your valuable comments that helped me to improve my thesis.

A special thanks goes to Xavier, for the precious support in the experimental work. You have always been reliable and professional, and working with you was always very enjoyable. I wish to thank my office mates, Ana and Lionel, for sharing this journey with me, and especially Ana for your helpfulness and your frankness in our personal discussions.

I would like to thank the researchers at CSEM PV-Center with whom I collaborated, especially Antonin Faes for our discussions on research topics and for the advice he provided in many occasions, Jacques Levrat for his explanations on electrical modeling of modules, and Matthieu Despeisse for encouraging a fruitful collaboration with his group.

In the beginning of my PhD I could profit from the experience from former members of the module encapsulation group. I am especially grateful to Gianluca (CSEM PV-Center) for his help in introducing me to the lab work and for having always been available for any lab-related question. At CSEM PV-Center I also wish to thank Laure-Emmanuelle, Hengyu, Jonathan,

Karin, and Valentin for the support and the scientific discussions; Pierrick and Sylvain for their help with the equipment at Innoparc.

I would like to express my gratitude to all the researchers who discussed with me at international conferences. In particular, I am grateful to Peter Hacke and Mike Kempe (NREL) for sharing their valuable opinion and providing some data on PID in Florida and the spreadsheet for the calculation of module temperature at night. David Miller (NREL) and Jens Hattendorf (Bosch) are also acknowledged for fruitful discussions. I also had the chance to collaborate with Dr. Marko Jankovec from the University of Ljubljana. Thank you for the time and effort you always put in our work, and for the nice discussions we had on several occasions. I am grateful to Maria Luisa Lo Trovato and Paola Pugliatti (Enel Green Power) for sharing their direct experience and delivering some testing material, and to Tomas Cebecauer and Artur Skoczek (Solargis) for delivering the meteorological data used in Chapter 5.

I owe to Omid (INDEOtec) the privilege of being part of the exciting adventure of renewable energies. I am enormously grateful to you for introducing me to the field of photovoltaics, and for encouraging me to pursue a PhD in this domain. A big word of thanks goes also to Fabrice for his guidance during my internship at INDEOtec, and for always showing me you cared about my path.

My gratitude goes to all my wonderful friends, in particular, Camilo, Josua, Natalia, Vincenzo, Johannes, and Jan. You have shared with me the ups and downs of the PhD experience, and were always there whenever I needed help. Thanks also for the amazing times outside the lab and all the fun moments (VIP tour on Aare to mention one!). I am grateful to all my friends with whom I shared many nice moments in Switzerland: Janina, Gizem, Alex, Linus, Darya, Jess, Corina, Marek, Chiara, Elaine, and Alex.

I am infinitely grateful to my parents: I could not have lived this amazing experience without your constant and unconditional support. Thanks to all my family, and to Daniela, Maurizio, Beatrice, and Fabrizio for following this adventure from far away and always making me feel your enthusiasm for what I was studying.

Having an extraordinary person at my side during these four years has been fundamental to accomplish this PhD. Alberto, you know more than anyone else what effort it took to reach this important goal. You were always there to support me in the moments of difficulty and helped me to improve myself. My very special “thank you” goes to you: you have been my anchor and my best teacher.

I finally wish to thank all the members of PVLab. In particular, I thank Aïcha for having always been available to help me in many situations. This work would have not been possible without the skillful help of PVLab technicians, Cédric, Lionel, Aymeric, and Joël Currit. I am also grateful to Joël Sunier for your help in technical activities in the beginning of my PhD. Thank you Mary-Claude, Karine, and Hassan, for your kind and efficient support in the administrative tasks. I would further like to thank Jarle for his Master thesis work, and all the students and interns who joined the reliability group. In particular, Martin, Alessia, Arnaud, Micha, Ludovic, and Pierre. Thanks to Cécile for her friendly assistance with the administrative tasks related to the doctoral school, and to Lara for the language quality control of this dissertation.

This thesis was possible thanks to the financial support from EOS Holding. I would also like to acknowledge the financial contribution provided by the SCCER-Furies project (supported by CTI), SolarSwissConnect, the Swiss Federal Office of Energy (OFEN), the Swiss National Science Foundation (SNSF) and the EPFL doctoral school in energy (EDEY).

Neuchâtel, 2018
Eleonora Annigoni

Eleonora Annigoni

École Polythechnique Fédérale de Lausanne (EPFL)

Curriculum Vitæ

EDUCATION

- **Ph.D. student in Microengineering**, EPFL, Switzerland, May 2014 – present.
  Research Topics: Reliability in Photovoltaics, Mathematical Modeling.
  Advisor: Prof. Dr. Christophe Ballif, Co-Advisor: Dr. Alessandro Virtuani.
- **M.Sc. in Mathematics**, University of Trento, Italy, Mar. 2012.
  Dissertation: "An Improved Dynamical Approach to Bargman Superselection Rule".
  Advisor: Prof. Dr. Valter Moretti.
- **B.Sc. in Mathematics**, University of Udine, Italy, Oct. 2008.
  Dissertation: "Modified Theories of Gravitation".
  Advisors: Prof. Lorenzo Freddi, Dr. Stefano Ansoldi.

EXPERIENCE

- **Doctoral Assistant**, May 2014 – present.
  Photovoltaics and Thin Film Electronics Laboratory, EPFL, Switzerland.
- **Trainee**, Jan. 2014 – Apr. 2014.
  CSEM PV-center, Neuchâtel, Switzerland.
- **Trainee**, Aug. 2013 – Dec. 2013.
  INDEOtec (scientific park NEODE), Neuchâtel, Switzerland.
- **Project Assistant**, Feb. 2012 – Aug. 2012.
  Laboratory of Industrial Mathematics and Cryptography, University of Trento, Italy.

AWARDS

- Best Overall Poster in Poster Session #3, PV Module Reliability Workshop, NREL, Colorado, USA, 2015.

PUBLICATIONS

- A. Virtuani, E. Annigoni, and C. Ballif, ***One-Type-Fits-All-Systems: Strategies for Preventing Potential-Induced Degradation in Crystalline Silicon Solar Photovoltaic Modules***. Submitted to *Progress in Photovoltaics*, 2018.
- E. Annigoni, A. Virtuani, J. Levrat, A. Faes, F. Sculati-Meillaud, M. Despeisse, and C. Ballif, ***Quantifying and Modeling the Impact of Interconnection Failures on the Electrical Performance of Crystalline Silicon Photovoltaic Modules***. Submitted to *Progress in Photovoltaics*, 2018.
- E. Annigoni, A. Virtuani, A. Ndiaye, N. Wyrsch, M. L. Ndiaye, C. Ballif, and C. M. F. Kebe, ***Promoting a sustainable diffusion of solar PV electricity in Africa: Results of the CODEV project***. Proc. of the European Photovoltaic Solar Energy Conference and Exhibition (EU PVSEC), 2909 – 2912, 2017.
- E. Annigoni, A. Virtuani, F. Sculati-Meillaud, and C. Ballif, ***Modeling Potential-Induced Degradation (PID) of Field-Exposed Crystalline Silicon Solar PV Modules: Focus on a Regeneration Term***. Proc. of the IEEE Photovoltaic Specialists Conference (PVSC), 2017.
- A. Virtuani, E. Annigoni, and C. Ballif, ***Preventing the Insurgence of Potential Induced Degradation (PID) in Crystalline Silicon PV Modules: Relationship between PID and BOM (Bill of Material)***. Proc. of the IEEE Photovoltaic Specialists Conference (PVSC), 2017.
- M. Jankovec, F. Galliano, E. Annigoni, H.-Y. Li, F. Sculati-Meillaud, L.-E. Perret-Aebi, C. Ballif, and M. Topič, ***In-Situ Monitoring of Moisture Ingress in PV Modules Using Digital Humidity Sensors***. IEEE Journal of Photovoltaics, vol. 6, No. 5, 1152 – 1159, 2016.
- D. C. Miller, E. Annigoni, A. Ballion, J. Bokria, L. Bruckman, D. M. Burns, X. Chen, J. Feng, R. H. French, S. Fowler, C. C. Honeker, M. D. Kempe, H. Khonkar, M. Köhl, L.-E. Perret-Aebi, N. H. Phillips, K. P. Scott, F. Sculati-Meillaud,

and J. H. Wohlgemuth, ***Degradation in PV encapsulant strength of attachment: An interlaboratory study towards a climate-specific test***. IEEE Photovoltaic Specialists Conference (PVSC), 0095–0100, 2016.

- E. Annigoni, M. Jankovec, F. Galliano, H.-Y. Li, L.-E. Perret-Aebi, M. Topič, F. Sculati-Meillaud, A. Virtuani, and C. Ballif, ***Modeling Potential-Induced Degradation (PID) in crystalline silicon solar cells: From accelerated-aging laboratory testing to outdoor prediction***. Proc. of the European Photovoltaic Solar Energy Conference and Exhibition (EU PVSEC), 1558 – 1563, 2016.

Publications prior to PhD thesis:

- E. Annigoni and V. Moretti, ***Mass Operator and Dynamical Implementation of Mass Superselection Rule***. Annales Henri Poincaré, vol. 14, No. 4, pp. 893 – 924, 2013.

POSTERS

- E. Annigoni, A. Virtuani, F. Sculati-Meillaud, and C. Ballif, ***Modeling Potential-Induced Degradation (PID) of Field-Exposed Crystalline Silicon Solar PV Modules: Focus on a Regeneration Term***. IEEE Photovoltaic Specialists Conference (PVSC), Washington D.C., USA, 2017.
- E. Annigoni, A. Martins, X. Niquille, J. Sunier, C. Ballif, and F. Sculati-Meillaud, ***Reliability of PV elements: lifetime and long-term performance prediction***. National Photovoltaics Conference, Bern, Switzerland, 2016.
- E. Annigoni, F. Galliano, M. Jankovec, H.-Y. Li, L.-E. Perret-Aebi, C. Ballif, and F. Sculati-Meillaud, ***Moisture ingress into PV modules: long-term simulations and a new monitoring technique***. PV Module Reliability Workshop, NREL, Colorado, USA, 2015.
- E. Annigoni, H.-Y. Li, V. Chapuis, F. Galliano, C. Ballif, and L.-E. Perret-Aebi ***Optimized PV module encapsulations for an improved reliability in various climatic conditions***. National Photovoltaics Conference, Lausanne, Switzerland, 2014.

TALKS

- ***Modeling Potential-Induced Degradation (PID) in crystalline silicon solar cells: From accelerated-aging laboratory testing to outdoor prediction***. European Photovoltaic Solar Energy Conference and Exhibition (EU PVSEC), Munich, Germany, 2016.
- ***Predictive models for the power degradation of c-Si PV modules: Potential-Induced Degradation and moisture ingress***. EUROREG PV Workshop, Ljubljana, Slovenia, 2016.

PARTICIPATION TO CONFERENCES AND WORKSHOPS

- IEEE Photovoltaic Specialists Conference, Washington D.C., USA, 2017.
- Energy Rating and Module Performance Modeling Workshop, SUPSI, Lugano, Switzerland, 2017.
- African Conference on Renewable Energies, Dakar, Senegal, 2016.
- EUROREG PV Workshop, Ljubljana, Slovenia, 2016.
- European Photovoltaic Solar Energy Conference and Exhibition, Munich, Germany, 2016.
- SOPHIA PV-Module Reliability Workshop, AIT, Vienna, Austria, 2016.
- National Photovoltaics Conference, Bern, Switzerland, 2016.
- PV Performance Modelling and Monitoring Workshop, TÜV Rheinland, Germany, 2015.
- PV Module Reliability Workshop, NREL, Colorado, USA, 2015.
- Training course “Fiabilité des produits”, Neuchâtel, Oct. 2015.
- SOPHIA PV-Module Reliability Workshop, Fraunhofer ISE, Freiburg, Germany, 2014.
- National Photovoltaics Conference, Switzerland, 2014.
- Workshop on Comsol programming, CSEM, Switzerland, 2014.

PROFESSIONAL EXPERIENCE

- Organizer of the *Ateliers Jouets Solaires* (activities for the popularization of photovoltaics in public schools) in the period 2014 – 2017, EPF Lausanne, Switzerland.
- Teaching assistant for a course in Applied Mathematics, University of Trento, Italy, Spring 2012.